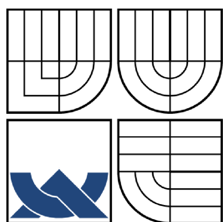

VYSOKÉ UČENÍ TECHNICKÉ V BRNĚ
BRNO UNIVERSITY OF TECHNOLOGY

FAKULTA STROJNÍHO INŽENÝRSTVÍ
ÚSTAV FYZIKÁLNÍHO INŽENÝRSTVÍ

FACULTY OF MECHANICAL ENGINEERING
INSTITUTE OF PHYSICAL ENGINEERING

DEPOSITION AND ANALYSIS OF DLC THIN FILMS

DEPOZICE A ANALÝZA TENKÝCH VRSTEV DLC

DIPLOMOVÁ PRÁCE
MASTER'S THESIS

AUTOR PRÁCE
AUTHOR

Bc. MIROSLAV RUDOLF

VEDOUCÍ PRÁCE
SUPERVISOR

prof. RNDr. TOMÁŠ ŠIKOLA, CSc.

BRNO 2009

Abstrakt
Diplomová práce nastiňuje problémy spojené s výrobou a analýzou tenkých vrstev DLC:H. Tyto vrstvy jsou ve středu zájmu mnoha vědeckých pracovníků již po několik desetiletí. V současné době existuje mnoho technik pro přípravu a analýzu. Příprava DLC vrstev má zásadní vliv na jejich vlastnosti a možnosti použití. Je zde mnoho kritérií jak vrstvy posuzovat. V této práci jsou studovány vlastnosti DLC:H vrstev připravených na substrát krystalického křemíku metodou RF-PECVD a následně jsou studovány mechanické, tribologické a optické vlastnosti. Jsou zde využity techniky jako XPS, Ramanova spektroskopie, reflektometrie, měření tvrdosti a adheze. Část práce se zabývá modelováním DLC z prvních principů. Pro tento účel je využito prvo-principiálního programu Abinit který je šířen pod GPL. Je studována otázka přípravy vstupních dat s ohledem na konvergenci výsledků. Pozornost je také věnována výpočtu vibračních spekter ve středu Brillouinovy zóny (Γ bod) a celkové hustotě elektronových stavů clusteru DLC v supercele tvaru krychle. Tyto výsledky mohou být porovnány s experimentálně získanými daty z Ramanovy spektroskopie, respektive z XPS spektra valenčního pásu.

Summary
Diploma thesis outlines the problems during preparation and analysis of DLC:H thin films. Many scientists have been interested in these films already for several decades. In the present time, many techniques exist for their preparation and analysis. The preparation of DLC has a significant influence on their characteristics and applications. There are many criteria how to examine the films. In this thesis, the DLC:H layers prepared on the crystalline silicon by the RF-PECVD method are discussed. Subsequently, the mechanical, tribological and optical properties have been investigated. The techniques as XPS, Raman spectroscopy, reflectometry, hardness and adhesion measurements have been employed. A part of the thesis deals with the modelling of DLC and DLC:H films from the first principles. The first-principle simulation software Abinit is used for this purpose. Abinit has been distributed under the GPL. The way of selection of input parameters has been studied with respect to the convergence of the results. Attention has been paid to computing the vibrational spectra in the middle of the Brillouin zone and the overall density of electronic states of DLC cluster in a cubic supercell. These data can be compared with results experimentally obtained from Raman spectroscopy and XPS of the valence band, respectively.

Klíčová slova
DLC, RF-PECVD, XPS, Ramanova spektroskopie, nanotvrdost, scratch test, reflektometrie, Abinit

Keywords
DLC, RF-PECVD, XPS, Raman spectroscopy, nanohardness, scratch test, reflectometry, Abinit

RUDOLF, M.*Deposition and analysis of DLC thin films.* Brno: Vysoké učení technické v Brně, FAKULTA STROJNÍHO INŽENÝRSTVÍ, 2009. 67 s. Vedoucí diplomové práce prof. RNDr. Tomáš Šikola, CSc.

Prohlašuji, že jsem diplomovou práci vypracoval samostatně pod vedením prof. RNDr. Tomáše Šikoly, CSc.

Bc. Miroslav Rudolf

I sincerely thank prof. Tomáš Šikola for giving me a chance to continue on the project which I have started several months ago at Aston University in Birmingham. He kindly read and commented this thesis, although he had a lot of other duties.

I have spent six months in professor John Sullivan's group. This residence abroad has been largely covered by the program Erasmus–Socrates funding. It has been small research group interested in surface science. I thank prof. John Sullivan that he led me and provided me all what I needed. Mr. Andrew Abbot taught me to run a deposition system and he gave me a hand all the time. I am deeply indebted to Dr. Baogui Shi who had paid a lot of his attention to me. He spent a lot of time to train me in handling a nanoindentor and performed measurements of photoelectron spectra. Everytime, when I needed, he devoted time to help me. I will never forget dialogues with Dr. Gavin Wilson about problems relating to this work and Dr. Sayah Saied's "talking time" during lunch time, thanks to that I was losing my shyness in speaking in English. I wish to be a part of such a group in my future career.

I thank to Dr. Dušan Hemzal from Masaryk University in Brno, who performed the measurements on Raman spectroscopy. I also thank to Dr. Michal Urbánek for the consultations on writing a program on fitting the reflectance spectra.

Last but not least, I would like to thank my parents for their finance and emotional support not only during my university studies.

Brno
May 2009

Bc. Miroslav Rudolf

Contents

1 Introduction **2**
1.1 Applications . . . 3
1.2 Characteristics — sp^3 and sp^2 hybridization . . . 4
1.3 Preparation . . . 4
1.3.1 Deposition method – Capacitively coupled RF-PECVD . . . 5

2 Characterisation **6**
2.1 PES (Photoelectron Spectroscopy) . . . 6
2.2 Tribology . . . 7
2.2.1 Hardness and scratch . . . 8
2.3 Raman spectroscopy . . . 11
2.4 Spectroscopic reflectivity . . . 16
2.4.1 Index of refraction and extinction coefficient . . . 17

3 Experiment **19**
3.1 Deposition . . . 19
3.2 Hardness and scratch . . . 27
3.2.1 Hardness . . . 27
3.2.2 Scratch test . . . 30
3.3 Photo-electron spectroscopy . . . 33
3.3.1 C 1*s* core level spectroscopy for sp^3 content determination . . . 33
3.3.2 Auger C K-V-V spectra and sp^3 content . . . 38
3.3.3 Valence band of DLC . . . 41
3.4 Raman spectroscopy . . . 43
3.4.1 Structural information . . . 43
3.4.2 Hydrogen content . . . 45
3.4.3 Results . . . 46
3.5 Spectroscopic reflectivity . . . 47
3.5.1 Program based on PJDOS (Parameterising Joint Density of States) model . . . 48
3.5.2 Program based on Forouhi-Bloomer (FB) model . . . 49
3.5.3 Results . . . 49
3.6 First principle calculations of vibrational spectra and ground states of DLC in *Abinit* . . . 52
3.6.1 Preparation of an initial structure for the ground state calculations 52
3.6.2 Convergence study . . . 52
3.6.3 Computation of a relaxed structure of DLC having a different hydrogen content . . . 53
3.6.4 Calculation of electronic DOS (Density of States) . . . 54
3.6.5 Calculation of VDOS (Vibrational Density of States) . . . 58

4 Conclusion **61**

5 Appendix **67**

1. Introduction

The aim of a thesis is the preparation and a subsequently study of DLC (Diamond-like Carbon) layers. The DLC thin films were prepared by chemical vapour deposition using a methane/hydrogen a precursor gas and then subsequently studied by spectroscopic analytic methods as X-ray photoelectron spectroscopy, Raman spectroscopy and spectroscopic reflectivity. The thickness of deposited layers, hardness, reduced modulus and adhesion were measured. A part of the thesis deals with *ab-initio* calculations of DLC and then comparison with experimental results.

Using diamond in industry has become common, thereby diamond started to be inaccessible. It was discovered that crystalline diamond has a combination of properties (largest bulk modulus, 5.5 eV optical gap, highest atom density of any solids, thermal conductivity) unequalled with other known materials. Thanks to these characteristics diamond has begun an aim of many scientists from all of the world. The synthetic diamond can be manufactured thanks to a HPHT (High Pressure-High Temperature) technique [1]. The method requires technology which is able to manage high pressures and temperatures (see fig. 1.1). The region A masked in fig. 1.1 is used for commercial production of diamond from graphite.

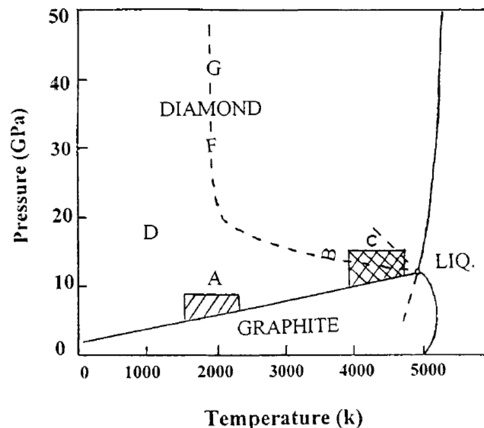

Figure 1.1: T-P phase diagram of carbon [1]

High pressure and temperatures restricted a massive expansion of the HPHT technique to the industry and thus there was demand to product diamond at lower pressures and temperatures. In 50th of the 20th century, the CVD (Chemical Vapour Deposition) method was used for a synthesis of metastable diamond under vacuum conditions.

Diamond like carbon (DLC) is classified as an amorphous carbon with a high fraction of C-C sp^3 hybridization [2]. Tetrahedral amorphous carbon ta-C is kind of DLC with the maximum of sp^3 content. DLC can also consists of a significant amount of hydrogen (see fig. 1.2). This structure is called a-DLC:H (Hydrogenated amorphous Diamond Like Carbon) and can be divided into the four classes:

- a-C:H with the highest amount of hydrogen (40–50) %, 60 % sp^3 hybridization. Films are soft and of low density. Energy of the band gap E_g (energy between the highest occupied and the lowest unoccupied band) is equal to (2–4) eV.

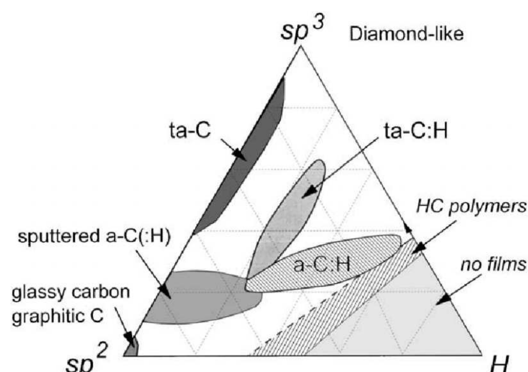

Figure 1.2: Ternary phase diagram of bonding in amorphous carbon-hydrogen alloys [3].

- a-C:H with hydrogen content (20–40) %, lower overall sp^3 hybridization but higher C-C sp^3 hybridization. Films have better mechanical properties. Energy E_g=(1–2) eV.
- ta-C:H (hydrogenated tetrahedral amorphous carbon). The highest C-C sp^3 content 70 %, higher density 2.4 g/cm^3, Young's modulus up to 300 GPa, $E_g \approx 2.3$ eV
- a-C:H – low H content (< 20 %), high sp^2 content and sp^2 clustering, $E_g < 1$ eV.

1.1. Applications

At present, the DLC thin films can be used in many diverse applications:

- magnetic storage technology [4]
- razor blades [4]
- car and engine parts – gears, wrist pins, valve lifters, fuel injector parts, piston rings and pump plungers of diesel injection systems, valve trains, tappets, motorcycle fork tubes [4]
- textile industry – components of textile machines in contact with yarn or textiles are protected with DLC (spinning rings, rapiers, needles, guides, grippers, yarn storage disks, weft tongs in weaving looms) [4]
- injection moulding [4]
- cutting tools – mills and drills for working on fiber, polymers, wood or aluminium [4]
- coatings for gas barriers blocking the passage of gas molecules through PET walls [5]
- photovoltaic solar cells [6]
- spacer tools for electron guns of cathode ray tube [7].

1.2. Characteristics — sp^3 and sp^2 hybridization

Valence bond and Molecular orbital theory

Carbon may form a big amount of crystalline and amorphous structures, since it can exist in three hybridizations. Generally, for a set of atoms it is advantageous to make energeticly profitable molecules and thus to achieve a state with minimum potential energy. These processes can be described by VB (Valence Bond) and MO (Molecular Orbital) theories. VB describes chemical bonds, which specifies the character of electrons included in the structure. This description of bonds leaves an electron-pair concept, which is useful in "Lewis electron dot structure"(e.g. $:\dot{C}\cdot$ for carbon atom or $:N \equiv N:$ for nitrogen molecule), so making the use of localised orbitals. This theory was first described by Walter Heitler and Fritz London and later worked by Linus Pauling, who also introduced an idea of "orbit hybridization " [8]. The concept of localised orbitals is very useful for description of molecules in a ground state or of dissociation binding energy. Nevertheless, for description of excited and ionised states is generally preferable a model of delocalised electrons.

MO theory may be used for description of ground states as well as of excited states in molecules. VB and MO theories propose different nature of electron-electron interactions. In the VB theory, the wave function of two electrons included in a mutual bond remain in their own atoms. While in the MO theory, an electron pair is inside an electron cloud being outstretched over two or more atomic cores. We can say that the VB theory is built up localised bonding, while the MO theory uses delocalised bonding.

These two theories utilise the idea of hybridization. A hybrid orbital is a linear combination of atomic orbitals. It is a new base orbital which represents a better description of molecular bonding. The terms sp^3 and sp^2 can be specified as $sp^3 = s+p_x+p_y+p_z$ and $sp^2 = s+p_x+p_y$, respectively, where s, p_x, p_y, p_z are atomic orbitals.

1.3. Preparation

One of the first depositions of DLC was performed by Sol Aisenberg and Ronald Chabot [9]. They used an ion beam deposition technique and substrates made of crystalline silicon, steel and glass at room temperature. They measured the characteristics of the films as resistivity reaching $10^{10}\,\Omega$, dielectric constant equal to 8–14 (calculated from the capacitance) as compared with 16.5 for diamond. The films were optically transparent with the high refracting index (over 2) and resistant to hydrogen hydrofluoric acid. The DLC films showed up high hardness, low friction coefficient and high resistivity against wear.

In the present time, many preparation techniques of DLC exist. It includes dense plasma focus [10], electron cyclotron wave resonant plasma [11], filter arc deposition [12], magnetron-sputtering [13], combining plasma-based ion implantation and microwave ECR chemical vapour deposition [14], ion beam assisted deposition IBAD, radio frequency -PECVD etc.

The most favourite laboratory method of preparation of DLC is PECVD (Plasma Enhanced Chemical Vapour Deposition). This method (with a capacitively coupled

radio frequency supply) has also been used in this study. The method is based on ionisation of a precursor gas in a low temperature plasma. A substrate is placed on a cathode electrode. The anode is formed by chamber walls having a much higher area in comparison with the cathode. Positively charged ions are accelerated from the plasma towards the substrate by bias voltage between the plasma and the cathode. The composition of grown films depends on the nature of the precursor gas. In this particular case, a mixture of methane and hydrogen was used. The resulting properties of the film depend on deposition parameters (bias voltage, pressure, substrate temperature) and the composition of the precursor gas. As the most favourite precursor gas, hydrocarbons such as methane, ethane, propane and so on are used for making DLC. The resulting films contain big amount of hydrogen (20 %–50 %).

1.3.1. Deposition method – Capacitively coupled RF-PECVD

Capacitively coupled RF (Radio Frequency) glow discharge is widely used for deposition or etching of thin films. In the RF discharge, under vacuum conditions, negative bias voltage (with respect to plasma potential) appears on a cathode electrode. This is a direct consequence of differences in mobility and diffusivities of electrons and ions. The electric field appears near the cathode resulting in accelerating positive charged ions towards the cathode. Deposition/etching in a capacitively coupled RF system can be described by an electrical circuit shown in fig. 1.3.

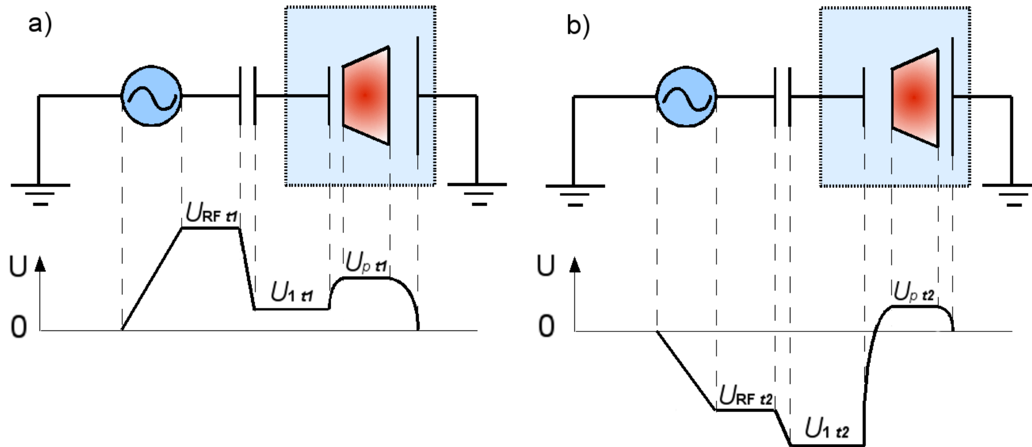

Figure 1.3: Electrical scheme describing the capacitively coupled RF system.

In figure 1.3, two different periods of a one RF cycle having opposite phases are shown. We can present the capacitively coupled RF plasma system by a circuit with three capacitors. One is placed between the cathode and the RF supply (a real capacitor) and the next two virtual capacitors representing dark space sheaths are located near the cathode and the anode (a chamber). From the potential distribution shown in fig. 1.3, it is clear that at every time, the highest potential in the circuit is U_p (except RF supply potential). A difference between the plasma potential U_p and the potential on the cathode U_1 is the bias voltage U_b and determines energy of ions accelerated towards the cathode surface.

2. Characterisation

2.1. PES (Photoelectron Spectroscopy)

XPS (X-ray Photoelectron Spectroscopy) or also ESCA (Electron Spectroscopy for Chemical Analysis) is one of the most widespread methods of surface analysis. The method XPS was developed by K. Siegbahn and his experimental group. He received a Nobell price for this work in 1981. This method is based on a photo-electron effect described by Einstein in the year 1905.

XPS is able to give a quantitative information about elements and their chemical or surface state at a studied surface and using angular dependent measurements, it is able to obtain information about depth distribution of elements. Photoelectron spectrum shows number of detected photoelectrons as a function of their kinetic or binding (E_b) energy.

XPS generally uses X-rays as Al Kα (1486.6 eV) or Mg Kα (1253.6 eV). It may be also chosen other radiation as Ti Kα (2040 eV). Electrons escaping the sample surface are analysed by a hemispherical analyzer according to their kinetic energy. Thus a photoelectron spectrum is obtained. Each electronic state in an atom has an appropriate binding energy E_b. The XPS spectrum is an image of atom and molecule electronic states. However, each electronic state has its own cross section which is a function of energy of incident photons. The cross sections of hydrogen and helium are small as compared to other atoms. It leads to lower probability of electron generation, resulting in lower counts of photoelectrons. Hence, the XPS is not sensitive to hydrogen and helium.

Electrons have to escape the sample and reach an analyzer. A mean free path of electrons must be higher than a distance between the sample and the end of the analyzer. Therefore, XPS works under UHV (Ultra High Vacuum) or in XHV (Extreme High Vacuum) conditions.

One of the most critical part of a XPS equipment is a hemispherical electron energy analyzer (HMA). The role of the analyzer is to detect electrons emitted from a specimen according to their energy. The analyzer can work in two modes — Constant Analyzer energy (CAE) and Constant Retard Ratio (CRR). In the CAE mode the pass energy is constant and so a deceleration/acceleration voltage is ramped by the lens to build up a spectrum. In the CRR mode the voltage difference between the hemispheres is proportional to the retarding voltage of the analyzer. Alternatively, the ratio of kinetic energy to pass energy is constant during scanning [15]. Resolution of the analyzer in the CAE mode is given

$$\Delta E = \frac{PE}{4}\left(\frac{w}{R_0} + 2\alpha^2 + \frac{w^2}{{R_0}^2} + \frac{z^2}{{R_0}^2}\right), \tag{2.1}$$

where w is the width of a slit, R_0 the mean radius of the hemispheres, α the radial entrance angle, z the slit length and PE pass energy. If we neglect the higher terms in equation (2.1), for resolution of the analyzer we obtain

$$\Delta E = \frac{PE}{4}\frac{w}{R_0}. \tag{2.2}$$

In the CAE mode of *Thermo Fisher Scientific ESCA 250* $\Delta E = 0.018 \cdot PE$. Relation 2.2 determines the width of the response function of the analyzer. The response function is for most of equipments given by the Gaussian function. The *ESCA 250* operates with a monochromatic X-ray source producing X-rays of well defined energy resolution. There is an electron gun providing a beam of focused electrons with energies up to 15 keV. Electrons impact the anode (aluminium-thin film deposited on a copper base) and produce X-rays. The X-rays are monochromatized by diffraction on a quartz crystal, to give a pure Al Kα (fig. 2.1) line of a Lorentzian shape. The convolution of a response

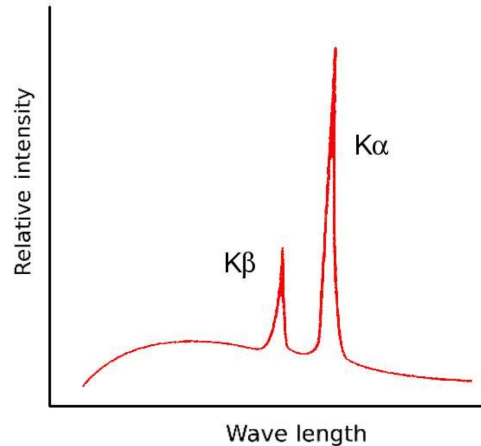

Figure 2.1: X-ray radiation spectrum [16].

function of the analyzer with the line $K\alpha$ gives a total resolution of the spectrometer.

2.2. Tribology

Tribology is a research field about friction, wear and lubrication of a surface in a relative motion to another surface. Tribology consists of this parts.

friction [17]:
Friction during the relative movement of two solid objects is usually proportional to the force pushing surfaces together. Hence, the force affecting friction is the force perpendicular to the surface (normal force), and is denoted N. The frictional force F_t can be written as $F_t = N \cdot \mu$, where μ is the friction coefficient having classically two different values (dynamical and statical).

If two surfaces move with respect to each other, the friction force is almost constant for a wide range of velocities. The dynamical friction coefficient is typically lower than the statical one.

wear [18]:
Wear removes the material from a solid surface as a result of mechanical acting by an other solid body or of chemical processes. Wear turns up as a progressive loss of material upon interaction of the two solid bodies. Several types of wear exist:

- adhesive
- abrasive
- corrosive

- surface-fatigue

Adhesive wear:
This type of wear is the most common. It occurs upon strong adhesive forces acting on the interface of two solids, when these are pushed together. During this process a contact is made between the surfaces. A consequent movement will break this contact and fine particles crumble away.

Abrasive wear:
Abrasive phenomena occur during movement of a hard and rough surface along a gentle surface, thereby grooves arise on this gentle surface. This phenomenon also occurs if particles are presented among two soft surfaces. These particles are embedded into one of these surfaces and the second surface is weared down during its motion. Abrasive phenomena also appear, when a liquid stream of high kinetic energy contains solid particles and hits the surface.

Corrosive wear:
Corrosive wear occurs any time when gas or liquid chemically attacks the surface being in relative movement to another surface. Some materials can become passivated during this process. Passivation (protective coating) results in deceleration of corrosion process.

Surface-fatigue:
Surface fatigue occurs during a cyclic loading. As a result, microscopic cracks below the surface are formed and then separation of particles from the surface occurs.

2.2.1. Hardness and scratch

a) **Hardness:**

The most common method used for hardness and modulus measurements was developed by Oliver and Pharr [19]. In this approach the total penetration depth is given by the sum of the plastic depth (contact depth) h_p (fig.2.2) and the elastic depth h_e which represents the elastic deformation of the surface during loading. Thus the total penetration depth h_t is given by

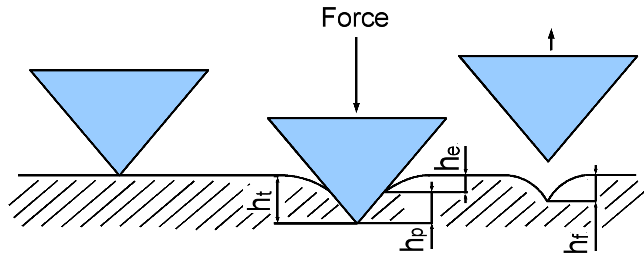

Figure 2.2: A schematic of the hardness measurement. Total depth h_t, plastic depth h_p, elastic depth h_e and final depth h_f.

$$h_\mathrm{t} = h_\mathrm{p} + h_\mathrm{e}, \tag{2.3}$$

where

$$h_\mathrm{e} = \varepsilon C P_\mathrm{max}, \tag{2.4}$$

where $1/C$ is the slope of an unloading curve at a maximum load P_{max} and C is called contact compliance [19]) see fig.2.3, ε is the constant depending on the indentor geometry

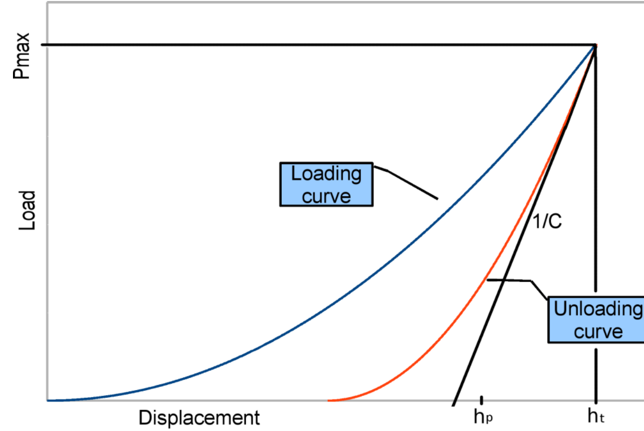

Figure 2.3: Depth determination.

(for the Berkovich indentor $\varepsilon = 0.75$). Value h_{p} can be evaluated from equations 2.3 and 2.4. The contact area A_{c} is determined by the plastic depth h_{p} and the known diamond area function A being for the Berkovich indentor $A(h) = 24.5 \cdot h^2$. This is an ideal function which must be corrected by measurement according to the range of penetration depths. The hardness H is determined by equation

$$H = \frac{P_{\mathrm{max}}}{A_{\mathrm{c}}}. \tag{2.5}$$

Young's modulus can be obtained from the the equation

$$C = \frac{\sqrt{\pi}}{2E_{\mathrm{r}}\sqrt{A_{\mathrm{c}}}}, \tag{2.6}$$

where E_{r} is the reduced modulus,

$$\frac{1}{E_{\mathrm{r}}} = \frac{(1-\nu_{\mathrm{s}}^2)}{E_{\mathrm{s}}} + \frac{(1-\nu_{\mathrm{i}}^2)}{E_{\mathrm{i}}}, \tag{2.7}$$

where ν_{s} is Poisson's ratio for the sample, $\nu_{\mathrm{i}} = 0.07$ is Poisson's ratio for the indentor, E_{s} is Young's modulus for the sample and $E_{\mathrm{i}} = 1141\,\mathrm{GPa}$ is Young's modulus for the indentor [19]. For most materials $\nu_{\mathrm{s}} = 0.25$.

b) **Scratch:**

Critical loads are influenced by many intrinsic and extrinsic parameters. According to [20], there are four requirements for quantitative scratch adhesion test:

1. adhesion-related failure mode
2. well defined failure mechanism
3. adhesion failure identification (location and size)

4. determination of the stress inducing failure

Soft coating: Hardness of the coating is $H < 5\,\mathrm{GPa}$ and the coating is on a softer or harder substrate. The coating fails by plastic deformation. The scratch test is not suitable for investigation of adhesion if the interfacial stress is lower than the shear strength of the softer component (substrate or coating).
Hard coating: Hardness of the coating is $H > 5\,\mathrm{GPa}$. In this case, failure modes can be divided into four groups [20]:

1. *"Through-thickness cracking—including tensile cracking behind the indentor, conformal cracking as the coating is bent into the scratch track and Hertzian cracking. These cracks may extend into the substrate if it is sufficiently brittle but are usually stopped at the interface in a hard coating on a softer substrate.*

2. *Coating detachment—including compressive spallation ahead of the indentor, buckling spallation ahead of the indentor or elastic recovery-induced spallation behind the indentor.*

3. *Chipping within the coating—usually observed for thick coatings on a softer substrate. The scratch test cannot practically measure the adhesion of coatings greater than 50 µm thick in its conventional form since it is impossible to generate sufficiently large stresses at the interface before chipping of the coating occurs.*

4. *Chipping within the substrate—for brittle coatings on brittle substrates where the adhesion is good the system tends to behave in the same way as a brittle bulk material and unless the coating is sufficiently thick chipping of the substrate will occur."*

2.3. Raman spectroscopy

Raman spectroscopy is widely used to derive the structural information of DLC and, if possible, their sp^3 fraction. Raman technique is inelastic light scattering by the change in polarizability α [3].

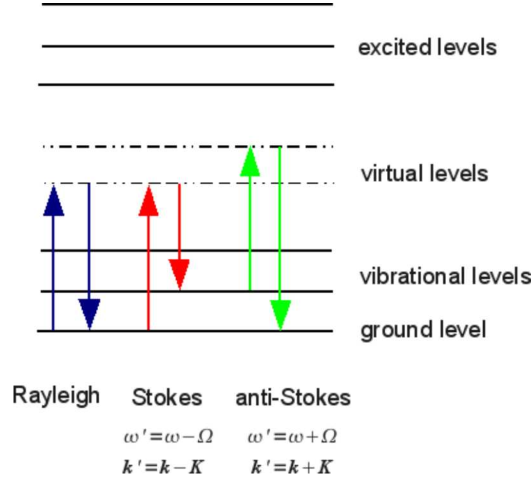

Figure 2.4: Description of the Raman phenomena in a solid. An atom in a crystal in the ground state can absorb a photon with energy $\hbar\omega$, reaches a virtual state and falls either back to the ground state (Rayleigh scattering) or to a vibrational state (Stokes process). The atom can also absorb a photon in the vibrational state and fall to the ground state (anti-Stokes process).

The process when the atom in the crystal in the ground state absorbs a photon with energy $\hbar\omega$, reaches the virtual state and irradiate a photon with lower energy $\hbar\omega'$ ($\hbar\omega > \hbar\omega'$) is called the *Stokes process* (see fig. 2.4). The atom being already in a vibrational state can absorb a photon $\hbar\omega$ and irradiate a photon $\hbar\omega'$, where $\hbar\omega < \hbar\omega'$, this is called the *anti-Stokes process*. These two mentioned energy transitions occur at different probabilities. The translation probability is temperature depend and the ratio of anti-Stokes and Stokes intensities is given by the relation [21]

$$\frac{I(\omega+\Omega)}{I(\omega-\Omega)} = \mathrm{e}^{-\frac{\hbar\Omega}{k_bT}}. \tag{2.8}$$

It is seen, that relative intensity vanishes when temperature is getting close to zero (fig. 2.5).

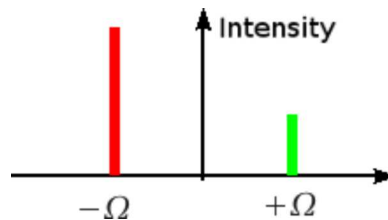

Figure 2.5: A Raman shift $\pm\hbar\Omega$ with respect to the photon excitation energy $\hbar\omega$. The peak at the energy $+\hbar\Omega$ corresponds to the annihilation of a phonon and the peak at $-\hbar\Omega$ to the creation of a phonon.

The Raman spectra of carbon films offer valuable information about atomic bonds and energy level structure of molecules. Especially in the nanostructured carbon thin films, Raman spectra are of a great importance in determination of their structure. Raman spectra are sensitive to changes in translational symmetry and are thus useful for the study of disordered or crystalline formations and of structural modifications in DLC films. The first order Raman spectrum for diamond and graphite consists of a single line at $1332\,\mathrm{cm}^{-1}$ and $1580\,\mathrm{cm}^{-1}$, respectively. The Raman spectra of DLC exhibit two main features — a peak centered at $1540\,\mathrm{cm}^{-1}$ and a weaker peak centered at $1340\,\mathrm{cm}^{-1}$, which are assigned to the G and D peaks, respectively [3].

Diatomic molecule vibrations

Raman spectra have an origin in polarization caused by incident electro-magnetic wave raising from UV up to IR and are presented as shifts from excitation frequency. Raman spectra can be described by a classical theory [22] as well. An incident wave with the intensity of

$$E = E_0 \cos 2\pi f t \tag{2.9}$$

comes to the surface of a solid and penetrates into its depth. When a diatomic molecule is irradiated by a week field E, the dipole moment

$$P = \alpha E \tag{2.10}$$

is induced. The α is called polarizability. Polarisability of the molecule is in principle the ability of the electronic cloud surrounding a molecule to be deformed by an external electric field. This phenomenon depends on the distance of valence electrons from a core. If the molecule is vibrating with the resonance frequency f_n, the displacement of nuclei q is given by

$$q = q_0 \cos 2\pi f_n t, \tag{2.11}$$

where q_0 is the amplitude. In a small range of amplitudes, α can be written as a linear function of the nuclear displacement q

$$\alpha = \alpha_0 + \left.\frac{\partial \alpha}{\partial q}\right|_{q=0} q. \tag{2.12}$$

By combination of equations 2.9, 2.10, 2.11, 2.12 we get

$$\begin{aligned} P &= \alpha_0 E_0 \cos 2\pi f t + \left.\tfrac{\partial \alpha}{\partial q}\right|_{q=0} q_0 E_0 \cos 2\pi f t \cos 2\pi f_n t \\ &= \alpha_0 E_0 \cos 2\pi f t + \tfrac{1}{2} \left.\tfrac{\partial \alpha}{\partial q}\right|_{q=0} q_0 E_0 \{\cos[2\pi(f + f_n)t] + \cos[2\pi(f - f_n)t]\}. \end{aligned} \tag{2.13}$$

The first term describes the dipole radiating light of frequency f (Rayleigh scattering). A second part gives the Raman anti-Stokes $f + f_n$ and Raman-Stokes $f - f_n$ scattering. If the polarizability change is zero, the second term vanishes and the vibration is Raman inactive (invisible in the Raman spectra).

Lattice vibrations

Let us have a base consisting of two atoms of mass M_1 and M_2 [21, 22]. By translation of this base we create a lattice where atoms with mass M_1 create one layer and atoms of mass M_2 create a second layer parallel to the first one (fig. 2.6). Equations of motion for atom at position u_s and v_s are

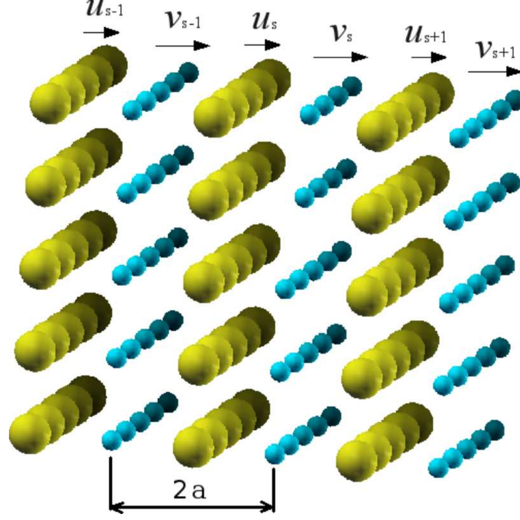

Figure 2.6: A crystal structure with two atoms in a primitive lattice with mass M_1 and M_2.

$$\begin{aligned} M_1\, \ddot{u}_s &= \kappa(v_s + v_{s-1} - 2u_s), \\ M_2\, \ddot{v}_s &= \kappa(u_{s+1} + u_s - 2v_s), \end{aligned} \tag{2.14}$$

where u_s and v_s denote the displacements of atoms indexed by s. The solutions can be expected in the form

$$\begin{aligned} u_s &= u \exp[\mathrm{i}(\Omega \mathrm{t} + \mathrm{k} \cdot 2\mathrm{sa})], \\ v_s &= v \exp[\mathrm{i}(\Omega \mathrm{t} + \mathrm{k} \cdot 2\mathrm{sa})], \end{aligned} \tag{2.15}$$

where $\Omega = 2\pi f$, k is the magnitude of a wave vector $\vec{k}$ and $2a$ is the distance (in $\vec{k}$ direction) between two identical layers. If we substitute the corresponding quantities in 2.15 to 2.14, we get a set of two linear homogeneous equations

$$\begin{pmatrix} M_1\Omega^2 - 2\kappa & \kappa\,[1 + \exp(-2\mathrm{i}ka)] \\ \kappa\,[1 + \exp(2\mathrm{i}ka)] & M_2\Omega^2 - 2\kappa \end{pmatrix} \begin{pmatrix} u \\ v \end{pmatrix} = \begin{pmatrix} 0 \\ 0 \end{pmatrix}. \tag{2.16}$$

By solving, we get an optical branch [22]

$$\Omega^2 = \kappa\left(\frac{1}{M_1} + \frac{1}{M_2}\right) + \kappa\sqrt{\left[\left(\frac{1}{M_1} + \frac{1}{M_2}\right)^2 - \frac{4\sin^2 ka}{M_1 M_2}\right]} \tag{2.17}$$

and an acoustical branch

$$\Omega^2 = \kappa\left(\frac{1}{M_1} + \frac{1}{M_2}\right) - \kappa\sqrt{\left[\left(\frac{1}{M_1} + \frac{1}{M_2}\right)^2 - \frac{4\sin^2 ka}{M_1 M_2}\right]}. \tag{2.18}$$

Lattice vibrations can be described as creation and annihilation of phonons. During the photon-phonon interaction the energy and momentum conservation laws must hold:

$$\begin{aligned} \omega^{'} &= \omega \pm \Omega \\ k^{'} &= k \pm K, \end{aligned} \tag{2.19}$$

where ω, $\omega^{'}$, and Ω is the frequency of incident light, scattered light and frequency of a phonon, respectively. The k, $k^{'}$ and K is is the wave vector of incident light, scattered light and wave vector of phonon, respectively. Values K can take the values between zero and a maximum value K_{max} corresponding to the boundary of the Brillouin zone and is approximately $\approx \pi/2a = \pi/(2 \cdot 10^{-10}\,[m]) \approx 1 \cdot 10^{8}$ [cm^{-1}], where a is a primitive lattice vector. From the observation during the Raman scattering the values $k^{'}$ are lower than $1 \cdot 10^{4}\,[\mathrm{cm}^{-1}]$. The value k of irradiating UV light is approximately equal to $\approx 2\pi/\lambda = 2\pi/100 \cdot 10^{-9}\,[m^{-1}] = 1 \cdot 10^{6}\,[\mathrm{cm}^{-1}]$. The value $k^{'}$ is negligible small with respect to the k. The value k is one hundred times lower than K_{max}. In order to satisfy the conservation law 2.19, the K values of phonons have to be near to the central (Γ) point of the Brillouin zone.

Vibrations of diamond and graphite

If the primitive lattice exhibits n atoms, there exist $3n$ modes separated to the 3 acoustical and $3n-3$ optical ones [21]. The primitive unit cell of diamond contains two atoms (see fig. 2.7). Only three $(3 \times 2 - 3)$ optical modes are expected. According to [22],

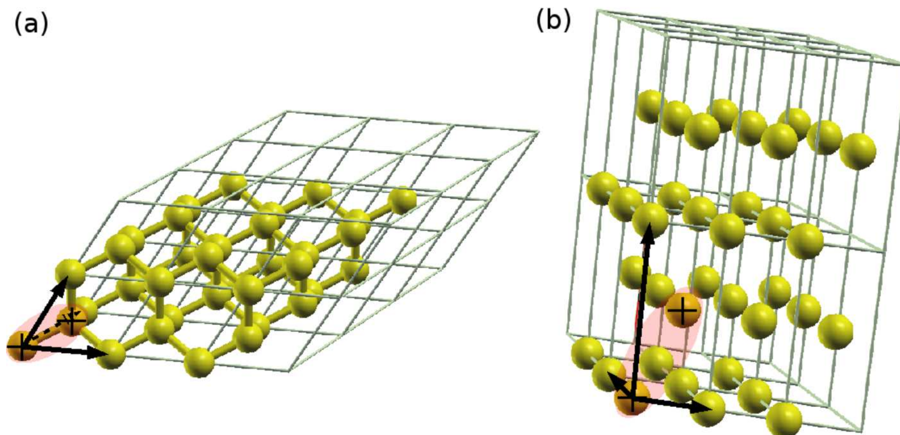

Figure 2.7: Diamond (a) and graphite (b) primitive unit cells with repetition. The arrows assign primitive vectors and the crosses denote a base of the lattice.

these vibrations belong to the triply degenerated F_{2g} species which are Raman active. Raman spectra of diamond at $K = 0\,\mathrm{cm}^{-1}$ exhibit only one peak at 1332 cm^{-1} (see 2.8).

Graphite consists of weakly bounded sheets parallel to each other. We can take into account only one isolated sheet. The whole sheet can be created by repeating a unit cell containing two atoms. The $(3{\times}2 - 3)$ vibrations are grouped into Raman inactive B_{2g} and Raman active E_{2g} [22]. The Raman spectrum of graphite exhibits only one peak at $1580\,\mathrm{cm}^{-1}$ (fig. 2.8). The intensity of an inter-sheet vibration peak of graphite

is negligible to the sheet vibration peak and so the peak is not present in the Raman spectra.

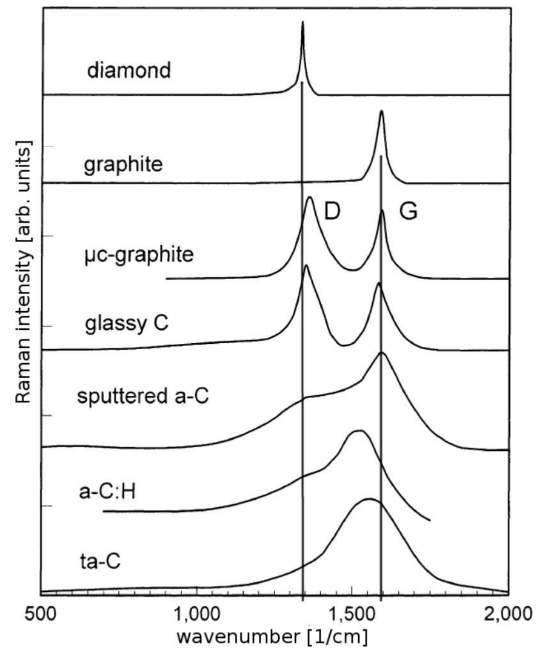

Figure 2.8: Raman intensity of diamond, graphite and different forms of DLC [3].

2.4. Spectroscopic reflectivity

Spectroscopic reflectivity is a measurement technique used to determine optical characteristics and thickness of mono- and multi-layers from reflective spectra. The reflection

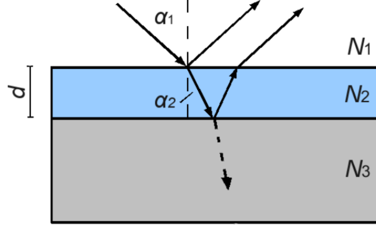

Figure 2.9: A scheme of a single thin film layer on the substrate. Values N_1, N_2 and N_3 denote the complex index of refraction of the ambient environment, the thin film layer and the substrate, respectively.

coefficient R is described by Fresnel coefficients

$$r_{12\parallel} \equiv \frac{E_{r\parallel}}{E_{0\parallel}} = \frac{N_2 \cos\alpha_1 - N_1 \cos\alpha_2}{N_2 \cos\alpha_1 + N_1 \cos\alpha_2}, \tag{2.20}$$

for the light with the electric field vector in the plane of incidence and

$$r_{12\perp} \equiv \frac{E_{r\perp}}{E_{0\perp}} = \frac{N_2 \cos\alpha_2 - N_1 \cos\alpha_1}{N_2 \cos\alpha_2 + N_1 \cos\alpha_1}, \tag{2.21}$$

for the light polarised perpendicular to the plane of incidence [23]. There $E_{0\parallel,\perp}$ and $E_{r\parallel,\perp}$ are corresponding components of the incoming and reflected light and $N = n - \mathrm{i}k$ is the complex index of refraction (see fig. 2.9). Usually, the reflectivity measurement is performed with the incidence angle $\alpha_1 = 0$ (perpendicular to the sample surface). According to Snell's law $n_1 \sin\alpha_1 = n_2 \sin\alpha_2$ for this case we get the refraction angle $\alpha_2 = 0$. Equations 2.20 and 2.21 are then simplified as

$$r_{12\parallel} = \frac{N_2 - N_1}{N_2 + N_1}, \tag{2.22}$$

$$r_{12\perp} = \frac{N_2 - N_1}{N_2 + N_1} \tag{2.23}$$

The reflection coefficient R of a single thin film layer on a substrate (fig. 2.9) is given by [24].

$$R = \frac{r_{12} + r_{23}\exp(-\mathrm{i}2\beta)}{1 + r_{12}r_{23}\exp(-\mathrm{i}2\beta)}, \tag{2.24}$$

where $r_{23} = (N_3 - N_2)/(N_3 + N_2)$, β is the phase difference between the beams reflected at the upper and the lower film interface and is given by

$$\beta = 2\pi\frac{d}{\lambda}N_2. \tag{2.25}$$

The measured quantity is called reflectance $\Re$ and is given by

$$\Re = |R|^2\,. \tag{2.26}$$

2.4.1. Index of refraction and extinction coefficient

Two models of finding optical properties and electronic structure from reflectance measurements has been taken into account in this work. First, the model proposed by A.R. Forouhi and I. Bloomer (FB model) [25, 26] and second, the model suggested by Daniel Franta *et al.* (PJDOS model) [27].

FB model:

This model is based on a quantum mechanical theory of absorption, from which a general expression is deduced for the extinction coefficient k. The energy of a band gap E_g is identified as the energy where k has an absolute minimum. Index of refraction n and extinction coefficient k are bounded through the Kramers-Kronig relations. Equations for n and k are

$$n(E) = n(\infty) + \frac{B_0 E + C_0}{E^2 - BE + C}, \tag{2.27}$$

$$k(E) = \frac{A(E - E_g)^2}{E^2 - BE + C}, \tag{2.28}$$

where

$$B_0 = \frac{A}{Q}\left(-B^2/2 + E_g B - E_g^2 + C\right), \tag{2.29}$$

$$C_0 = \frac{A}{Q}\left((E_g^2 + C)B/2 - 2E_g C\right), \tag{2.30}$$

$$Q = \frac{1}{2}\sqrt{(4C - B^2)}. \tag{2.31}$$

For an amorphous structure $k(E)$ and $n(E)$ can be determined using the parameters A ,B, C, E_g, $n(\infty)$, where E_g is the energy of the band gap and $n(\infty)$ is the index of refraction for infinite frequency.

PJDOS model:

This model is based on the parametrisation of the valence band (see figure 2.10), where only two transitions $\sigma \rightarrow \sigma^*$ and $\pi \rightarrow \pi^*$ are taken into account [27]. Imaginary and real components of permitivity are

$$\varepsilon_{\mathrm{i,j\rightarrow j^*}}(E) = \begin{cases} \frac{30Q_{\mathrm{j}}(E-E_{\mathrm{gj}})^2(E-E_{\mathrm{hj}})^2}{(E_{\mathrm{hj}}-E_{\mathrm{gj}})^5 E^2} \in E_{\mathrm{gj}} < E < E_{\mathrm{hj}} \\ 0 \qquad \text{otherwise,} \end{cases} \tag{2.32}$$

$$\varepsilon_{\mathrm{r,j\rightarrow j^*}}(E) = \frac{60Q_j^2}{\pi(E_{\mathrm{hj}} - E_{\mathrm{gj}})^5}\left[B(E)\ln\left|\frac{E+E_{\mathrm{hj}}}{E+E_{\mathrm{gj}}}\right| + C(E)\ln\left|\frac{E-E_{\mathrm{hj}}}{E-E_{\mathrm{gj}}}\right| - D(E)\right], \tag{2.33}$$

where

$$B(E) = \frac{Y(E) + X(E)}{2E^2}, \tag{2.34}$$

$$C(E) = \frac{Y(E) - X(E)}{2E^2}, \tag{2.35}$$

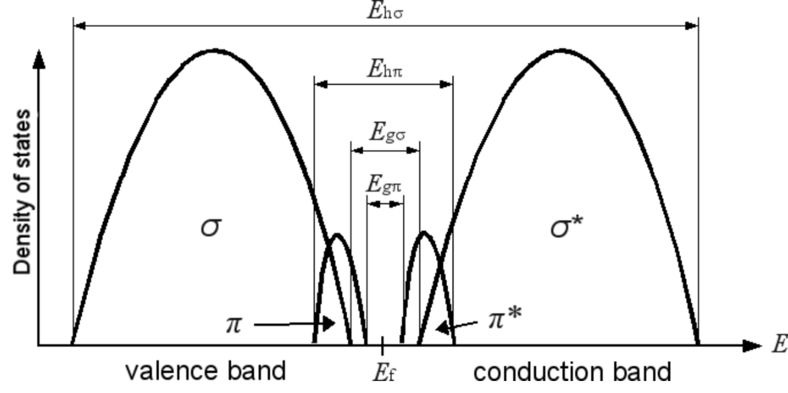

Figure 2.10: The DOS (Density of States) model of valence and conduction bands of DLC. This model is comparable with a valence band measured by XPS and shown in figure 3.23.

$$D(E) = \frac{E_{gj}^2 E_{hj}^2}{E^2} \ln\left|\frac{E_{hj}}{E_{gj}}\right| + \frac{3(E_{hj}^2 - E_{gj}^2)}{2}, \tag{2.36}$$

$$X(E) = 2E[E_{hj}(E_{gj}^2 + E^2) + E_{gj}(E_{hj}^2 + E^2)], \tag{2.37}$$

$$Y(E) = E^2(E_{hj}^2 + E_{gj}^2 + 4E_{gj}^2 E_{hj}^2 + E^2) + E_{gj}^2 E_{hj}^2. \tag{2.38}$$

Where j denotes π, σ and j^* denotes π^*, σ^*. The complex dielectric function ε of DLC is then given by

$$\varepsilon(E) = 1 + \varepsilon_{\pi\to\pi^*}(E) + \varepsilon_{\sigma\to\sigma^*}(E). \tag{2.39}$$

Index of refraction n and extinction coefficient k can be then calculated by the relations [28]

$$n = \sqrt{\frac{1}{2}\varepsilon_{\mathrm{r}} + \frac{1}{2}\sqrt{\varepsilon_{\mathrm{r}}^2 + \varepsilon_{\mathrm{i}}^2}}, \tag{2.40}$$

$$k = \sqrt{-\frac{1}{2}\varepsilon_{\mathrm{r}} + \frac{1}{2}\sqrt{\varepsilon_{\mathrm{r}}^2 + \varepsilon_{\mathrm{i}}^2}}. \tag{2.41}$$

Using 2.22 – 2.26, 2.32 – 2.41 and the formula $N = n - \mathrm{i}k$, one can obtain parameters Q_σ, Q_π, $E_{h\sigma}$, $E_{g\sigma}$, $E_{h\pi}$ and $E_{g\pi}$ connecting the real reflectance spectra with the density of states in the valence band.

3. Experiment

3.1. Deposition

All depositions were performed in the *Oxford Plasmalab System 100*. The equipment consists of a vacuum chamber furnished by 4 feedthroughs. Two of them are at the bottom and two at the side. One of the bottom feedthroughs serves for the insertion of a wire probe for the measurement of the potential at a cathode U_1, one of the side feedthroughs serves for the measurement of temperature at the cathode or of plasma potential U_p. The second of the side feedthroughs is a window port for the visual inspection of the plasma inside the chamber.

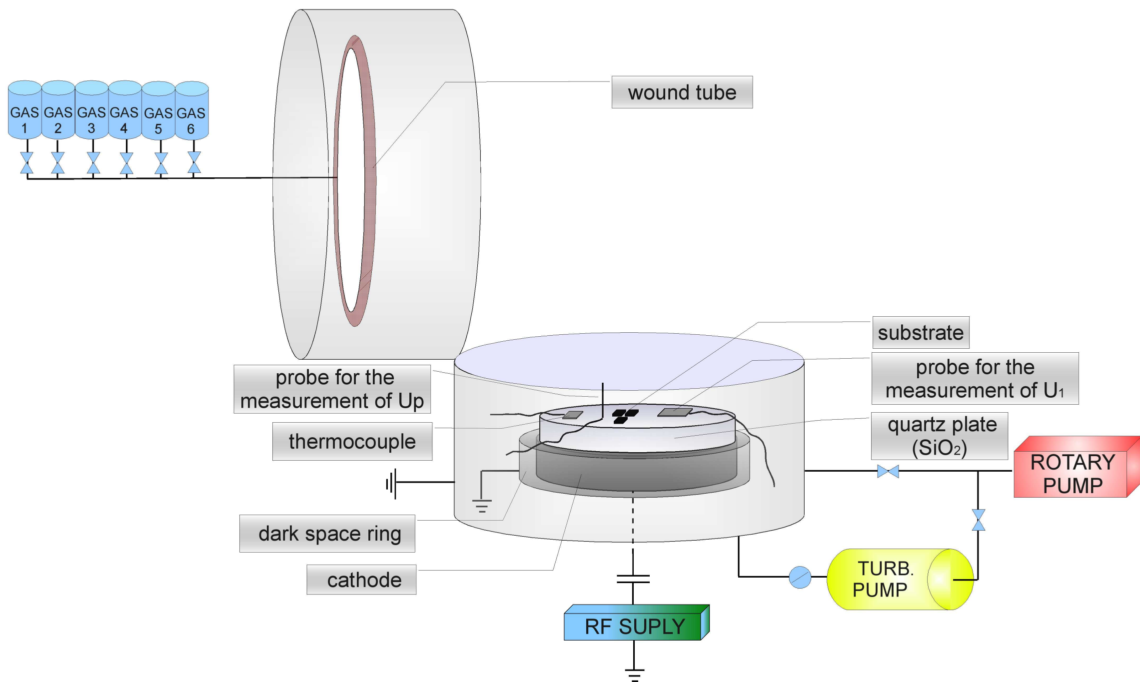

Figure 3.1: A layout of a deposition chamber.

Vacuum is provided by one rotation oil pump (RP) and a turbo-molecular pump (TP). At first only a RP runs. After achievement of a pressure of 30 mTorr the valve among the RP and the chamber is closed and the valves among RP and TP and among TP and the chamber are opened. The resulting base pressure in the vacuum chamber is higher than 3×10^{-7} mbar, and the pressure 6×10^{-6} mbar is archived during four-hour pumping by TP. The vacuum chamber is of a cylindrical shape with a diameter of 380 mm, the height of both the lower and detachable upper part is 130 mm. In this upper part of the chamber is a wound tube with holes for injection of a gas being connected to six bottles of compressed gas. Between each bottle and the chamber is a computer-regulated valve enabling monitoring gas flow to the chamber. A circular cathode with a diameter of 200 mm is at the bottom part of the chamber and is connected via a capacitor to a RF supply with a maximum input power of 350 W. A cylindrical annulus called *a dark space ring* being similarly to the chamber grounded is around the cathode

in a distance of 1 mm. This configuration leads to more homogeneous plasma in the area of the cathode.

During the deposition, a quartz plate (SiO_2) with a thickness of 10 mm was put on the cathode. This chamber was primarily made for etching. Etching is a physical process leading to removing topmost layers. The main difference between etching and deposition processes is that etching uses higher bias voltage. This bias voltage is lowered by the quartz plate.

A metal plate with a size of $25 \times 50 \times 1$ mm was placed on the top of the quartz plate, in order to measure the potential at the cathode surface. This plate was connected to the feedthrough by a wire covered by ceramic rings protecting it against plasma influence. Further, the surface was furnished by a thermocouple for temperature measurements. Later, a thermocouple was interchanged by a probe for the measurement of the plasma potential U_{p} (a coaxial cable connected by an outer wire to the earth). The end of the inner wire was placed into the plasma. Samples were fixed to the middle of the cathode, thus avoiding the role of non-homogeneous plasma areas at the cathode borders.

Four series, each of them consisting of 16 depositions (64 together) and one additional series of a-DLC:H deposition were accomplished. Substrates were cut from Si (100) wafers to a size of 0.5×0.7 mm and subsequently cleaned. The samples were cleaned in distilled water, then in 5% solution of *Neutrocon* detergent and in the end in iso-propanol. Each cleaning procedure was performed in an ultrasonic bath for a duration of 10 min. Before insertion of samples into the chamber the substrate was heated up in the bath of iso-propanol close to temperature of 40°C, dried up by flow of helium and carefully masked by a sticky tape matched to vacuum conditions. The tape covered 1/3 of a sample area and was used in view of the measurement of the film thickness.

Closely before deposition, the base pressure p_{min} in the vacuum chamber was in the range of $(9 \times 10^{-7} - 9 \times 10^{-6})$ mbar. Low pressure was necessary for desorption of impurities from the substrate surface and minimisation of residual gas atoms. No cleaning of the substrate in the chamber was performed (for instance ion-beam etching removing an oxide from Si surface). Thus it was assumed that the Si surface was passivated by native SiO_2 oxide.

Deposition was controlled by three parameters: by pressure p in the chamber, input RF power P and the relative hydrogen flow $H_2/(CH_4+H_2)$ in the intervals (20–100) mTorr, (50–200) W and (28–90) %, respectively. The total gas flow rate was fixed to 20 SCCM. Each deposition was performed for a different combination of p, P and $H_2/(CH_4+H_2)$. Several additional parameters were recorded at the beginning and at the end of deposition: cathode potential U_1 and its amplitude $U_{1\mathrm{A}}$ (both measured by an oscilloscope on the quartz plate) and temperature T (only D series - fig. 3.2) measured twice during the deposition as well. Temperature did not exceed 300 °C, at which desorption of hydrogen from the DLC surface begins [3]. In figure 3.2, it is seen that temperature during the 30 minutes did not reach 60°C. In tables 3.1, 3.2, the results from depositions are shown. There are shown operational parameters (pressure during deposition p , input RF power P, base pressure before deposition p_{min}) and dependent parameters (cathode potential U_1 and its amplitude $U_{1\mathrm{A}}$ at the beginning and at the end of depositions, temperature (only series D)). Difference between U_1 at the beginning and at the end may be caused due to sooting of the metal plate used for measuring this potential. During deposition, U_1 was declining consistently to zero. The same behaviour

has been observed during measurements of the plasma potential U_p by the coaxial wire. Therefore, after each deposition process, the vacuum chamber was cleaned. According

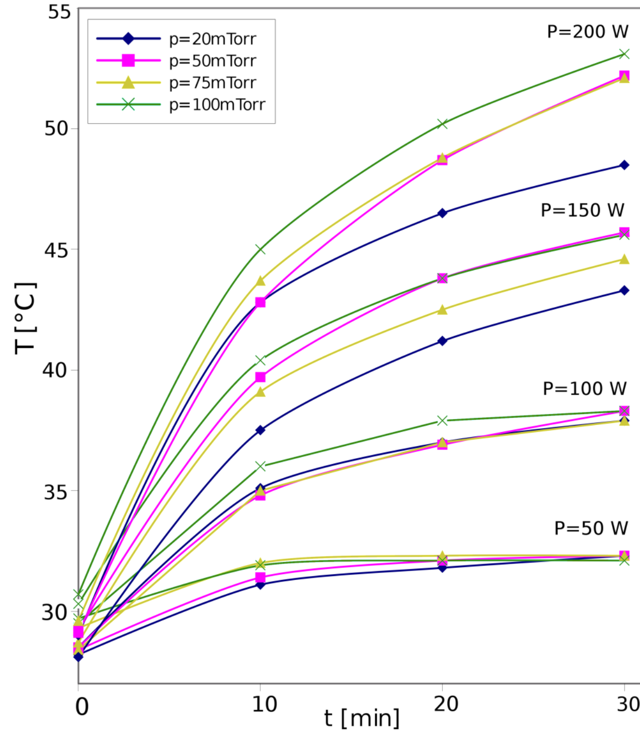

Figure 3.2: Temperature measured during deposition (series D), P is the input RF power and p is the pressure during deposition.

to [29], the relation between U_1 and U_p is

$$U_\mathrm{p} = \frac{U_1 + U_{1\mathrm{A}}}{2}. \tag{3.1}$$

The graphical illustration is seen in figure 3.3. It is possible to determine the plasma potential U_p without the need of a measurement. The knowledge of U_1 and $U_{1\mathrm{A}}$ is sufficient as can be seen from the figure. This was confirmed by an experiment. In figure 3.4 we can see graphs showing how the cathode potential U_1 changes with pressure p and input RF power P.

The plasma potential U_p has been measured at the same time as U_1 and $U_{1\mathrm{A}}$. The measured U_p is compared with U_p given by theory (eqn. 3.1). The results are shown in figure 3.5. It is clearly seen, that the measured plasma potential and that one from the theory are close each other except several measurements (samples A14, B14, C14). The bias voltage U_b is then given by relation $U_\mathrm{b} = U_1 - U_\mathrm{p}$ where the plasma potential U_p was calculated according to equation 3.1.

The thickness of films deposited on silicon has been measured by a profilometer *Taylor-Hobson Talystep* immediately after deposition. The results (thickness and deposition rate) are shown in table 3.3. The thickness is displayed against the pressure p and power P in figure 3.6. With an increasing power and of a fixed pressure the ratio ion/atom increases. More ions impact the surface and stick there. The result is the higher deposition rate and higher thickness. The second case occurs for the constant

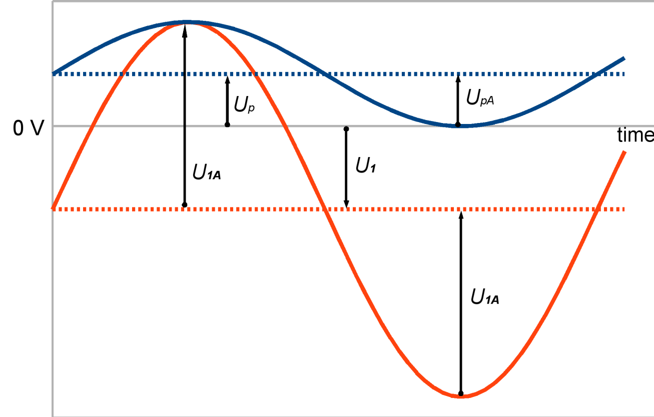

Figure 3.3: Relation between the plasma U_p and the cathode potential U_1.

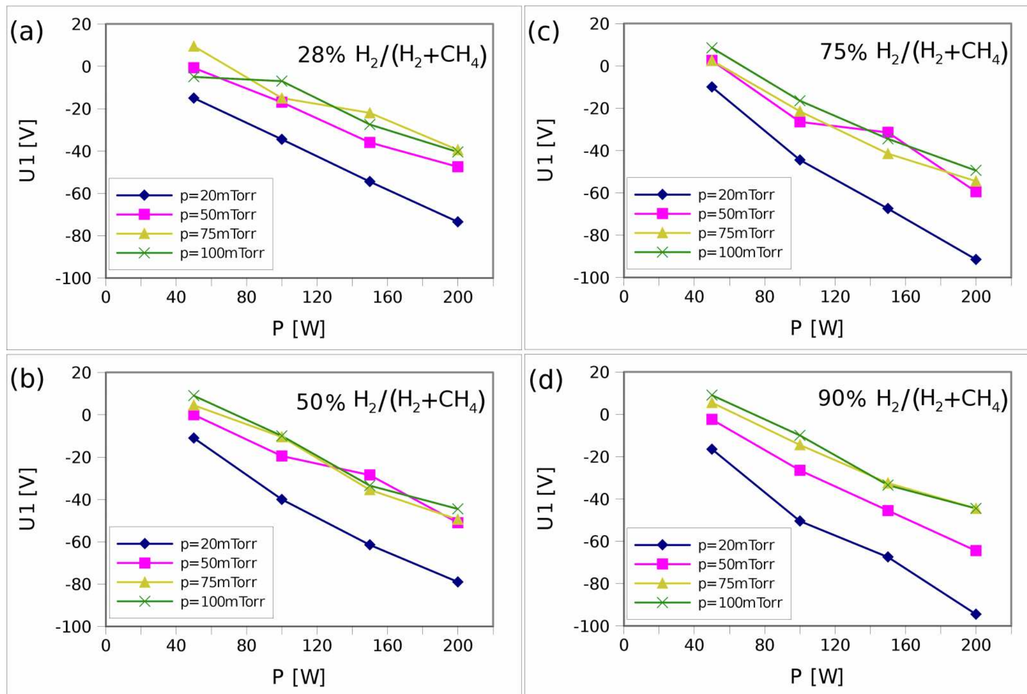

Figure 3.4: Potential U_1, (a) series A, (b) series B, (c) series C, (d) series D.

power and increasing pressure. More atoms results in more ions impacting the surface. Thus the deposition rate increases as well. With the higher ratio of hydrogen to methane mixture the resulting thickness of DLC gets smaller. Pure hydrogen atoms cannot create stable solids at atmospheric pressure and room temperature. Hydrogen has to create bonds with another type of atoms, in case of DLC with carbon. The content of carbon atoms in a gas mixture is low which results in a lower deposition rate. In figure 3.7, evolution of film thickness (or deposition rate) with bias voltage U_b is shown. The thickness is smaller for lower $H_2/(CH_4+H_2)$ flow than the higher one and the positions of maxima are approximately at the same value of U_b =-100 V.

(a)

Name	p	P	p_{min}	U_1 begin	U_1 end	U_{1A} begin	U_{1A} end
	[mTorr]	[W]	[mbar]	[V]	[V]	[V]	[V]
A11	20	50	1.80E-05	-15	-11	94	93
A12	20	100	8.00E-06	-35	-25	130	123
A13	20	150	3.40E-06	-55	-37	147	145
A14	20	200	1.20E-06	-74	-67	170	168
A21	50	50	1.10E-06	-1	2	85	85
A22	50	100	2.40E-06	-17	-8	116	115
A23	50	150	5.60E-06	-36	-19	138	136
A24	50	200	1.10E-06	-48	-32	159	158
A31	75	50	4.00E-06	10	7	84	82
A32	75	100	5.50E-06	-15	-5	114	112
A33	75	150	6.20E-06	-22	-10	128	127
A34	75	200	2.80E-06	-40	-21	152	148
A41	100	50	7.40E-06	-5	-6	74.4	74
A42	100	100	5.20E-06	-7	-4	110	110
A43	100	150	1.10E-06	-28	-13	131	129
A44	100	200	1.00E-06	-41	-33	148	147

(b)

Name	p	P	p_{min}	U_1 begin	U_1 end	U_{1A} begin	U_{1A} end
	[mTorr]	[W]	[mbar]	[V]	[V]	[V]	[V]
B11	20	50	3.60E-06	-11	-4	92	93
B12	20	100	5.20E-06	-40	-23	126	123
B13	20	150	3.60E-06	-62	-40	152	148
B14	20	200	1.00E-06	-79	-56	171	167
B21	50	50	3.40E-06	0	-2	86	85
B22	50	100	1.10E-06	-20	-9	115	115
B23	50	150	3.20E-06	-29	-18	135	136
B24	50	200	7.00E-07	-51	-26	158	156
B31	75	50	1.00E-06	5	4	87	86
B32	75	100	5.00E-06	-11	-7	113	111
B33	75	150	2.50E-06	-36	-15	137	133
B34	75	200	1.00E-06	-50	-28	154	152
B41	100	50	3.40E-06	9	3	82	82
B42	100	100	5.40E-06	-10	-8	111	110
B43	100	150	8.00E-06	-34	-18	133	130
B44	100	200	7.70E-07	-45	-22	153	147

Table 3.1: Deposition, (a) series A — flow of H_2=5.6 SCCM and CH_4=14.4 SCCM $\Rightarrow$ the relative hydrogen flow $H_2/(CH_4+H_2)$=28%, (b) series B — flow of H_2=10 SCCM and CH_4=10 SCCM $\Rightarrow$ $H_2/(CH_4+H_2)$=50%. Deposition time t=30 min, pressure p, RF power P, pressure before deposition $p_{\min}$, cathode potential U_1 and its amplitude U_{1A} at the beginning and the end of deposition.

(a)

Name	p	P	p_{min}	U_1 begin	U_1 end	U_{1A} begin	U_{1A} end
	[mTorr]	[W]	[mbar]	[V]	[V]	[V]	[V]
C11	20	50	2.60E-06	-10	-10	89	89
C12	20	100	2.60E-06	-45	-37	126	123
C13	20	150	1.10E-06	-68	-52	154	148
C14	20	200	1.10E-06	-92	-71	174	168
C21	50	50	3.40E-06	3	-5	83	84
C22	50	100	2.00E-06	-27	-18	120	117
C23	50	150	2.70E-06	-32	-28	139	138
C24	50	200	1.20E-06	-60	-42	168	154
C31	75	50	3.20E-06	3	-3	88	85
C32	75	100	3.40E-06	-22	-17	118	114
C33	75	150	1.30E-06	-42	-29	141	135
C34	75	200	3.00E-06	-55	-37	161	154
C41	100	50	3.00E-06	9	2	87	84
C42	100	100	7.50E-07	-17	-15	117	112
C43	100	150	2.20E-06	-35	-23	138	134
C44	100	200	1.20E-06	-50	-37	150	147

(b)

Name	p	P	p_{min}	U_1 begin	U_1 end	U_{1A} begin	U_{1A} end	T [°C]			
	[mTorr]	[W]	[mbar]	[V]	[V]	[V]	[V]	0 min	10 min	20 min	30 min
D11	20	50	4.40E-06	-17	-19	89	86	28.2	31.1	31.8	32.3
D12	20	100	9.60E-07	-51	-48	125	122	28.5	35.1	37.0	37.9
D13	20	150	7.00E-07	-68	-62	153	145	28.1	37.5	41.2	43.3
D14	20	200	2.90E-06	-95	-86	173	167	29.0	42.8	46.5	48.5
D21	50	50	9.30E-07	-3	-5	91	90	28.4	31.4	32.1	32.3
D22	50	100	2.30E-06	-27	-22	120	114	28.5	34.8	36.9	38.3
D23	50	150	3.00E-06	-46	-37	141	139	29.2	39.7	43.8	45.7
D24	50	200	9.80E-07	-65	-52	162	158	29.1	42.8	48.7	52.2
D31	75	50	1.90E-06	5	0	88.5	86	29.3	32.0	32.3	32.3
D32	75	100	9.70E-07	-18	-15	116	114	28.4	35.0	37.0	37.9
D33	75	150	2.70E-06	-37	-27	136	134	28.7	39.1	42.5	44.6
D34	75	200	7.30E-07	-56	-42	153	151	29.6	43.7	48.8	52.1
D41	100	50	2.30E-06	6	0	84	82	29.7	31.9	32.1	32.1
D42	100	100	9.50E-07	-15	-13	113	110	29.5	36.0	37.9	38.3
D43	100	150	2.80E-06	-33	-21	136	132	30.3	40.4	43.8	45.6
D44	100	200	9.50E-07	-45	-34	152	147	30.7	45.0	50.2	53.1

Table 3.2: Deposition, (a) series C — flow of H_2=15 SCCM and CH_4=5 SCCM ⇒ the relative hydrogen flow $H_2/(CH_4+H_2)$=75%, (b) series D — flow of H_2=18 SCCM and CH_4=2 SCCM ⇒ $H_2/(CH_4+H_2)$=90%. Deposition time t=30 min, pressure p, RF power P, pressure before deposition $p_{\min}$, cathode potential U_1 and its amplitude U_{1A} at the beginning and the end of deposition.

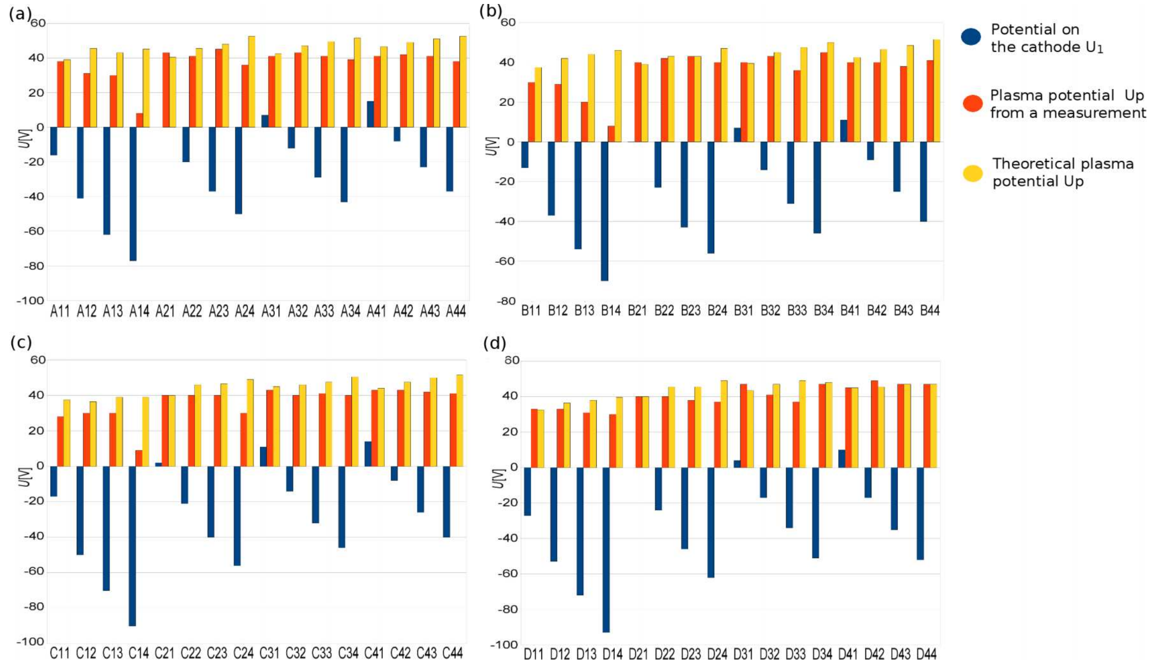

Figure 3.5: Plasma potential from a measurement, plasma potential counted from a theory (eqn. 3.1) and potential on the cathode U_1, (a) series A, (b) series B, (c) series C, (d) series D.

Name	h	r	Name	h	r	Name	h	r	Name	h	r
	[nm]	[nm/min]		[nm]	[nm/min]		[nm]	[nm/min]		[nm]	[nm/min]
A11	113	4	B11	187	6	C11	147	5	D11	61	2
A12	247	8	B12	243	8	C12	220	7	D12	93	3
A13	293	10	B13	340	11	C13	207	7	D13	147	5
A14	300	10	B14	370	12	C14	253	8	D14	127	4
A21	235	8	B21	320	11	C21	227	8	D21	117	4
A22	400	13	B22	440	15	C22	313	10	D22	190	6
A23	487	16	B23	530	18	C23	413	14	D23	200	7
A24	620	21	B24	500	17	C24	447	15	D24	187	6
A31	283	9	B31	353	12	C31	267	9	D31	153	5
A32	520	17	B32	393	13	C32	373	12	D32	180	6
A33	760	25	B33	600	20	C33	367	12	D33	207	7
A34	813	27	B34	573	19	C34	467	16	D34	287	10
A41	313	10	B41	313	10	C41	260	9	D41	135	5
A42	553	18	B42	527	18	C42	360	12	D42	220	7
A43	600	20	B43	600	20	C43	413	14	D43	200	7
A44	773	26	B44	587	20	C44	427	14	D44	253	8

Table 3.3: Thickness h determined by a profilometer and the deposition rate r.

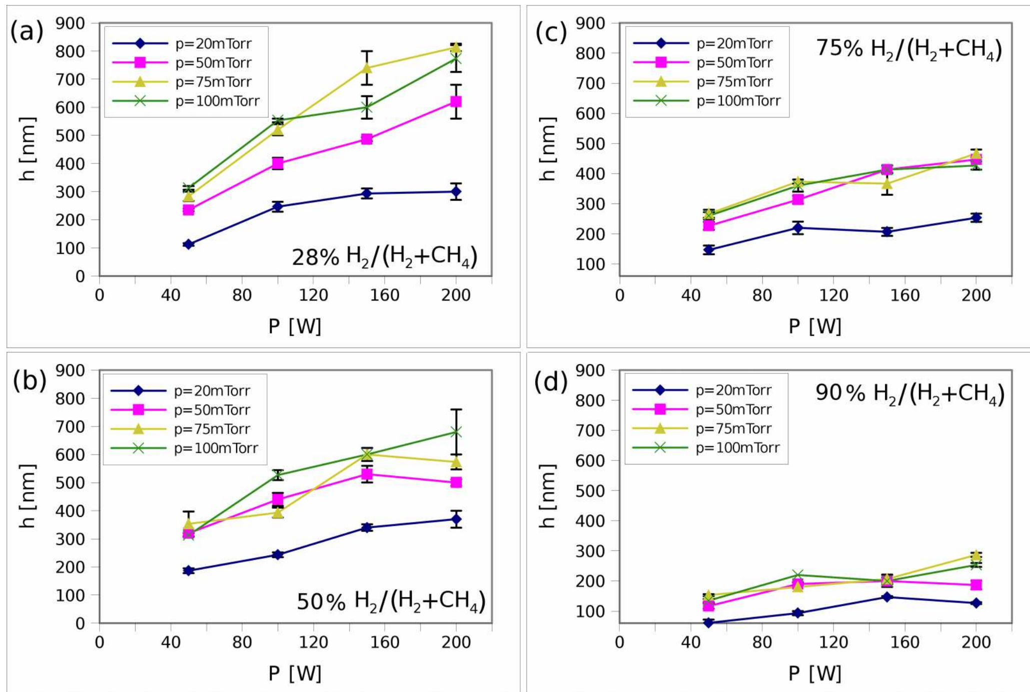

Figure 3.6: Thickness h of DLC films (a) series A, (b) series B, (c) series C, (d) series D.

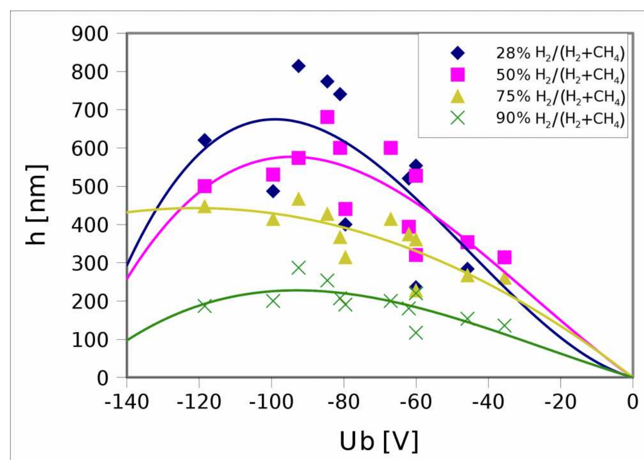

Figure 3.7: Thickness h of DLC films. Maxima in thickness (and deposition rate) occur around $|U_\mathrm{b}|$ =90–110 V for all H_2/CH_4 flows.

3.2. Hardness and scratch

3.2.1. Hardness

Measurements of hardness, reduced modulus and critical loads have been performed with a testing platform *Micro Materials Ltd NanoTest*™. A three-side pyramidal diamond Berkovich indentor has been employed for a nano-hardness test. The diamond area function of the Berkovich indentor was calibrated by an indentation into a fused silica. On each sample, 15 indentations have been performed. A depth-controlled procedure was used and a penetration depth of indentations was set to 15 nm. This constant value was chosen because the pre-indentation testing has shown significant variations of hardness of fused silica with the penetration depth. The constant depth of indentations was kept to avoid this depth-related contribution to the hardness and reduced modulus. As the thinnest film used for the hardness test, the film with a thickness of 113 nm was used (sample A11). It is known that if the penetration depth is chosen higher than 1/10 of the film thickness, then the measured hardness and reduced modulus of a film is substantially influenced by the substrate [30, 31, 32]. The 15 nm penetration depth was to high for the A11 sample, but the smaller penetration depth would be too low to obtain reliable results. The loading and unloading rate was set to 0.01 mN/s, the dwell period at the maximum load was 5 s, the indentor contact velocity 0.2 μm/s and temperature inside the testing chamber 25°C for all samples.

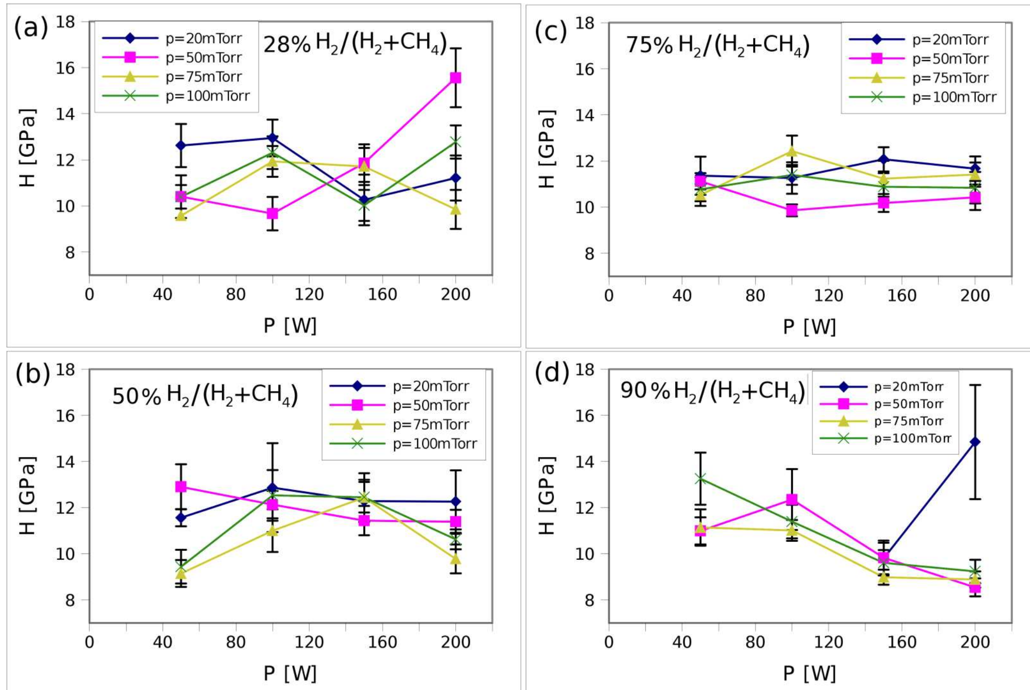

Figure 3.8: Hardness H of DLC films on the silicon substrate, (a) series A, (b) series B, (c) series C, (d) series D.

The results from these measurements did not show any resonable data (fig. 3.8). For this reason, the depositions of four 400 nm thick representative samples from each series have been repeated. Deposition rates were taken from table 3.3. In table 3.4, the operational parameters and the film thickness from that deposition are shown. The

new series is described by an acronym “EXxx”. The first letter “E” represents the new series and “Xxx” means old notation (Xxx ≡ A11, A14, B44 or D11 etc). For example, the sample A11 and EA11 are made under the same conditions. Different in only film thickness and the time of the deposition as well. Although, the aim of the new

Name	p	P	p_{min}	U_1 begin	U_1 end	U_{1A} begin	U_{1A} end	t	h
	[mTorr]	[W]	[mbar]	[V]	[V]	[V]	[V]	[min]	[nm]
EA11	20	50	2.40E-06	-17	-3	88	86	110	573
EA14	20	200	6.50E-06	-60	-33	167	163	40	493
EA41	100	50	1.70E-06	4	3	74	74	40	373
EA44	100	200	5.40E-06	-38	-36	145	142	18	413
EB11	20	50	1.00E-06	-6	4	87	87	95	360
EB14	20	200	8.00E-06	-71	-64	163	163	35	360
EB41	100	50	1.40E-06	11	6	75	76	40	360
EB44	100	200	4.90E-06	-40	-34	148	144	22	427
EC11	20	50	1.20E-06	-12	-3	94	89	90	373
EC14	20	200	3.60E-06	-87	-60	170	164	52	387
EC41	100	50	1.30E-06	13	15	82	81	50	360
EC44	100	200	2.10E-06	-44	-34	150	146	30	467
ED11	20	50	8.10E-06	-17	0	89	92	210	493
ED14	20	200	7.10E-06	-88	-70	164	164	100	360
ED41	100	50	1.20E-06	26	20	79	78	95	387
ED44	100	200	3.00E-06	-43	-25	151	147	50	387

Table 3.4: Deposition of series E. $H_2/(CH_4+H_2)$=28 % — EA, $H_2/(CH_4+H_2)$=50% — EB, $H_2/(CH_4+H_2)$=75% — EC and $H_2/(CH_4+H_2)$=98% — ED, pressure p, RF power P, pressure before starting deposition p_{min}, cathode potential U_1 and its amplitude $U_{1\mathrm{A}}$ at the beginning and at the end of deposition, deposition time t and film thickness h.

deposition was the creation of 400 nm samples, the thicknesses dispersion of series E is 360 nm–573 nm. Hardness and scratch tests have been repeated for the films of series E. During the hardness test the penetration depth was fixed to 35 nm for all samples and fifteen indentations per one sample have been performed. Figure 3.9 shows how hardness H and reduced modulus E_{r} of DLC films change with the bias voltage U_{b}, $H_2/(CH_4+H_2)$ flow and pressure p.

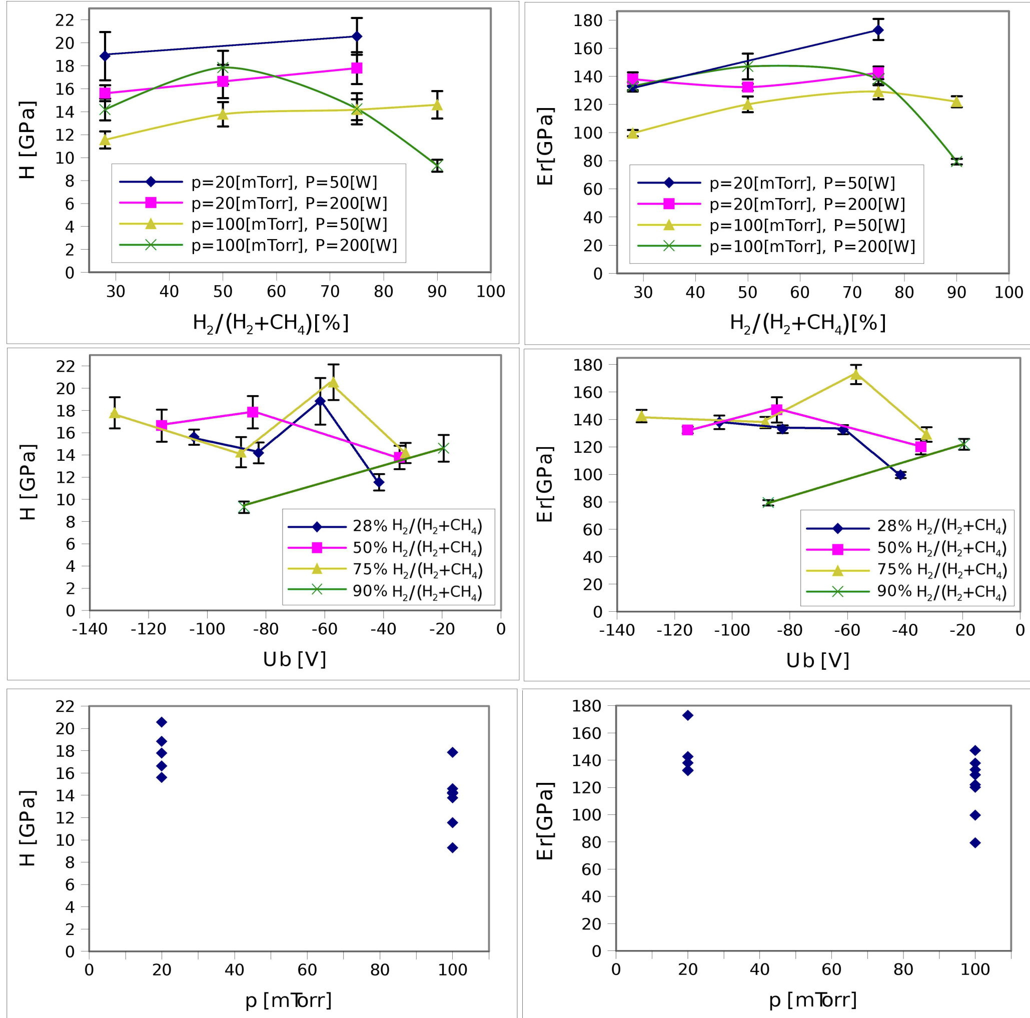

Figure 3.9: Hardness H and reduced modulus E_r against H_2/CH_4 flow, bias voltage U_b and pressure p, (series E).

3.2.2. Scratch test

For a scratch test a sphero-conical diamond indentor of the operating angle 60° and radius 4 μm was used. Three scratch tests per one sample were performed (see fig. 3.10). The scratch length 150 μm was fixed for all samples. During first 20 μm a minimal (scanning) normal force of 0.05 mN was applied. After that the indentor force started to increase with a constant loading rate of 4 mN/s up to 200 mN. This maximal force was reached after the 100 μm long track and for the last 30 μm the indentor force was constant (200 mN). After removing the samples from a sample holder, an optical microscope was used to observe the scratches. A typical picture of scratches is shown in figure 3.10. Here it is clearly seen, how a DLC film can protect the substrate (silicon) against scratching. More detailed view of the scratches is in figure 3.11. The picture was taken by a scanning

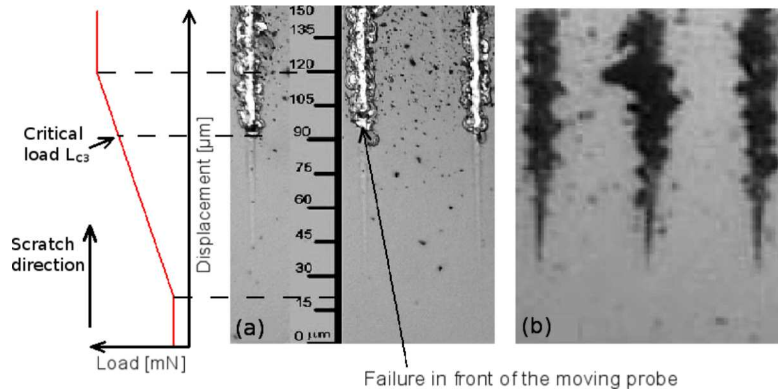

Figure 3.10: Optical image of the surface after the scratch test with DLC on silicon (a). Optical image after the scratch test of the silicon surface only (b).

electron microscope (SEM). Lateral cracking in figure 3.11 (c) indicates a hard brittle coating.

The critical load Lc_3 corresponding to the "*failure in front of the moving probe*" increases with the thickness of a deposited film as a linear function $Lc_3(h)$, where h is the thickness. This is valid only in a small range of thicknesses. The additional parameter Lc_3/h is introduced for comparison of scratch resistivity. Function Lc_3/h is not suitable for comparing the films with a high thickness dispersion. All of our samples cover a thickness range of (50–800) nm and the relation is rather parabolical $Lc_3(h^2)$ than linear (see fig. 3.12). We can take into account only a series E (see squares in fig. 3.12) which represents a lower range of thicknesses and we can assume a linear relationship. Lc_3/h is different for a series E, where the thickness of DLC films is close to 400 nm and for the series A,B,C,D where the thickness covers the (50–800) nm range. The function Lc_3/h is not proper for comparison of films with high thicknesses dispersion! The parameter Lc_3/h allowing the comparison of scratch resistivity for the samples with different thicknesses is thus more relevant for the series E.

Figure 3.12 shows the critical load Lc_3, normalised critical load Lc_3/h against the bias voltage U_{b} and Lc_3/h against the $H_2/(CH_4{+}H_2)$ flow for the series E. The slope of the variable $Lc_3(U_{\mathrm{b}})$ curve may be influenced by hardness growing with the increasing absolute value of bias voltage U_{b}.

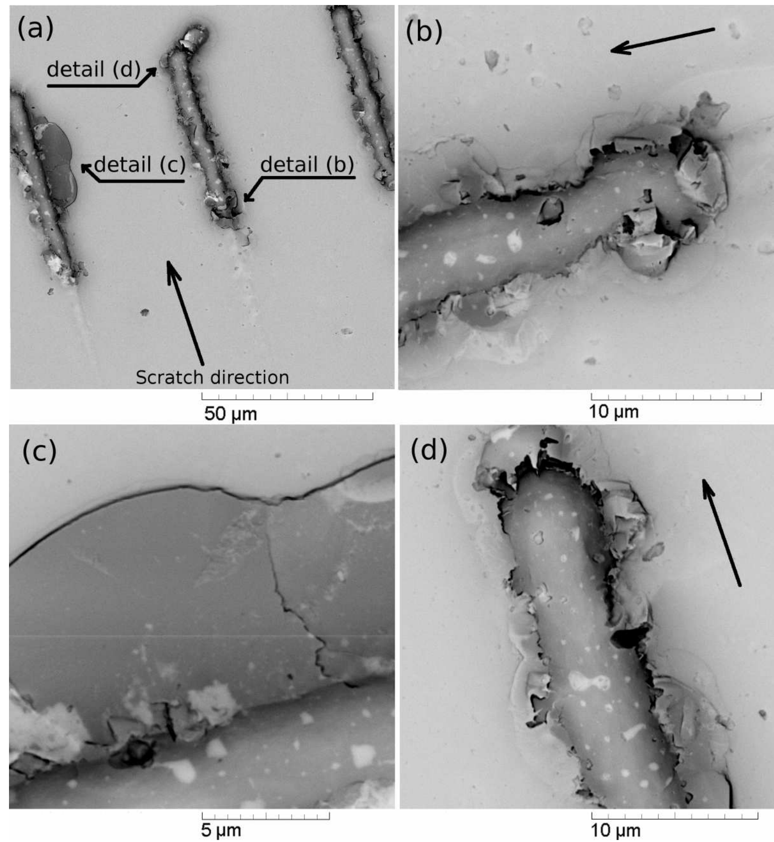

Figure 3.11: SEM images of the sample EA11 with scratches. Overview (a) of the scratches after the scratch test. Three scratches on each sample were done. The path length of the probe was 150 μm. The picture (a) shows the last 100 μm of the scratch. There is clearly seen failure in front of the moving probe. In (b), there is a detail of this failure. On (c), there is a detail of cracking along a lateral side of the scratch, (d) shows a detail of the end of the scratch. The long-black arrows mark the scratch direction.

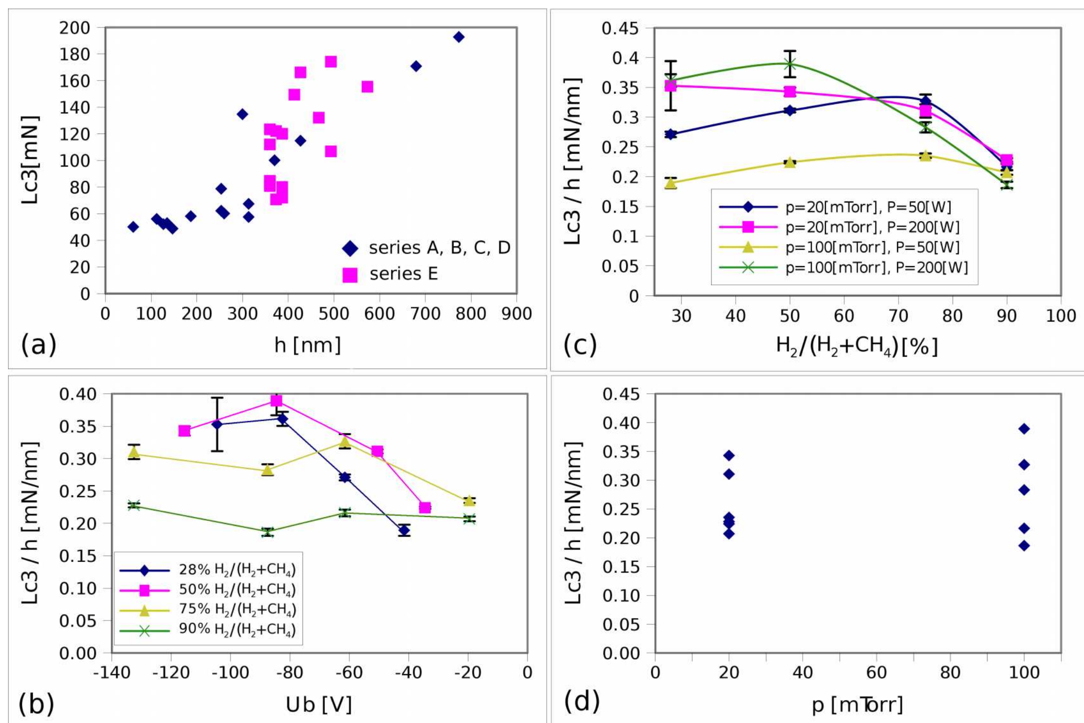

Figure 3.12: Critical load Lc_3 (a) as a function of film thickness — (series A, B, C, D, E), normalised load Lc_3/h (b) against bias voltage U_b — (series E), Lc_3/h (c) against H_2/CH_4 flow — (series E), Lc_3/h (d) against pressure p — (series E).

3.3. Photo-electron spectroscopy

3.3.1. C $1s$ core level spectroscopy for sp^3 content determination

XPS spectra were obtained with using an analyzer *Thermo Fisher Scientific* **Inc.** *ESCALAB 250*. Each C $1s$ — core level peak of the DLC film of series A, B, C, D was scanned under the following conditions: constant pass energy PE=20 eV, energy step 0.1 eV, dwell time 0.05 s and 5 scans at each energy. The work function of the analyzer detector was 4.2 eV. The resolution of the analyzer is given by the relation $\delta E = 0.018 \cdot PE = 0.018 \cdot 20 = 0.36$ eV. The collecting angle was adjusted to 90°(perpendicular to the sample surface). Energy of electrons hitting the anode was 15 keV, input power of the X-ray gun 150 W and the diameter of the X-ray beam at the sample surface 500 μm. Before inserting the sample into the vacuum chamber, a gold mask was deposited on it to fabricate a DLC-gold grid. The base pressure was $5 \cdot 10^{-10}$ mbar. After filling the chamber with argon gas ($4 \cdot 10^{-8}$ mbar), a electron gun bombarding the surface by low-energy electrons (flood gun) was turned on (filament current 1.6 A, emission current 0.1 mA) to compensate a positive charge developed on the surface during measurements of insulating materials and semiconductors. In fig. 3.13, an XPS image of measured area (gold – black points, DLC layer – white) is shown.

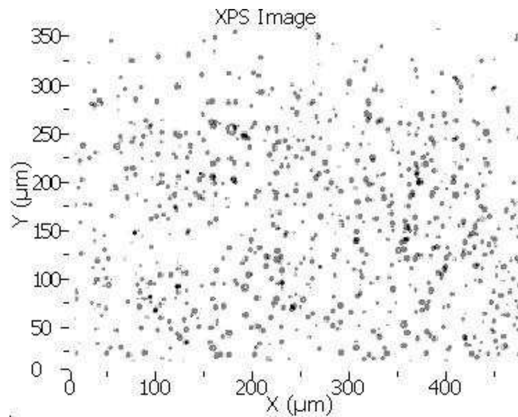

Figure 3.13: XPS image of gold – black points on a DLC layer – white.

In figure 3.14 the typical wide scan for a sample D33 is shown. There is a gold dublet peak represented the Au $4f^{7/2}$ peak with an energy of 84 eV and Au $4f^{5/2}$ peak at 87.8 eV, further carbon C $1s$ (285 eV), gold dubled peak Au $4d^{5/2}$ (535 eV) and Au $4d^{3/2}$ (354 eV), oxide O $1s$ peak (531 eV), gold Au $4p^{3/2}$ (547 eV), oxide Auger O KL1 (980 eV) and carbon C KL1 (1220 eV).

Generation of photoelectrons corresponding to the dublets leads to the vacancies in the $p^{1/2}$, $p^{3/2}$, $d^{3/2}$, $d^{5/2}$, $f^{5/2}$, $f^{7/2}$. The spin orbit splitting ratio is 1/2 for p levels, 2/3 for d levels and 3/4 for f levels [33].

The commercial software for controlling XPS equipment, data acquisition and processing *Advantage* was used only for shifting the C $1s$ peak according to a reference peak Au $4f^{7/2}$ at energy 84 eV (source NIST — National Institute of Standards and Technology). All data C $1s$, O $1s$, Auger K-V-V and the valence band were saved in the *xls* format for processing in the system *MatLab*® software. This approach was chosen, since a big amount of information was necessary to work up and *MatLab* enables to

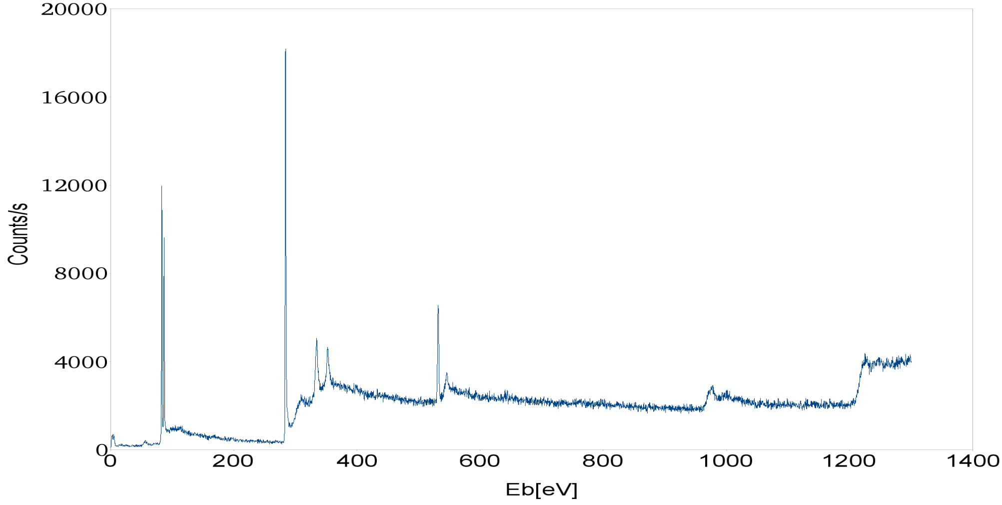

Figure 3.14: A wide survey scan (a sample D33).

make all procedures semi-automatic and fast. Many software procedures were designed to process these data. An important part of XPS spectra processing is elimination of the background from the areas of interest. For this purpose the Shirley background has been chosen [34]. The form of Shirley background is

$$S(E) = I_2 + k\frac{A_2(E)}{A_1(E) + A_2(E)},$$

where $k = I_1 - I_2$, I_1 and I_2 are the starting and final intensity of selected range in the spectrum, respectively. A_1 and A_2 are defined

$$A_1(E) = \int_{E(I_1)}^{E} I(E') \cdot \mathrm{d}E',$$

$$A_2(E) = \int_{E(I_1)}^{E(I_2)} I(E) \cdot \mathrm{d}E - \int_{E(I_1)}^{E} I(E') \cdot \mathrm{d}E'.$$

In figure 3.15, an example of removing the background in the valence band is shown. Further, a fitting function GL (Gauss-Lorentz) without tail mixing was created, especially for fitting C 1s peak (the sum of 3 peaks) and the valence band (9 peaks). The fitting GL function was taken from [35].

$$GL(E) = \frac{h}{\left(1 + \frac{M(E-E_0)^2}{s^2}\right) \cdot \exp\left((1-M)\frac{\ln 2(E-E_0)^2}{s^2}\right)}, \tag{3.2}$$

where h is the height of the peak, M is Gauss/Lorentz mixing ratio (1 for 100% Lorentzian and 0 for 100% Gaussian peak shape), the parameter s is the one-half of FWHM and E_0 is the central position of the peak.

The C 1s peaks in all 64 spectra of the samples of series A, B, C, D have been fitted. The fitting conditions are shown in table 3.5. The parameters appearing in the table are terms of eqn. 3.2 and they are described below this equation. $M = 0.3$

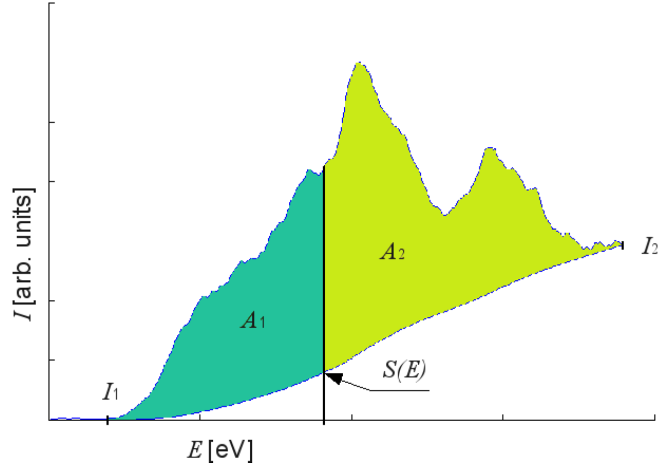

Figure 3.15: Shirley background $S(E)$ counted by the above procedure from the valence band of DLC.

	Starting points				Lower bounds				Upper bounds			
	M [-]	h[arb.u]	s [eV]	E_0 [eV]	M [-]	h[arb.u]	s [eV]	E_0 [eV]	M [-]	h[arb.u]	s [eV]	E_0 [eV]
sp2	0.3	0.5	0.5	284.3	0.3	0.0	0.4	284.2	0.3	1.0	0.6	284.4
sp3	0.3	0.5	0.5	285.1	0.3	0.0	0.6	285.0	0.3	1.0	0.9	285.2
CO2	0.3	0.2	0.5	286.0	0.3	0.0	0.0	285.5	0.3	1.0	1.8	287.0

Table 3.5: Constrains for fitting C 1s peaks: h height of the peak, M Gauss/Lorentz mixing ratio (1 for 100% Lorentzian and 0 for 100% Gaussian peak shape), parameter s is the one-half of FWHM and E_0 is a position of the peak.

(Gauss/Lorentz mixing ratio — 1 for 100% Lorentzian and 0 for 100% Gaussian peak shape) was chosen because the resolution of the analyzer is 0.36 eV. Thus the largest contribution to the shape of the carbon peak is the Gaussian one. The parameter s (1/2 of FWHM) is higher for the sp^3 peak than for sp^2. The carbon C 1s core level peak of HOPG (Highly Oriented Pyrolytic Graphite) which is used as a standard for pure sp^2 hybridization is narrower than the carbon 1s peak of diamond (pure sp^3 hybridization). The separation in position of the carbon C 1s peaks of graphite and diamond is 0.6–0.9 eV. These values were used for the separation of sp^2 and sp^3 peaks during the fitting procedure. In the case of a-DLC:H the different kind of C-H bonds are present. This type of bonding causes shifting the C 1s peak. There is a difference between the binding energy of the σ bond which includes two sp^3 hybridised orbitals of two carbon atoms $\sigma = A(sp^3_{C_1} + sp^3_{C_2})$ and the energy of bond including one carbon atom and one hydrogen atom $\sigma = B(sp^3_C + 1s_H)$. This difference in bonding causes differences in density, internal stress and mechanical properties as hardness and elastic modulus etc.

The results are presented in Appendix, table 5.1 and two examples of fitting the spectral peaks are shown in fig. 3.16.

In figure 3.17 the development of the relative concentration of the sp^3 bonds with the relative hydrogen flow $H_2/(CH_4{+}H_2)$ is shown. The solid line connects the medians of sp^3 of each series. The sp^3 concentration does not show any statistically significant evolution with the bias voltage U_b, pressure p or RF power P.

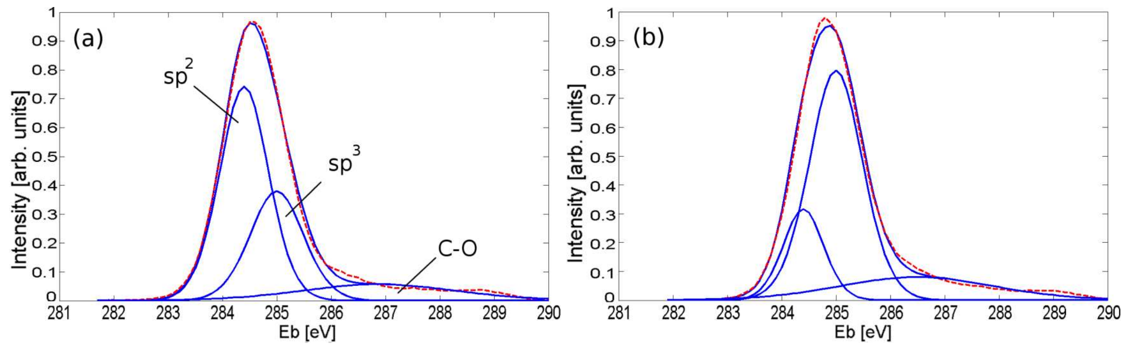

Figure 3.16: Fitting of the C 1s peak with three components as sp^2, sp^3 and C-O. In figure (a) and (b), there is the C 1s peak of a sample with a lower and a higher sp^3 hybridization, respectively.

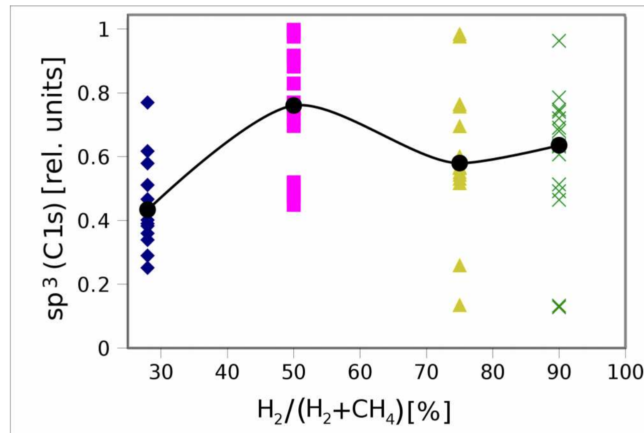

Figure 3.17: The degree of sp^3 hybridization against the relative hydrogen flow $H_2/(CH_4+H_2)$.

In figure 3.18, the relative concentration of the sp^3 bonds against the bias voltage for different $H_2/(CH_4+H_2)$ flows is shown. There is no visible trend neither inside the individual series nor across the series.

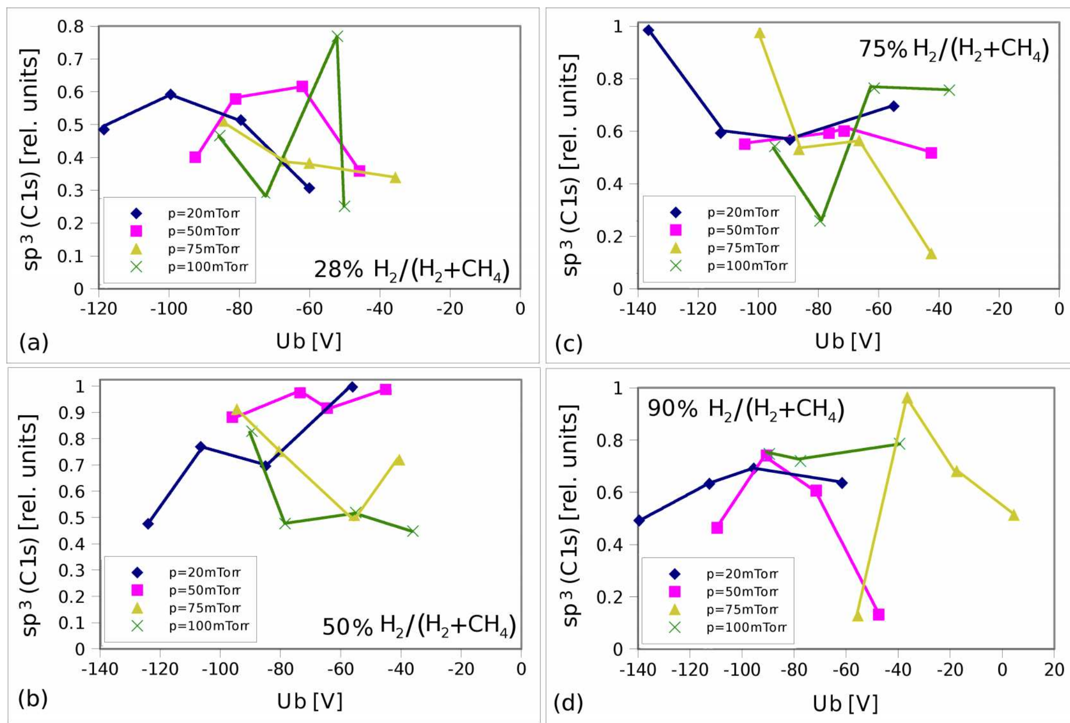

Figure 3.18: The degree of sp^3 hybridization against the bias voltage U_b for different relative hydrogen flows $H_2/(CH_4+H_2)$, (a) series A, (b) series B, (c) series C, (d) series D.

3.3.2. Auger C K-V-V spectra and sp^3 content

For the measurements of Auger C K-V-V (K shell - Valence - Valence) peaks and the valence band, the samples without deposited gold were used, since gold in the spectra interfered with other peaks in the area of interest. The spectra of four samples of each series (16 together) were acquired. The acronyms of measured samples are X11, X14, X41, X44, where X means the symbols A,B,C and D. The conditions during data acquisition were as follows: constant pass energy PE=20 eV, energy step 0.3 eV, dwell time 0.05 s and 50 scans.

Determination of the quantity of spatially bonded carbon from Auger K-V-V peaks is possible to deduce via the derivative of this curve [36]. The difference between the maximum and the minimum of the derivative (D value) varies for diamond and graphite. The spectra of diamond and HOPG (Highly Oriented Pyrolytic Graphite) were used as standards with 100 % of sp^3 (diamond has only σ bonds) and 100 % of sp^2 (the last third electron in the p orbital can form the π bond with another electron in the p orbital of a second carbon atom) hybridization, respectively. It is worth noting, that the sp^2 hybridised orbitals make a stronger and shorter σ bond in the graphite layer than is the σ bond in diamond. On the other hand graphite has a weak π Wan der Waals bond between this strongly bonded layers. Hence, graphite is soft. D values of graphite and diamond were taken from [37]. Here it is mentioned $D = 14.3$ eV for diamond and $D = 22.5$ eV for graphite. It is necessary to differentiate the spectra. Since differentiation is unfortunately a good generator of random numbers (especially such curves with the high ratio of noise/signal), it is important to smooth these spectra before differentiation and consequently to smooth their derivatives to determine the D values. And this makes another problem: What the level of smoothing to use? Here is necessary to make a compromise among smoothing of the resulting curve and preserving the original curve keeping all significant features. In figure 3.19, it is seen how the D value varies with changing the smoothing level of Auger C K-V-V spectra and changing of the smoothing level of Auger C K-V-V derivative. In this study a Savitzky-Golay filter was used [38].

Preferably, we should use the values close to the left bottom corner (low level of smoothing). In this figure designed from a measured Auger spectrum, it is clearly seen that it is possible to choose an area with a higher or a lower D value related to the content of sp^3 hybridizations. If the D value changes about 0.5 eV, the sp^3 content will change around 6 %. An interesting thing is, that the graph is symmetrical.

In the end, for obtaining D values, 19 smoothing points of all Auger curves and derivatives were used. Each point in the original spectrum is recounted from its neighbouring values given by the smoothing points. In figure 3.20, original Auger spectra with smoothing lines and appropriate derivatives with smoothing are mentioned. The points show a maximum and a minimum of the smoothed derivative. Difference between these points is equal to the D value.

In figure 3.21, the sp^3 content determined from Augere C K-V-V spectra as a function of the relative hydrogen flow $H_2/(CH_4+H_2)$ is shown.

In fig. 3.22, the comparison of sp^3 content derived from C 1s and Auger C K-V-V peaks is presented. The sp^3 contents derived from Auger C K-V-V peaks are overestimated with comparison by those derived from the C 1s peaks.

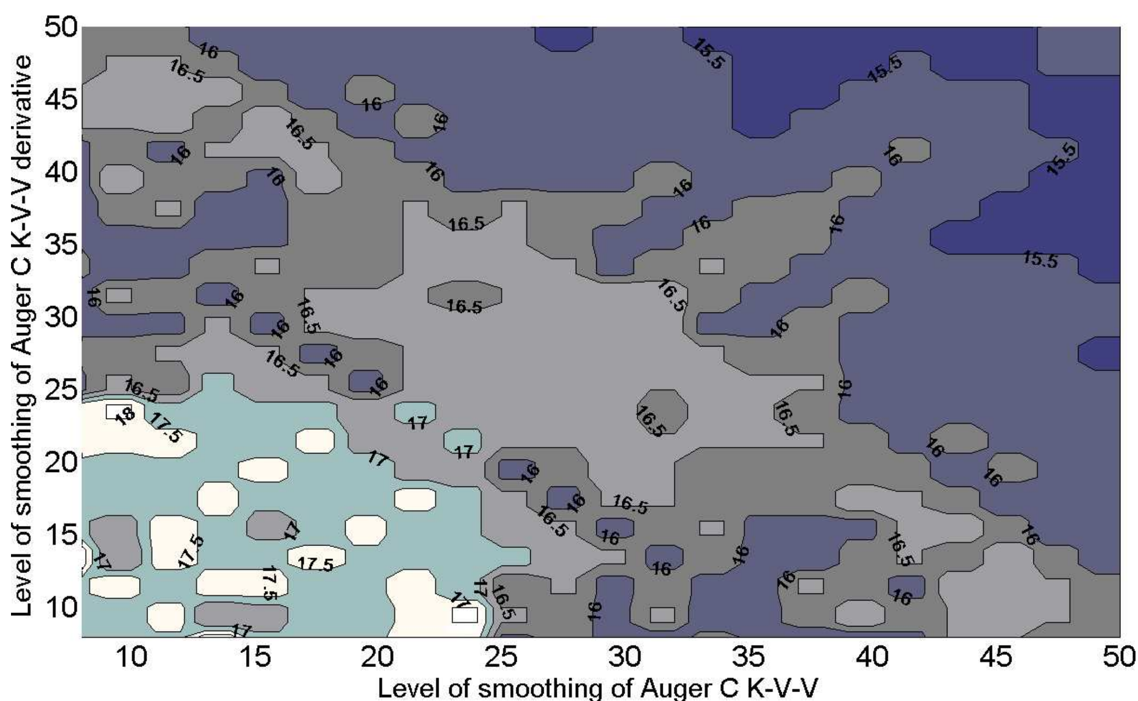

Figure 3.19: The level of smoothing of Auger C K-V-V against the level of smoothing of Auger derivative $\mathrm{d}A/\mathrm{d}Eb$ and the corresponding D values (sample $A11$). A change of D values with the quality of smoothing is obvious, which consequently causes the change of the sp^3 fraction.

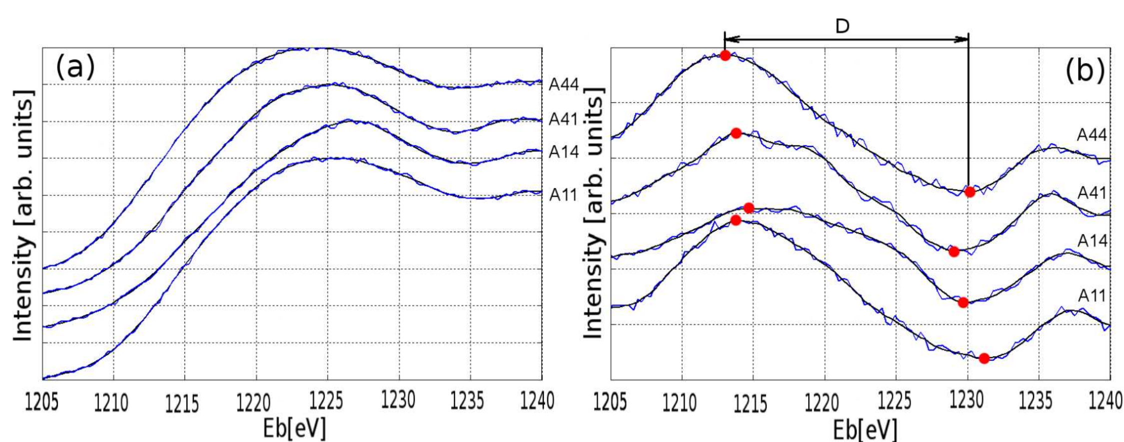

Figure 3.20: Auger C K-V-V spectra (a) and corresponding derivatives (b), series A. The points in (b) show a maximum and a minimum of the smoothed derivative. The difference between these points is equal to the D value.

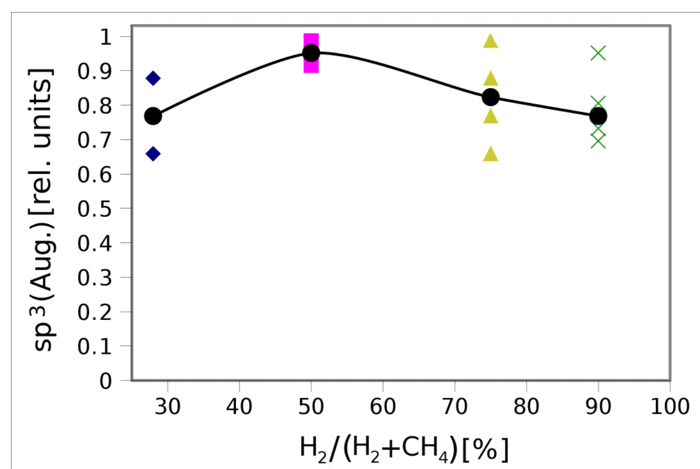

Figure 3.21: Amount of sp^3 hybridization derived from the Auger C K-V-V spectra against the relative hydrogen flow $H_2/(CH_4{+}H_2)$. The solid line connects the medians of sp^3 of each series.

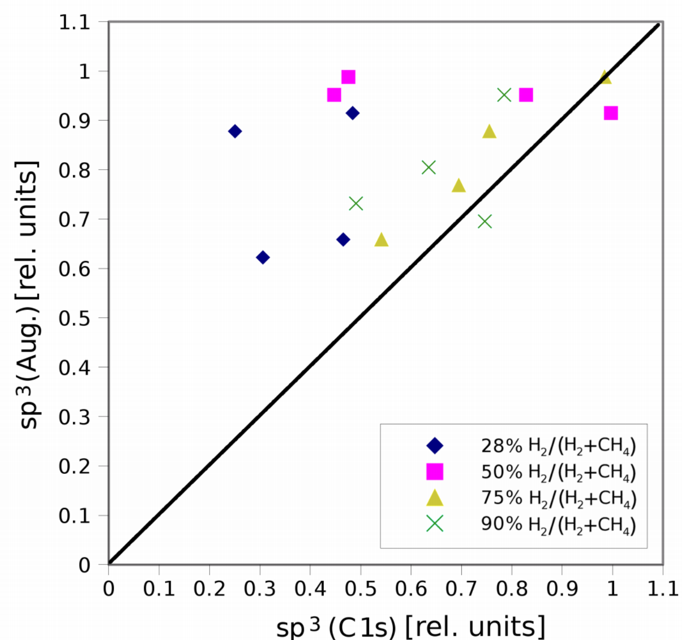

Figure 3.22: Comparison of the sp^3 hybridization determined from the Auger C K-V-V peaks with the sp^3 hybridization determined from the C 1s core level peaks. The solid line represents an ideal relationship.

3.3.3. Valence band of DLC

Electrons in the valence band are more sensitive to the environment surrounding an atom. Hybridised orbitals termed sp^3, sp^2 and sp^1 have their origin in the valence band. This terms were created to the better description of valence bands of molecules. It is well known that eigenfunctions calculated for hydrogen (only for hydrogen it is possible to find eigenfunctions and eigenvalues of the system analytically) were not sufficient for description of molecules. Hybridization enables to create different shapes of orbitals with higher electron density between atoms making bonds stronger with a deeper potential energy. This approach gives a higher agreement with an experiment. According to the molecular orbital theory, all of the valence electrons are delocalized around a molecule. Each electron lies inside a new molecular orbital with energy different from valence atomic orbitals.

A general idea about the position of the valence band can be given if we knew atomic ionization energy of carbon, hydrogen and oxide. Atomic ionization energies of the hydrogen valence electron H 1s is 13.6 eV, carbon C 2s electron 19.4 eV, C 2p electron 10.6 eV, O 2s electron 32.3 eV and O 2p electron 15.8 eV. Binding energy of these states are approximately same with opposite signs. Generally, a new bonding molecular orbital should correspond to lower energy (higher ionization energy) and nonbonding or antibonding orbitals have higher energies than original atomic orbitals.

The cross section of generation of electrons from carbon p states is 13× lower these from carbon s states [39] when using X-rays. This results in a lower intensity of XPS spectra for the p electron peaks as seen in figure 3.23. If someone wants to study the p states, it is possible to employ UVS (Ultra Violet Spectroscopy) where the cross section for electrons of p states is higher than for the s states, but this goes out the topic of this thesis.

Figure 3.23 shows the normalised XPS valence band spectra of a-DLC:H. There are two spectra, both shifted with respect to the Fermi level. The first fitting was performed according to [39]. In this study seven peaks were used (p-π, p-σ, two peaks C 2p and three C 2s). In addition, we have two oxide states O 2p and O 2s. The centers of carbon peaks were located in positions published in [39] and [40]. The oxide peaks centers were set according to [33]. The centers of all peaks could be changed during fitting in defined ranges.

The fitting results of all fifteen spectra were taken and the average values of all fitting parameters were counted. These new values (positions, FWHM) were used as an input to a new fitting procedure with a lower possibility of moving. Two resulting spectra and all values are shown if figure 3.23 and in Appendix, table 5.2, respectively. From there, it is obvious that the deposition with higher $H_2/(CH_4+H_2)$ flow inside the chamber has a broader central area around C 2s states. We have summed the areas below the three C 2s peaks. In figure 3.24 the results are shown.

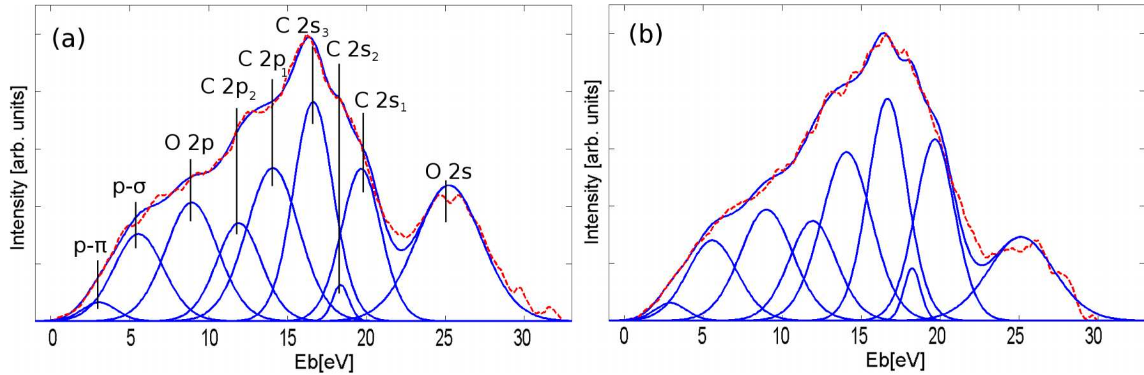

Figure 3.23: Fitting the valence band of DLC:H with nine peaks. (a) sample A44 with 25 % of H and (b) sample D44 with 29 % of H. The amounts of hydrogen in the structure were determined from the Raman spectroscopy.

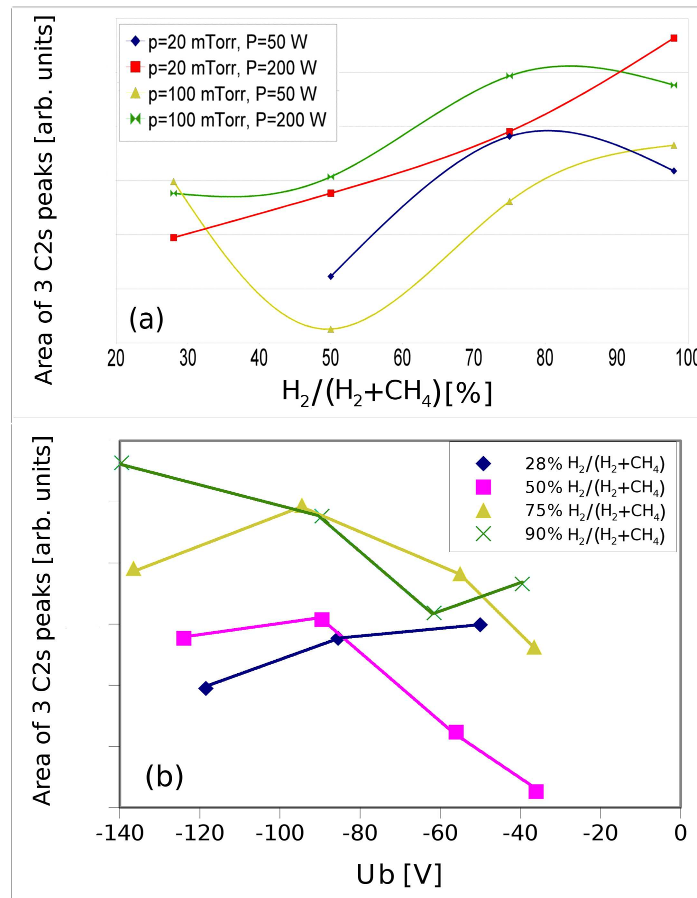

Figure 3.24: The sum of the areas below three $2s$ peaks C $2s_1$, C $2s_2$ and C $2s_3$ as the function of the relative hydrogen flow $H_2/(CH_4+H_2)$ (a) and of the bias voltage U_b (b).

3.4. Raman spectroscopy

The measurement of Raman spectra were performed by the *Renishaw inVia* spectrometer at Masaryk University in Brno. A laser beam with an excitation wave length of 514 nm (green colour), power 20 mW was used. A technique, employed in this study is called the *micro-Raman* spectroscopy. In this particular case the laser is focused on a sample by an objective providing 50× magnification and a spot size of 2 μm at the surface. The Stokes-Raman spectrum of one measured DLC sample is shown in figure 3.25. The spectrum contains several features. A sharp peak at the position 525 cm^{-1} corresponds to phonon of silicon near to the Γ point of a Brillouin zone. A small broader peak at a position 872 cm^{-1} is the second-resonance frequency of silicon. The dominant features of the spectra are two broad peaks at the positions close to 1330 cm^{-1} and 1530 cm^{-1}. These peaks are called D and G ones, respectively. The label G has its origin in the name of graphite and D means "disordered".

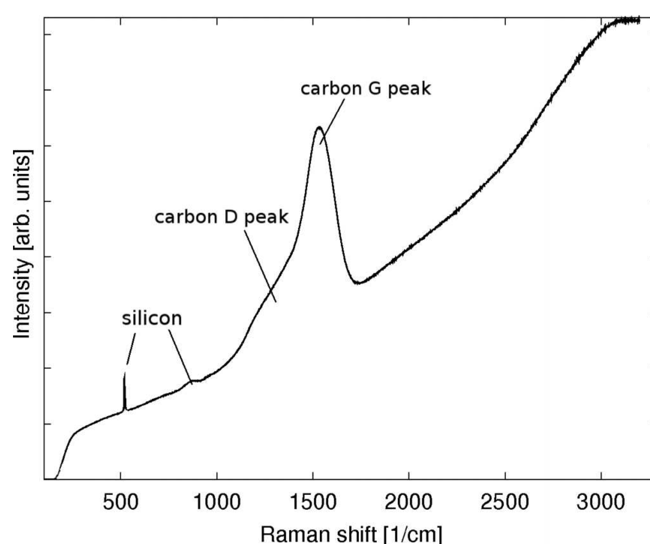

Figure 3.25: Raman spectrum of one samples with a significant luminescence background.

In figure 3.26, the Raman spectrum of the EA11 sample showing the D and G peak is present. The Shirley background similarly to C 1*s* and a valence band peaks in XPS spectra was used for removing a luminescence background and a similar procedure of fitting as in case of XPS spectra was used to obtain the parameters of the D and G peak components. The results of these fittings are in table 3.6.

3.4.1. Structural information

The cross section of the sp^2 bond for a visible Raman spectroscopy (514 nm) is 50–250× higher than for the sp^3 one [41]. There several rules on the evolution of Raman spectra of D and G peaks are discussed. Figure 3.27 shows amorphization trajectory of carbon from pure graphite having 100 % sp^2 to nearly 100 % sp^3 hybridization [41]. It consists of 3 stages.

Name	E_D	E_G	FWHM$_D$	FWHM$_G$	h_D	h_G	I_D	I_G	I_D/I_G	m/h_G
	[eV]				[arb. units]				[-]	[µm]
EA11	1345	1538	326	172	0.33	0.86	121	171	0.71	2.58
EA14	1351	1539	332	173	0.35	0.84	132	168	0.79	1.50
EA41	1334	1531	328	164	0.34	0.86	126	161	0.78	3.16
EA44	1348	1538	333	173	0.34	0.85	129	169	0.76	1.66
ED11	1347	1538	331	163	0.38	0.84	140	158	0.88	3.41
ED14	1375	1552	338	145	0.45	0.8	172	133	1.29	2.64
ED41	1341	1534	327	167	0.35	0.85	129	164	0.79	3.47
ED44	1359	1543	333	153	0.41	0.82	155	146	1.06	2.80

Table 3.6: Results of fitting Raman spectra in energy range from $1000\,\mathrm{cm}^{-1}$ to $1800\,\mathrm{cm}^{-1}$. E_D and E_G are peak positions, FWHM$_D$ and FWHM$_G$ full width of the peaks at half maximum, h_D and h_G are normalised peak heights, I_D and I_G are peak areas (intensity), m/h_G is the ratio of the slope of luminescence between the energies $1000\,\mathrm{cm}^{-1}$– $1800\,\mathrm{cm}^{-1}$ to the intensity of the G peak which indicates the amount of hydrogen in the structure.

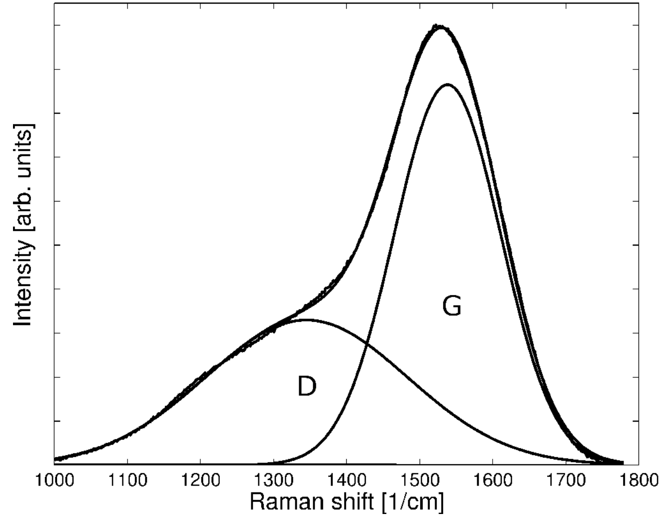

Figure 3.26: Fitting of the Raman spectrum by two single pure Gaussian peaks D and G (sample EA11).

Stage 1:

- A pure graphite layer has an infinite grain size L_a and thus no grain boundary. When the grain size decreases the G peak moves up in position due to phonon confinement in graphite domains.
- The D peak increases its intensity according to the relation $I_D/I_G \approx 1/L_a$.

Stage 2:

- At the moment when the structural disorderlines appears in graphite, the layer is characterised by weaker bonds and lower phonon frequency. The G peak moves towards lower wavenumbers (frequencies). The relation $I_D/I_G \approx 1/L_a$ from the stage 1 is not valid any more and the square of the grain size L_a^2 and number of aromatic rings is proportional to $\approx I_D/I_G$.

Stage 3:

- Changing from planar to a spatial structure ($sp^2 \rightarrow sp^3$) and the change from aromatic rings to shorter olefinic chains. The G peak position is higher due to the confinement of π electrons in this chains. The ratio of I_D/I_G is close to zero due to missing aromatic rings.

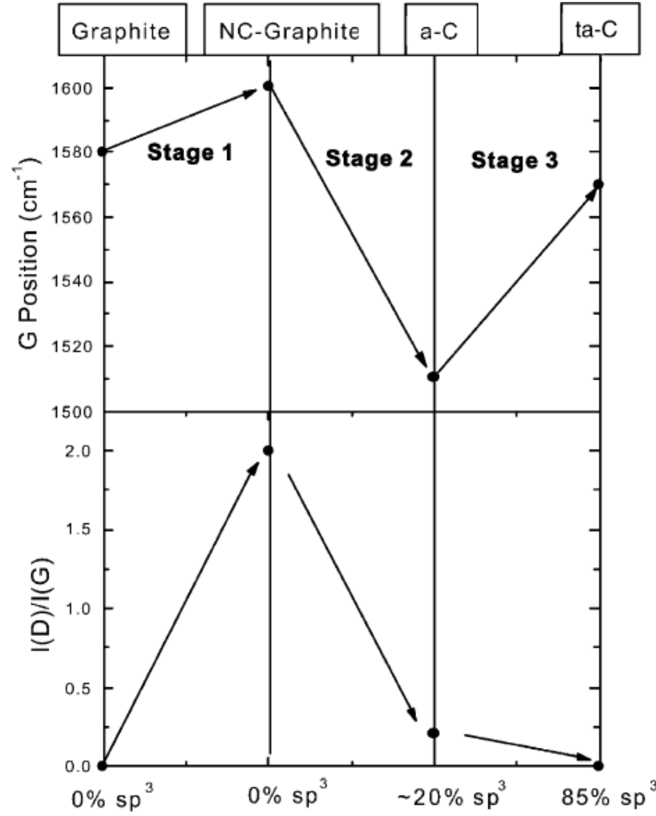

Figure 3.27: Amorphization *trajectory* of carbon [41].

3.4.2. Hydrogen content

The amount of hydrogen in the structure can be deduce according to [42]. In this publication, many depositions of DLC:H by RF-PECVD and ECWR (Electron Cyclotron Wave Resonance) systems were carried out. They considered two precursor gases as CH_4 and C_2H_2, the silicon was used as a substrate. Raman spectra showed up no photoluminescence background (PB) for low hydrogen concentrations, whilst for the maximum ones (50%) H the PB was strong. PB was characterised as the ratio between the slope m (measured between $1000\,\text{cm}^{-1}$ and $1800\,\text{cm}^{-1}$) and the height of the G peak. The hydrogen content was determined from NRA (Nuclear Reaction Analysis). By fitting these results they got a formula (eqn. 3.3) allowing the assessment of hydrogen content in DLC:H. The results are listed in table 3.6.

$$\text{H[at\%]} = 21.7 + \log \frac{m}{h_G} [\mu\text{m}] \tag{3.3}$$

3.4.3. Results

Hydrogen content in the film is higher for depositions at higher $H_2/(CH_4+H_2)$ and lower for higher absolute values of bias voltage U_b (fig. 3.28). Both, the position of the G peak and I_D/I_G increase with absolute value of the bias rather for higher $H_2/(CH_4+H_2)$ and hold constant for lower $H_2/(CH_4+H_2)$. This can be caused by a decrease of hydrogen in the structure at lower $H_2/(CH_4+H_2)$. Compare fig. 3.27, our results correspond to the stage 2 of the amorphization trajectory.

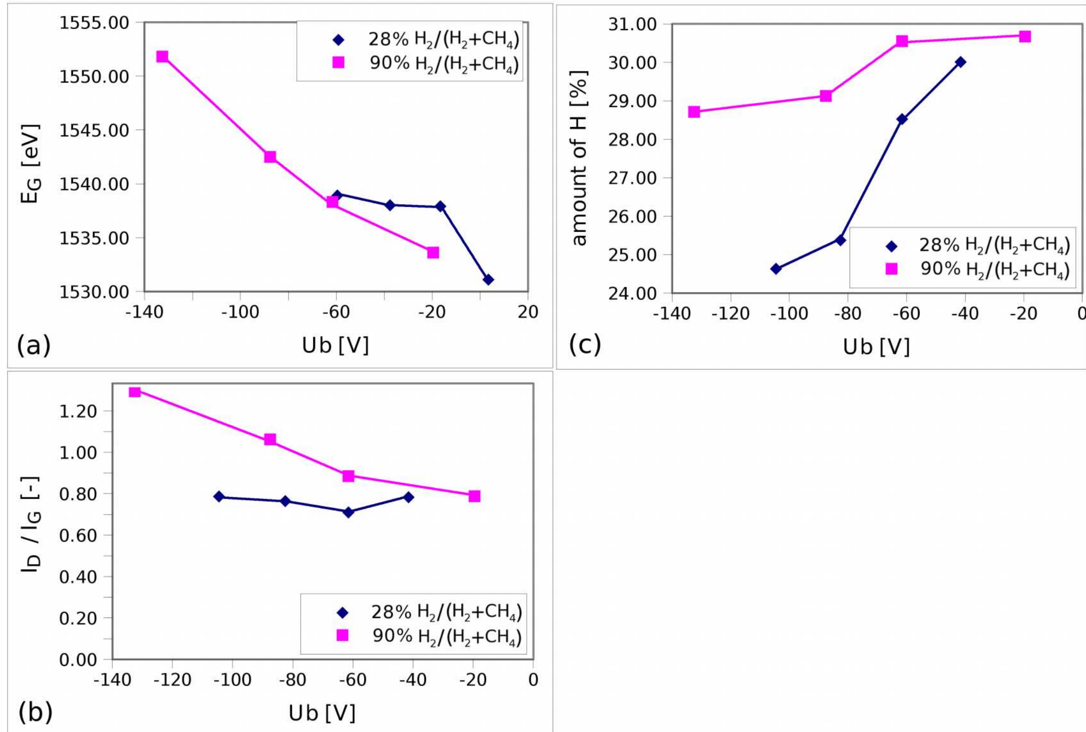

Figure 3.28: Position of the G peak E_G (a), ratio of I_D/I_G intensities against the bias voltage U_b (b) and the amount of hydrogen in the DLC:H film (c).

3.5. Spectroscopic reflectivity

Spectroscopic reflectivity measurements were done by a thin film reflectometry setup *Ocean optics NANOCALC-2000-UV-VIS*. The system uses the relative method of determination of reflectance $\Re$. Reflectance $\Re$ is determined by comparison of the intensity of the light I_s reflected by a sample with the intensity of the light I_0 reflected by a standard sample which reflectance $\Re_0$ is known [28]. As the standard sample crystalline silicon was used. In the reflectance mode, the ratio of reflected intensities $\frac{I_s}{I_0}$ in eqn. 3.4 is measured. The obtained spectrum must by multiplied by reflectance of silicon $\Re_0$ according to equation 3.4. Such a procedure is shown in fig. 3.29. Here (a) represents the relative spectrum $\frac{I_s}{I_0}$, (b) the reflectance of Si and (c) the absolute reflectance of the sample.

$$\Re = \Re_0 \frac{I_s}{I_0} \tag{3.4}$$

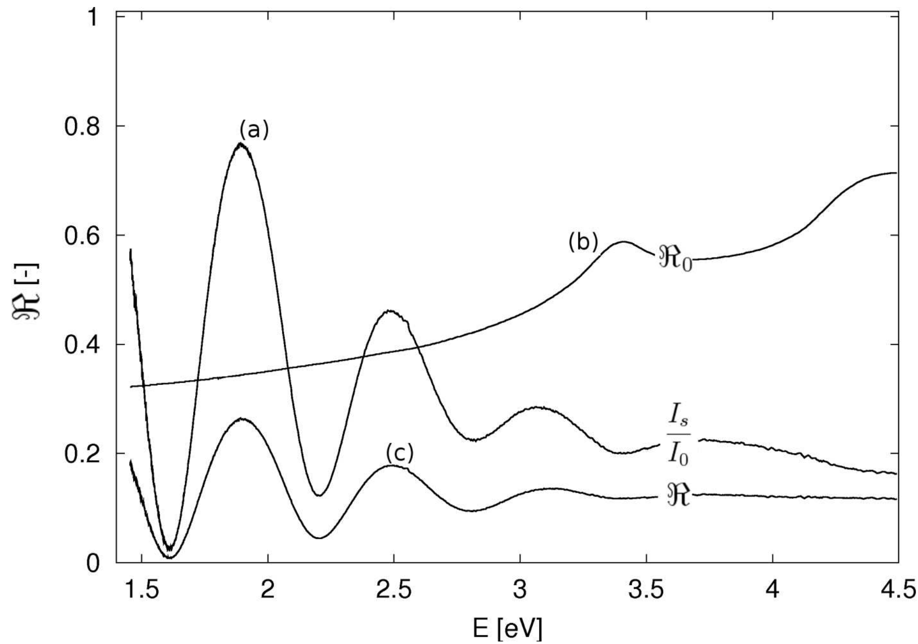

Figure 3.29: Calculation of the absolute reflectance $\Re$ of a sample from the relative one $\frac{I_s}{I_0}$. The curve (a) represents a relative spectrum $\frac{I_s}{I_0}$ taken to the reflectance of silicon $\Re_0$ (b), absolute reflectance $\Re$ of a sample is marked as (c).

Two computer programs were written in order to obtain optical parameters of DLC films according to [27] and [25, 26]. They were created in the *GNU Octave* language (high-level programming language which is freely redistributable under the terms of the GNU General Public License (GPL)). The main procedure of both software is a fitting function based on Levenberg-Marquardt nonlinear regression.

The input parameters are the same for both programs (relative reflectance spectrum $\frac{I_s}{I_0}$ and Si energy reflectance $\Re_0$). The programs deal with parameters given in [27] or [25, 26] to be found by fitting. At the beginning of each fitting procedure, where an experimental curve is fitted by a theoretic one (being described by one or more parameters), we have to give the first estimates of parameters. Here the difficulties can

arised, because if the theoretical function has many parameters, the fitting procedure can find a local and not an absolute minimum. Particularly, to reduce this problem, starting values as close to the expected values as possible should by chosen. Theory given in [25] deals with five parameters A ,B, C, E_g, $n(\infty)$ and in [27] with six parameters Q_σ, Q_π, $E_{h\sigma}$, $E_{g\sigma}$, $E_{h\pi}$, $E_{g\pi}$. In our case, we have an additional parameter – thickness h of the DLC layer.

3.5.1. Program based on PJDOS (Parameterising Joint Density of States) model

The program is based on the theory proposed by Franta *et al.* [27]. As mentioned above, this theory deals with seven (including thickness) parameters needed to fit an experimental reflectance curve by a theoretical curve and thus to assess the index of refraction n and extinction coefficient k of the DLC layer.

Testing of the code

Debugging and testing of a new software code is an important part of its development. This was done using the data published in [27]. The experimental reflectance of one sample was taken [27] and compared to the spectrum calculated by the code with the parameters taken from [27]. The points lie on the theoretical curve (fig. 3.30) and so the code can be considered as the correct one.

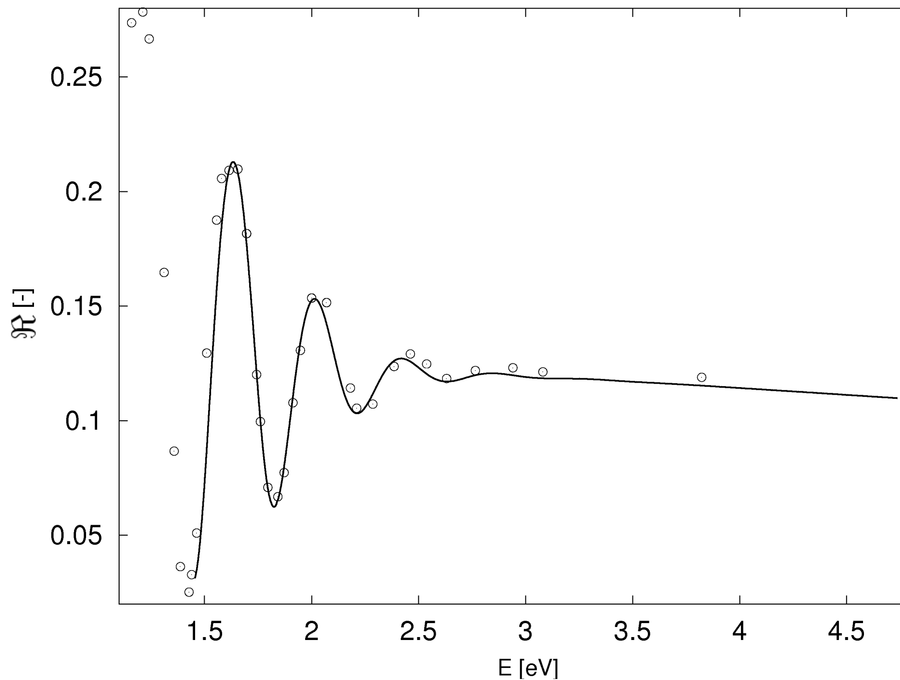

Figure 3.30: Testing the code by the comparison of reflectance of the sample H05 (circuits) published in [27] with the reflectance calculated by the code (smooth curve) using the parameters given in [27] for this sample. If all procedures in the code are correct, the points must lie on the curve.

Fitting

The first attempt has been done without any constrains. The thickness was set to the value obtained from profilometry and other values of parameters Q_σ, Q_π, $E_{h\sigma}$, $E_{g\sigma}$, $E_{h\pi}$, $E_{g\pi}$ were chosen for the DLC films approximately according to [27]. Although the resulting fits were well-imitated the experimental curve, some of found values of parameters were out of exception. Most of the sixteen results of different spectra fitted by this way showed this behaviour.

The second attempt utilised the knowledge on a shape of the valence band (XPS measurement). $E_{h\sigma}$, the distance between the bottom of a σ bonding and the top of a σ^* nonbonding band (see.2.10) was set to 65 eV and this value was kept constant. In this way, the number of unknown parameters was decreased.

3.5.2. Program based on Forouhi-Bloomer (FB) model

This theory deals with six parameters (including thickness). During fitting, no larger deviation of parameters were observed for different spectra. The starting values of A ,B, C, E_g, $n(\infty)$ were chosen close to those published for a-C:H in [26]. As in the previous case, the thicknesses were set to the values obtained from profilometry.

3.5.3. Results

The results obtained from reflectance measurements are presented in Appendix, table 5.3 and most important are shown in figure 3.31. The first column of figure 3.31 contains results from the (PJDOS) model [27]. The graph in (a) shows the evolution of $E_{g\sigma}$ and $E_{g\pi}$ energies with the bias voltage U_b, (b) $E_{h\pi}$ energy, (c) and (d) index of refraction n and extinction coefficient k, respectively at a wavelength of λ =600 nm. In the second column, there is energy of the band gap E_g (e) according to the (FB) model [25], the correlation of index of refraction n(600 nm) (f) and extinction coefficient k(600 nm) (g), respectively, determined from (PJDOS) and (FB) models. It is evident that these coefficients are the same for both (PJDOS) and (FB) theories. The graph (h) shows the change of $E_{g\pi}$ and $E_{g\sigma}$ energies with pressure p. Comparison of index of refraction n and extinction coefficient k counted by (PJDOS) and (FB) theories of one sample is seen in figure 3.32.

Also the correlation of the thicknesses determined by profilometry and reflectance measurements was studied (fig. 3.33). Although the thicknesses measured by the profilometer might be slightly overestimated, there is a good agreement between these results.

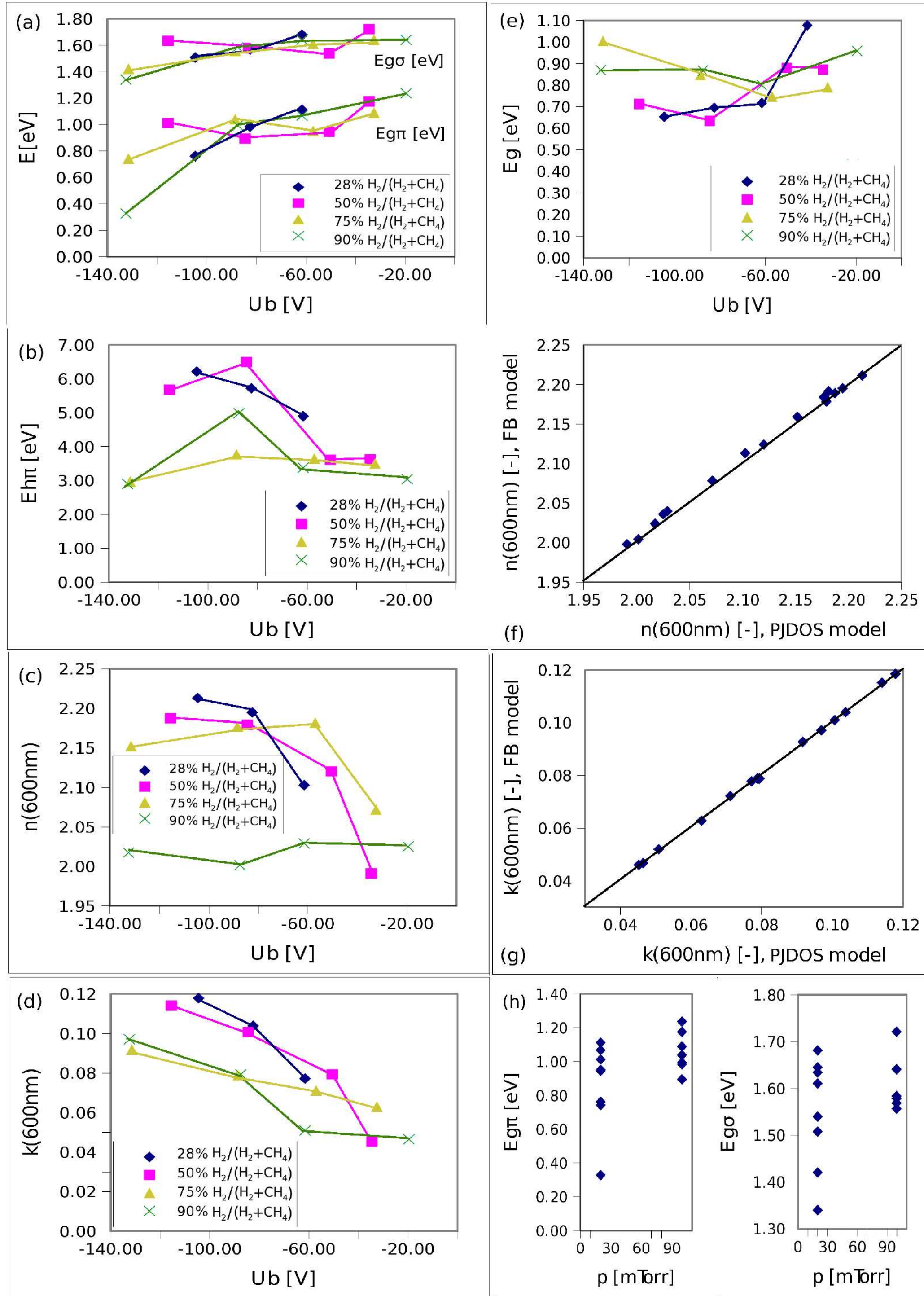

Figure 3.31: Correlation of results obtained from reflectance measurements, (a) shows $E_{g\sigma}$ and $E_{g\pi}$ as a function of the bias voltage U_{b}, (b) $E_{h\pi}$, (c) and (d) index of refraction n and extinction coefficient k, respectively at a wavelength of $\lambda = 600$ nm according to the PJDOS model. Energy of the band gap E_g (e) according to the FB model, the correlation of index of refraction $n(600\,\mathrm{nm})$ (f) and extinction coefficient $k(600\,\mathrm{nm})$ (g) determined from PJDOS and FB models. The solid lines in (f) and (g) represent the ideal relationship. The graph (h) shows the change of $E_{g\pi}$ and $E_{g\sigma}$ energies with pressure p.

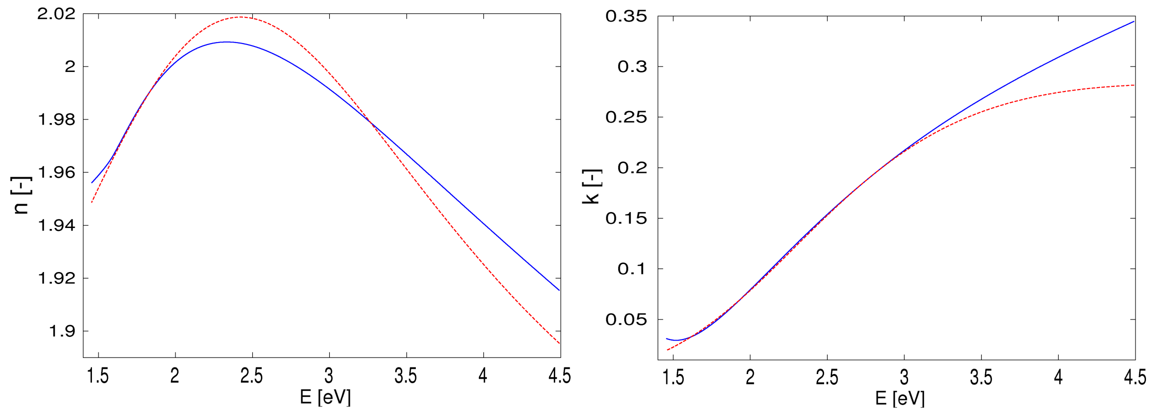

Figure 3.32: Index of refraction n and extinction coefficient k of the sample ED44 for the PJDOS (solid lines) and FB (dashed lines) theories. The differences between these two fits are more profound at higher energies.

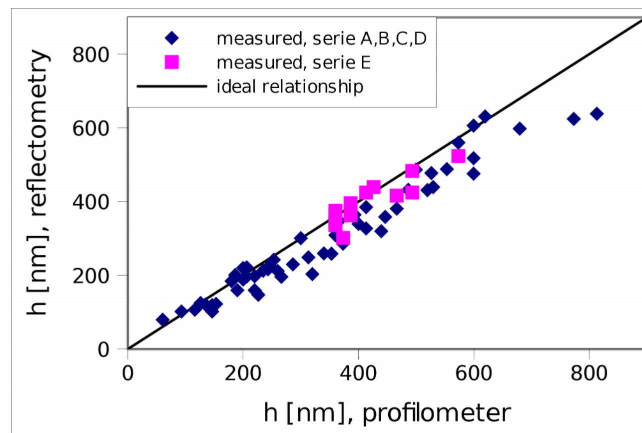

Figure 3.33: Correlation between the thickness of DLC films obtained by profilometry and optical reflectivity measurements.

3.6. First principle calculations of vibrational spectra and ground states of DLC in *Abinit*

At present, a few programs deal with first principles calculations. One of them is the *Abinit*. Abinit is a set of procedures allowing optimising the geometry of the system consisting from nuclei and electrons according to the DFT (Density Functional Theory). More details about this program can be found on the official web site [43]. The main procedure in the program performs DFT calculations by using the plane wave basis and pseudopotentials.

3.6.1. Preparation of an initial structure for the ground state calculations

Generally, the ground state calculation is the first step on the way to calculate the electronic structure of a molecule. Here, several parameters relating to the physical properties of the material such as mass density, number of different elements, interatomic distance and so on are needed. Many other parameters describing the procedures allowing the system to reach the relaxed configuration by molecular dynamic procedures must by set up. However, if someone wants to corelate experimental results with calculations, an input model of the structure of an interest must by as close to the real structure as possible. The molecular dynamics is only used for correcting this geometrical structure to reach the minimal energy of the system and thus get closer to the real structure.

The program based on a random number generator was written to create the first estimation of the structure of DLC:H. The input parameters of this program are:

- cell size
- number of atoms in the cell N
- minimal interatomic distance

The main program function is define N atom positions in the cell so that atoms fulfil the cell and have interatomic distances higher than a minimal one. In the case of DLC and DLC:H the cubic shape of cell was chosen. The number of atoms is 60 and minimal interatomic distance 1.5 Å. Sixty atoms in the cell is a compromise with respect to the time necessary to reach the relaxed geometry and determination of the structure. The size of the cell 7.5 Å was calculated to get the mass density between 1.5 g/cm^3 and 2.5 g/cm^3 for 30 %, 20 %, 10 % and 0 % of hydrogen in the structure.

If we took the geometry generated by the random generator only, we would obtain positions of atoms close to each other and consequently the relaxation would not be successful. The repulsive interatomic force is high and leads to high velocities of atoms. This results in much lower time integrated steps during the relaxation and thus to a increase of overall relaxation times. A value of 1.5 Å inter-atomic distance was observed as a good estimation for minimisation of these forces. This is shown in figure 3.34.

3.6.2. Convergence study

A convergence was studied with respect to kinetic-energy cutoff E_{cut}. E_{cut} is an internal parameter in the *Abinit* which determines the number of planewaves at a given k point

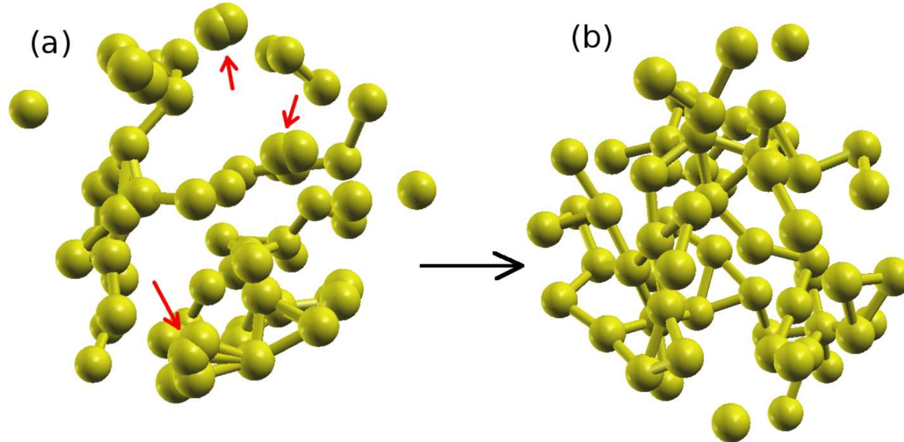

Figure 3.34: Sixty randomly generated atom positions (a), this structure is not suitable for a molecular dynamic relaxation due to the short-distance atoms. Rearrangement after a structural optimisation (b). The arrows in (a) show the closest atoms which would do the problems in consequent relaxation in *Abinit*. The structure in (b) is ready for relaxation in *Abinit*.

in the Brillouin zone. This parameter has a significant effect on the calculation quality. The higher value implies a better convergence of the calculations and always a lower total energy of the system. A disadvantage of this choice is that the higher value also increases the overall time of calculations. The structural convergence was studied with respect to E_{cut}=25, 30 Ha (1 Ha (hartree)=27.2113845 eV). The molecular dynamic algorithm used in *Abinit* is based on Verlet algorithm [44] and stopping each atom for which the scalar product of velocity and force is negative. This dynamics depends on a time step determining the time range of updating the ions positions. This is another convergence parameter the influence of which must by studied. In the convergence test 100 of carbon atoms was used. The time step was studied in the range of 25–100 atomic time units (1 atu = $2.418884 \cdot 10^{-17}$ s). The value of 100 atu leads in this case to the total break up of the structure and thus to the divergence of E_{tot}. The value of 25 atu is fine and allows the structural relaxation. The result can be seen in fig. 3.35. There are two curves — a solid line for E_{cut}=25 Ha and dashed line for E_{cut}=30 Ha. On the horizontal axis there is an iteration number which corresponds to the time step. On the vertical axes there is the total energy of a system E_{tot}. This value is not an overall system energy and thus has no physical meaning. Only the difference in energies has a physical sense. If these curves are close enough, the next increase in cutoff energy E_{cut} is useless.

3.6.3. Computation of a relaxed structure of DLC having a different hydrogen content

The relaxation computation of different DLC:H structures were performed for 0%, 10%, 20%, 30% hydrogen content. Two structures for the same hydrogen content were created to show, how the properties are influenced by the relaxation procedure. At first, the number of sixty atom was chosen to obtain a satisfactory ratio of *physical meaning/computation time*. According to the mass density of DLC and DLC:H structures between 1.5 g/cm^3 and 2.5 g/cm^3, the size of 7.5 Å of the cell was chosen. Using the pro-

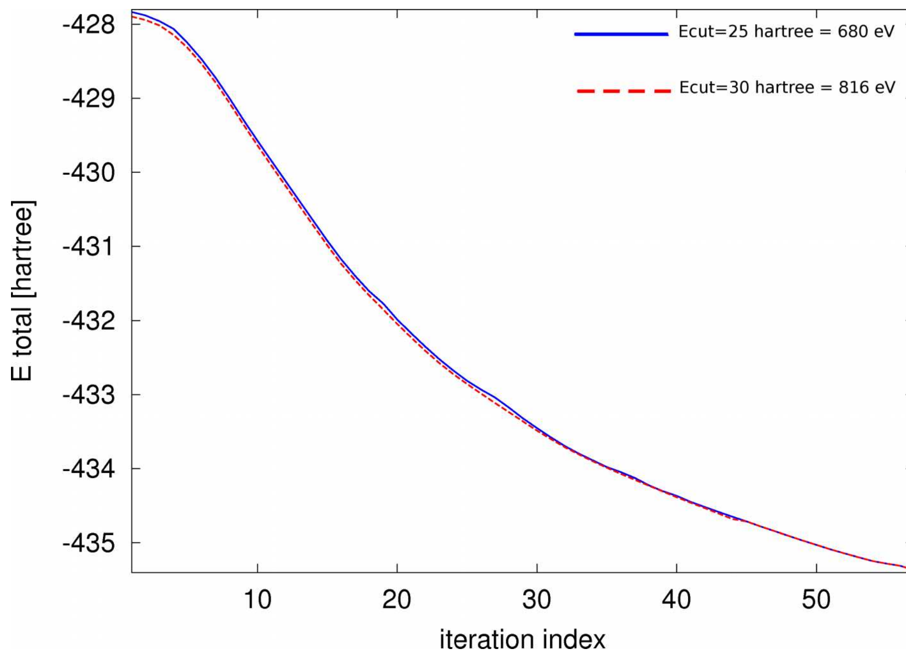

Figure 3.35: Convergence test with respect to the kinetic cutoff E_{cut} energy . There are two curves, a solid line for E_{cut}=25 Ha and a dashed line for E_{cut}=30 Ha. In the horizontal axis there is an iteration number corresponding to a time step and in the vertical axes, the total energy of the system E_{tot}.

gram mentioned above the initial structure was created (see fig. 3.34). This structure was incorporated to the *Abinit* code for the structural relaxation with cutoff energy of E_{cut}=30 Ha and a time step of 25 atu. The evolution of total energy with the iteration number during the relaxation of the structure with 60 C and 0 H → (0% H), 40 C and 20 H → (30% H) can be seen in fig. 3.36. Solid and dashed lines represent the same structure (mass density, %H) but different displacements of atoms in the cell. The relaxation procedure was stopped between 400–500 steps when in a consequential step the total energy changed only in the fifth significant digit.

In figure 3.37, the relaxed structures are visualised. Here a cell with a base consisted of 60 carbon atoms (a) and of (40 C and 20 H) atoms (b) is depicted. At the bottom of the figure, the repetitions of these primitive cells are shown.

3.6.4. Calculation of electronic DOS (Density of States)

Each carbon and hydrogen atom has four and one valence electrons, respectively. If we had 10 carbons atoms separately to each other we would have 20 valence orbitals (10 2s and 10 2p). If these carbon atoms are put together, the number of 20 orbitals must stay. New molecular orbitals are different in energies with respect to the atomic orbitals. After a structural relaxation, when the system approached an area close to the minimum of the total energy, a procedure to get these energies (eigenvalues of a Hamiltonian) can be used in the *Abinit* code. We can get the discrete values of energies the number of which depends on the number of atoms in the cell. The computation of eigenvalues is performed at a zero temperature. *Abinit* allows to use smearing techniques to get the electronic DOS from these values. However, this function was not used and

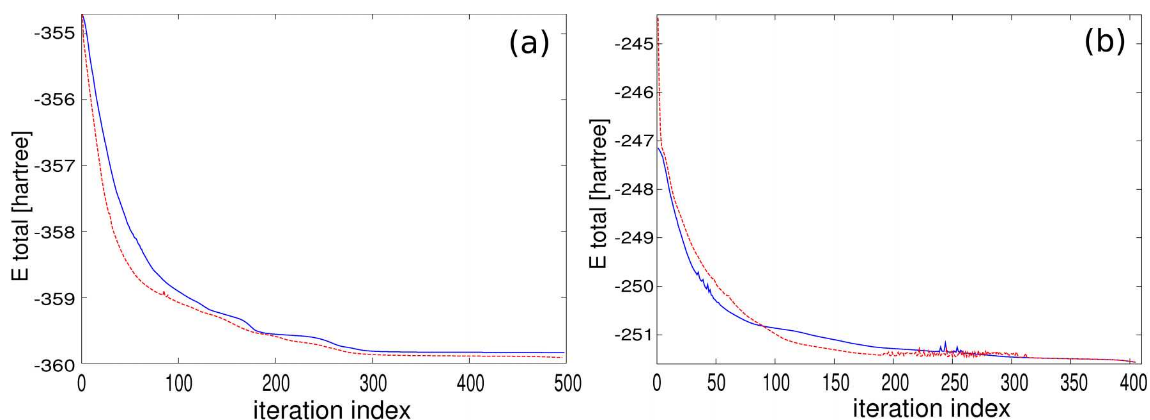

Figure 3.36: Evolution of total energy with the iteration number during the relaxation of a structure (a) with 60 C and 0 H → (0% H) and (b) 40 C and 20 H → 30% H. Solid and dashed lines represent the same structure (mass density, %H) but different displacements of atoms in the cell.

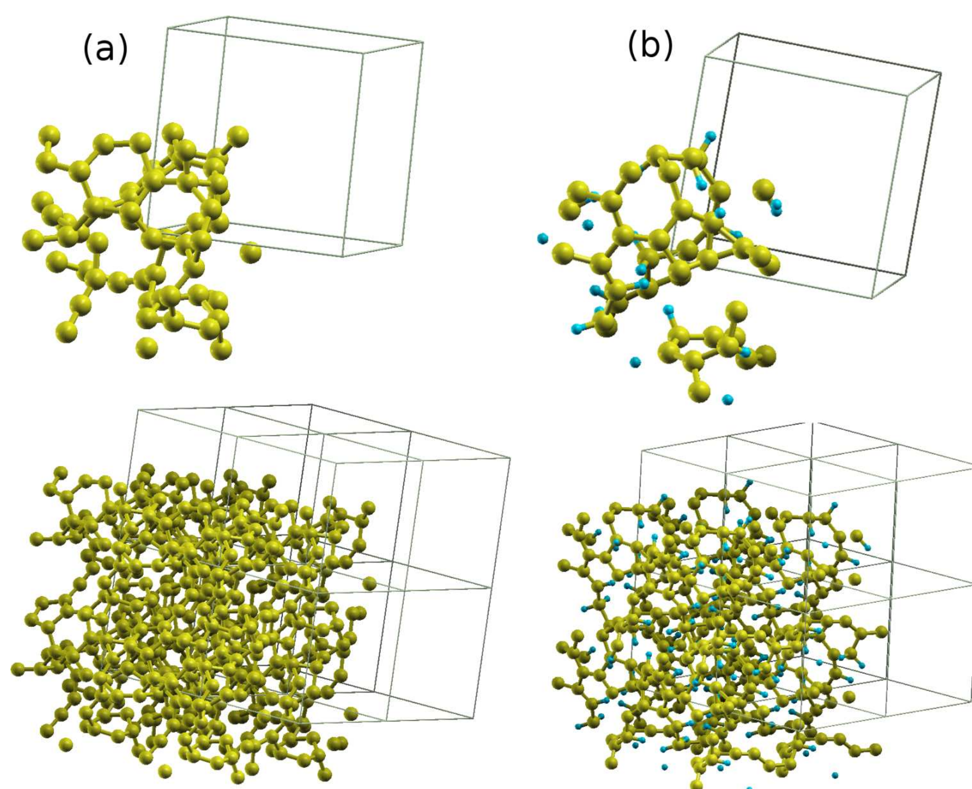

Figure 3.37: Relaxed structure of DLC (a) and DLC:H with 30 % H (b). Larger and smaller atoms represent carbon and hydrogen, respectively. At the bottom, the repetitions of these cells (supercells) are shown.

the conversion of eigenvalues to DOS was performed by a similar technique in *MatLab*. Electronic DOS of DLC and DLC:H with 0 %, 10 %, 20 % and 30 % of hydrogen content

are shown in figure 3.38. In each row, the DOS of two structures with the same amount of hydrogen but of different atom distribution are placed.

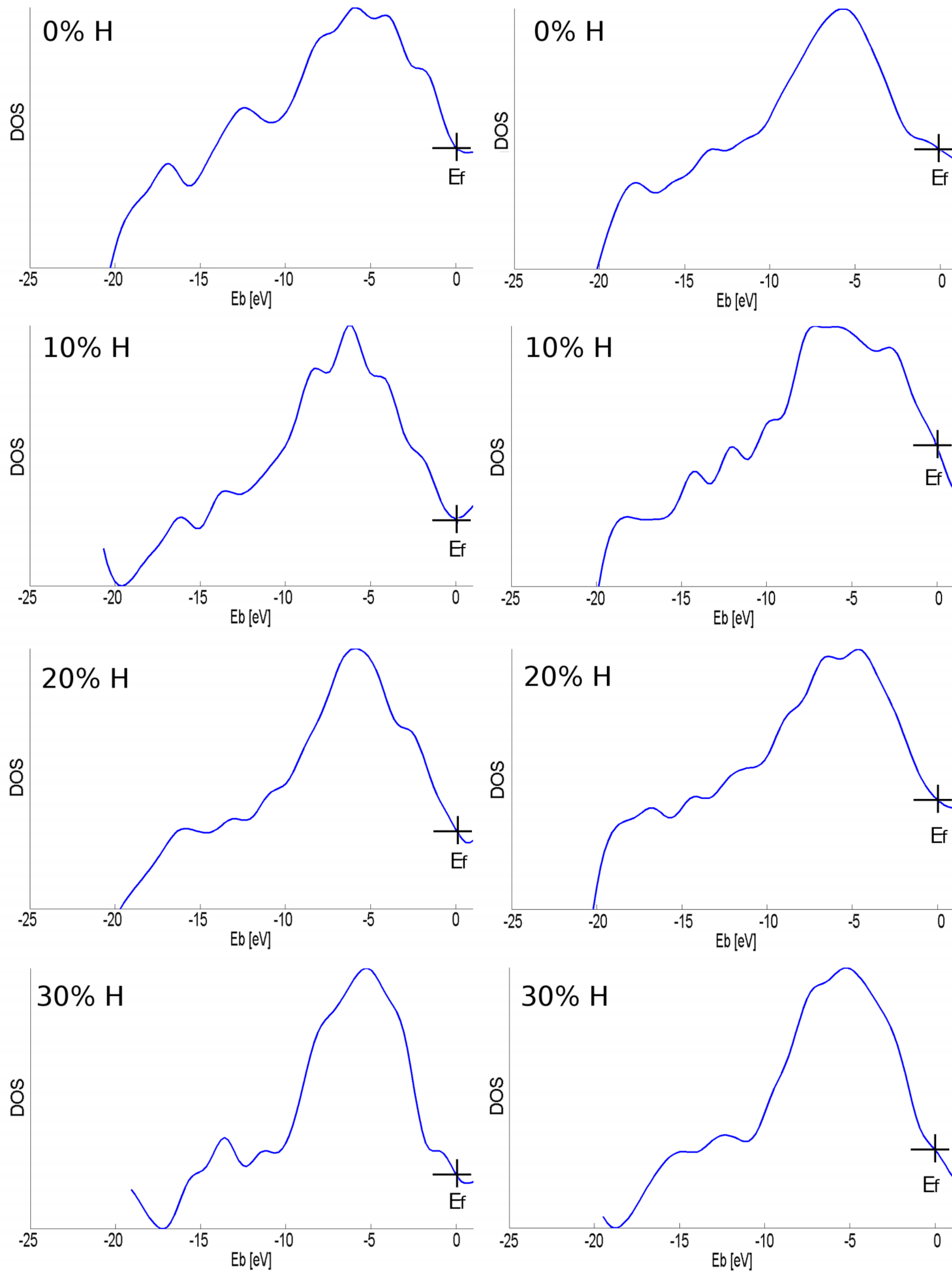

Figure 3.38: DOS of DLC and DLC:H for different amount of hydrogen in the structure. Each row contains the DOS for the structures with the same amount of hydrogen, but with a different atom distribution in the cell.

The comparison of the electronic DOS of DLC:H computed by *Abinit* and published in [39] is made in figure 3.39). The picture (a) represents the measured valence band without an oxide peaks O 2s and O 2p contribution. The features appearing in the

measured valence band are associated through solid lines with the features in the DOS calculated by *Abinit* (b) and published DOS (c) in [39] as well. It can be seen that the overlap of the valence band (a) and DOS (c) is very good. Actually, this paper was the one of two articles being used for the interpretation of the valence band. The DOS calculated by the *Abinit* is slightly shifted towards lower energies with comparison to the published DOS.

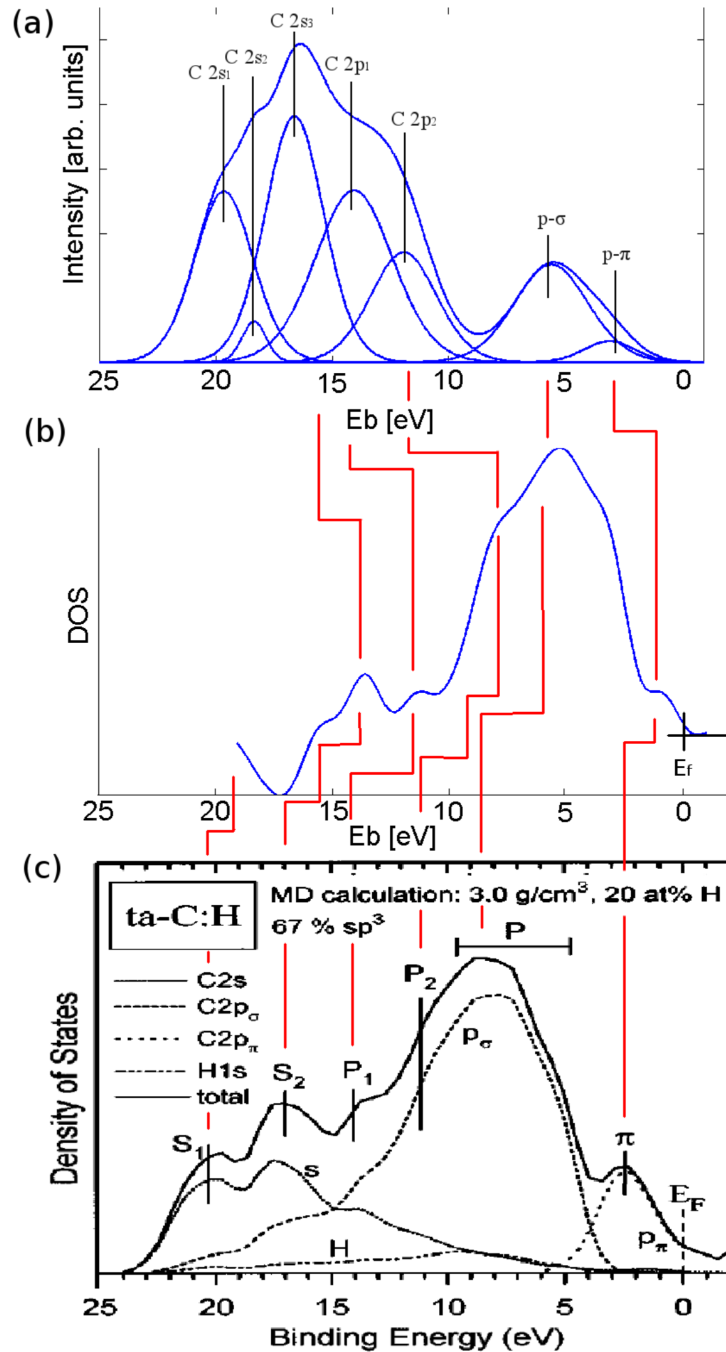

Figure 3.39: The picture (a) represents the measured valence band without an oxide peaks O 2s and O 2p contribution . DOS calculated by the *Abinit* (b) is slightly shifted towards lower binding energies with respect to the published one (c).

3.6.5. Calculation of VDOS (Vibrational Density of States)

This part deals with Vibrational Density of States VDOS of DLC. The reason why the attention was paid to VDOS is, that this directly correlates with Raman spectra. The testing of the procedure was done for crystalline silicon and diamond. The calculated phonon spectra in different parts of the Brillouin zone for silicon and diamond are in fig. 3.40.

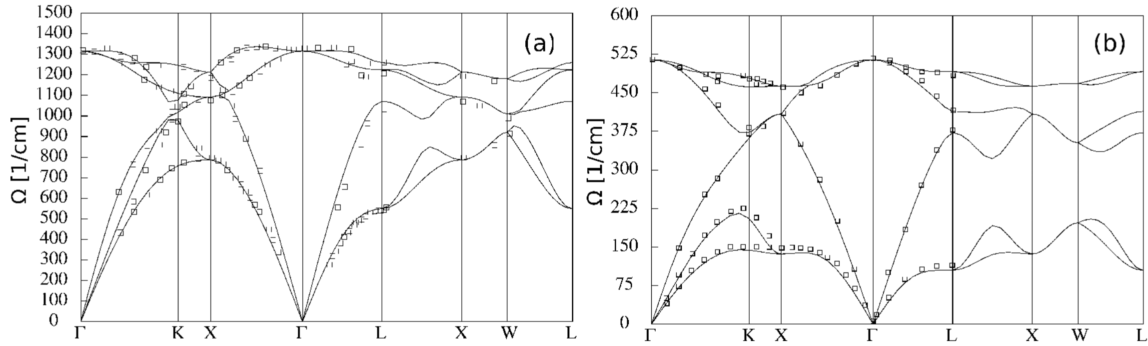

Figure 3.40: Phonon band structure of diamond (a) and silicon (b) calculated by the *Abinit*. The points represent experimental values taken from [45].

We can see a good correlation between the experimental and calculated values. In addition, the phonon frequency of silicon 510 cm^{-1} and diamond 1315 cm^{-1} in the middle of the Brillouin zone (Γ point) practically correspond to the position of the first order peak in the Raman spectra (see fig. 2.8 and 3.25). A similar procedure was used to calculate the phonon frequencies of DLC and DLC:H at the Γ point in the Brillouin zone. This computation is very time-consuming. Each atom in the cell must by displaced from the equilibrium position and energy of the final system must by calculated. The difference between the ground-state energy and energy with the displaced atom determines the oscillation frequency of the atom in the direction of displacement. If this procedure is done for three directions perpendicular to each other, one can describe atomic oscillations in an arbitrary direction of a space. This was done for the cell with sixty atoms and different amount of hydrogen. These structures are exactly the same as in the case of electronic DOS computation. In the end we obtain $3 \times N$ frequencies, where N is the number of atoms in the cell. For sixty atoms, we have 180 frequencies. The normalised vibrational density of states is possible to determine by using a histogram. The results of VDOS of DLC for different amounts of hydrogen in the structure are shown in figure 3.41. A typical feature which is not presented in the case of DLC (0 % H) and laying around 2700 cm^{-1} in DLC:H is a C-H stretch bond.

A figure 3.42 shows comparison between VDOS of DLC:H in the Γ point of the Brillouin zone obtained by *Abinit* (a) and that one published in [46]. Additionally, the measured Raman spectrum is shown below for comparison. The corresponding features are assigned by lines.

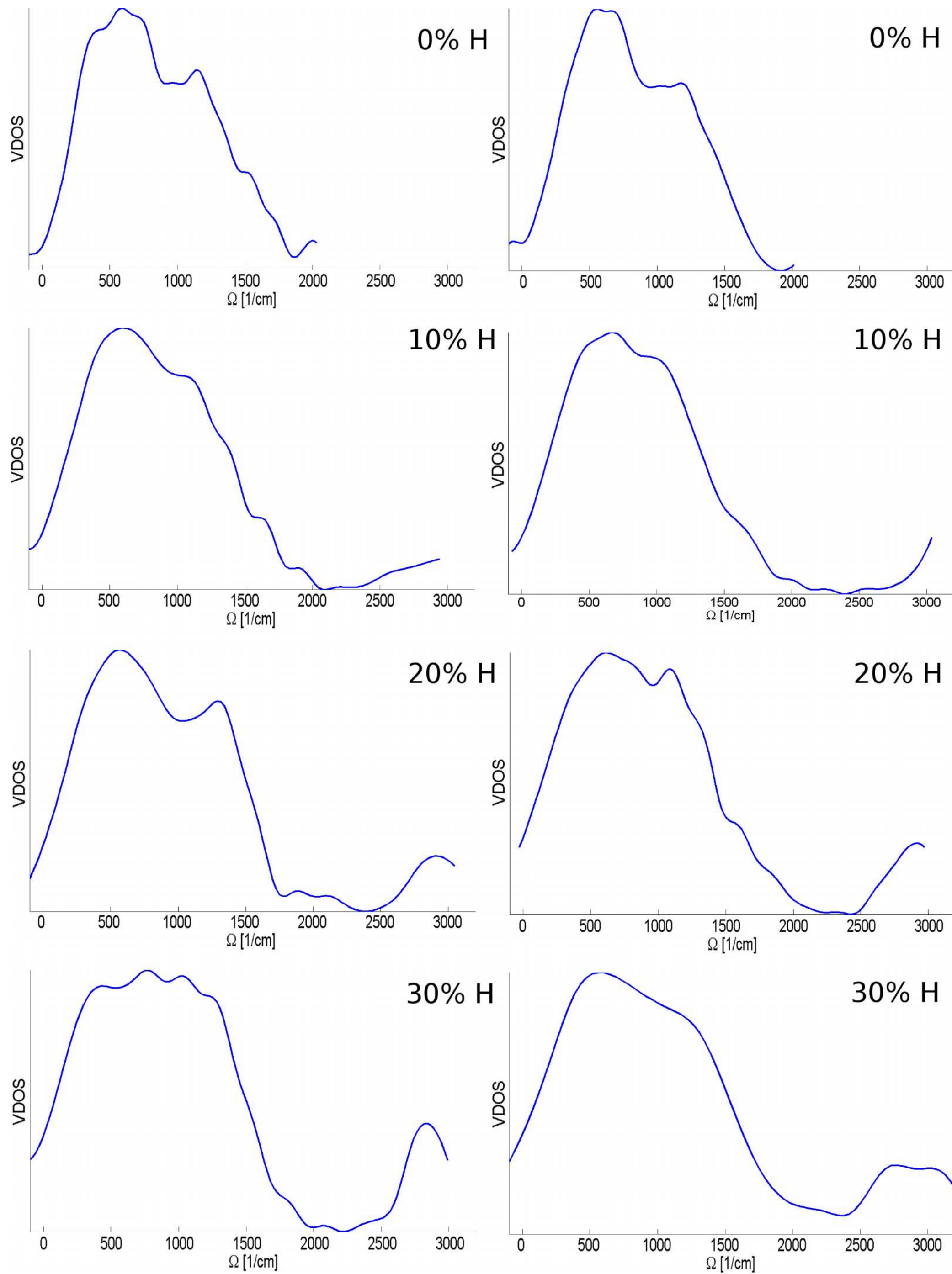

Figure 3.41: VDOS of DLC and DLC:H with different amount of hydrogen in the structure. Each row contains the VDOS for the structures with the same amount of hydrogen but with a different structural ordering of atoms in the cell.

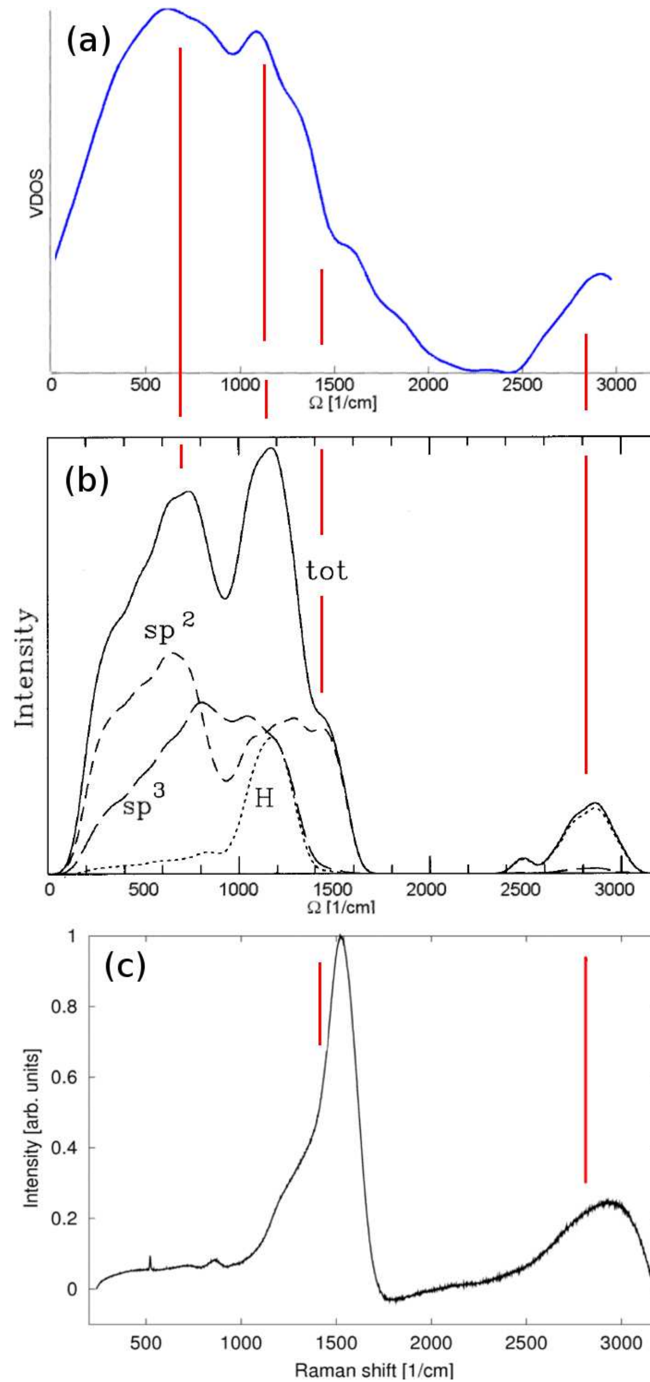

Figure 3.42: (a) VDOS of DLC:H with 20 % of hydrogen calculated by *Abinit* in the middle of the Brillouin zone (Γ point), (b) VDOS (solid line) of DLC:H with 16 % of H content, the VDOS is decomposed into the components of the sp^2 (dashed) and sp^3 (long dashed) C atoms, and H atoms (dotted) [46], (c) Raman spectrum (sample EA11) of DLC:H with subtracted luminescence background.

4. Conclusion

The aim of this project was to study DLC. Capacitively coupled RF-PECVD has been employed to prepare DLC:H films on a crystalline silicon substrate covered by native silicon oxide. Four series of deposition experiments with different relative hydrogen flows $H_2/(CH_4+H_2)$ were carried out. Each of these series consisted of sixteen depositions done under different operational parameters. These parameters were:

- deposition pressure p=(20–100) mTorr
- input RF power P=(50–200) W
- flow of hydrogen ϕ_H=(5.6–18) SCCM, flow of methane ϕ_M=(2–14.4) SCCM, total flow fixed to $\phi_H + \phi_M = 20$ SCCM

During deposition, the potential on the cathode U_1, its amplitude $U_{1\mathrm{A}}$ and plasma potential U_p were measured. The plasma potential corresponded to the values calculated from theory. The potential on the cathode U_1 was measured for twice, at the beginning and at the end of the deposition. Every time the potential at the end of deposition came closer to zero. The possible reason may be the sooting of a metal probe. Therefore, the chamber was always cleaned by iso-propanol before every new deposition. Deposition rate increases with higher pressure p or input RF power P and decreases with the relative hydrogen flow $H_2/(CH_4+H_2)$. The maximal deposition rate occurs in the range of the bias voltage U_b= (-80 – -100) V. The lowest and highest deposition rate for 18% $H_2/(CH_4+H_2)$ was 4 nm/s and 27 nm/s, respectively. On the other hand for 98% $H_2/(CH_4+H_2)$ it was only 2 nm/s and 10 nm/s, respectively. Substrate temperature at first 30 minutes did not reach 60°C. It was important, because desorption of hydrogen from surface occurs around 300°C.

The thickness of one from three samples was measured by a profilometer immediately after deposition. The same sample was stuck to after that a sample holder by an adhesive glue and the hardness and scratch tests were performed (the scratch test only for four samples from each series). During the hardness test the penetration depth should be archived up to 1/10 of film thickness to avoid a substrate influence. During a machine calibration and testing on fused silica it was found that hardness and reduced modulus were changing with penetration depth. Thus the penetration depth during the hardness test was fixed to 15 nm to avoid this contribution. Unfortunately, no development with bias voltage, hydrogen/methane mixture or pressure have been seen in hardness tests. Therefore, four depositions from each series were performed again. Each sample had a thickness close to 400 nm. The hardness and scratch tests were done again. The results show, that the hardness and reduced modulus slightly increase with increasing absolute value of bias voltage U_b (except deposition of 28% $H_2/(CH_4+H_2)$ flow) and decreasing pressure p. We can say that maximum hardness occurs somewhere between (50–80) % of $H_2/(CH_4+H_2)$ flow.

It is clearly seen that the critical load Lc_3 corresponding to the failure in front of the moving probe rapidly increases with thickness. In the low range of thicknesses linearly and in the higher range more less quadraticly. Parameter Lc_3/h has been introduced with the aim to remove influence of thickness and which allows the comparison of scratch resistivity of samples with different thicknesses. This is valid only in the first approximation in a low range of thicknesses. Thus, we could use this parameter only for samples

of series E with thicknesses close to 400 nm. Lc_3/h slightly increases with the absolute value of bias voltage for the samples with higher $H_2/(CH_4+H_2)$ flow and rapidly for these with lower one. The pressure has no significant effect on the Lc_3/h. Similarly to hardness the Lc_3/h is the highest between (50–80) % of $H_2/(CH_4+H_2)$ flow. The reason may be in increasing the hardness and reduced modulus which results in lag of failure of the substrate.

A second sample from each deposition was used for XPS analysis C K-V-V and a valence band. The third sample was covered by gold via a mask and thus a gold-DLC grid was created. XPS spectra of gold and C 1*s* were measured and the carbon peak was shifted with respect to the gold $4f^{7/2}$ peak having the energy 84 eV. The program in *MatLab* was written to processes the measured data. The Shirley background and a Gauss-Lorentz function without tail mixing were used for fitting C 1*s* peaks and valence bands. The C 1*s* peaks were decomposed to the three peaks as sp^2, sp^3 and C-O. The degree of sp^3 hybridization determined from the C 1*s* peaks does not show an evolution with the bias voltage U_b. The samples with the maximal amount of sp^3 hybridization were deposited at 50% $H_2/(CH_4+H_2)$ flow.

The sp^3 content has been also estimated from Auger spectra. The D values (difference among the minimum and the maximum of the differentiated Auger spectra) were calculated. An influence of a smoothing procedure of Auger spectra A and of the derivative dA/dE_b to the D value was observed. The sp^3 content determined from the Auger spectra was higher than that one from the C 1*s* peak. The maximum of sp^3 hybridization occurred again at 50% $H_2/(CH_4+H_2)$ flow. The correlation between the sp^3 content derived from C 1*s* peaks and Auger C K-V-V peaks is weak. The possible explanation is that the results are influenced by the large amount (25 %–30 %) of hydrogen in the films structure.

An experiment with a valence band was done. At first sight, it was seen that the higher amount of hydrogen in the gas mixture causes a broadening of the central area. All the peaks were shifted with respect to the Fermi level and decomposed in nine peaks. The summation of three C 2*s* states below central area was done. This sum increases with the relative hydrogen flow $H_2/(CH_4+H_2)$ and with the absolute value of bias voltage U_b.

Only eight Raman spectra were measured using a visible-Raman spectroscopy (514 nm). It is possible to estimate the amount of hydrogen in the structure of the DLC:H from the luminescence background. The structural information can be possible obtained from the ratio of intensities I_D/I_G and the positions of D and G peaks. The hydrogen content in the structure is higher for depositions with higher $H_2/(CH_4+H_2)$ flow and higher for lower the absolute value of bias voltage U_b. Both the position of the G peak E_G and the ratio I_D/I_G increase with the absolute value of bias voltage U_b rather with higher $H_2/(CH_4+H_2)$ flow and hold constant at lower $H_2/(CH_4+H_2)$ flow. This can be influenced by a higher decrease of hydrogen in the structure with lower $H_2/(CH_4+H_2)$ flow. Referred to fig. 3.27, our results correspond to trajectories in stage 2. Unfortunately, the stage 2 is between nano-crystalline graphite and with 20 % of sp^3 which does not correlate to the results obtained from XPS measurements, where the sp^3 content was rather higher than 20 %.

The reflectance spectra of all samples were measured. Two programs were written to fit these spectra using two different approaches to get the index of refraction n and extinction coefficient k satisfying the Kramers-Kronig relation. In addition, the

parameters appearing in these theories are related to the electronic structure of the DLC including the band gap E_{g}. One program was successfully tested using the aid of the published data. The agreement between index of refraction n and extinction coefficient k obtained by these two theories is quiet good for lower energies (up to 3 eV) and poor for higher energies. The obtained thicknesses were correlated with profilometric measurements. The energy of band gap $E_{g\sigma}$ of $\sigma \rightarrow \sigma^*$ and $E_{g\pi}$ of $\pi \rightarrow \pi^*$ transitions decreases with a higher absolute value of bias voltage U_{b} (PJDOS model). It does not corresponds to the energy band gap E_g evolution obtained for 75% $H_2/(CH_4+H_2)$ flow from the (FB) model, where the energy of the band gap increases with the absolute value of bias voltage. Index of refraction n and extinction coefficient k increase with the absolute value of bias for all $H_2/(CH_4+H_2)$ flows except one (n for 90% $H_2/(CH_4+H_2)$ flow is constant with the bias voltage). None of the coefficients appearing in the PJDOS and the FB model except energy $E_{g\pi}$ and $E_{g\sigma}$ depends on pressure p. These two values are higher at the higher pressure p.

Attention has been paid to the first principle computation of electronic density of states (DOS) and vibrational density of states (VDOS) of DLC and DLC:H at Γ point. The initial model structures of DLC and DLC:H were prepared using a program which was written in the *GNU Octave* — high level programing language. By molecular dynamics in the first-principle simulation software *Abinit*, this initial structure could be relaxed to the ground state and then the electronic eigenvalues were obtained. The electronic DOS was compared with valence bands measured by XPS and published in literature. The published DOS was in a better agreement with the features in the valence band of the DLC:H. The DOS calculated by *Abinit* is shifted towards lower binding energies with respect to those published.

The VDOS of DLC and DLC:H were obtained from 3×60 frequencies. Each of sixty atoms in the cell was displaced from the equilibrium position to the three mutually perpendicular directions. From the energy difference between ground state energy and energy of the state with the displaced atom, the frequency of vibrations can be determined. The VDOS counted by *Abinit* in the Γ point is in a good agreement with the published data. Furthermore, peaks appearing in the Raman spectra can be assigned to the features in this VDOS.

Bibliography

[1] J.B. Wang, G.W. Yang: *Phase transformation between diamond and graphite in preparation of diamonds by pulsed-laser induced liquid-solid interface reaction.* Journal of Physics: Condensed Matter, 1999, vol. 11, p. 7089–7094.

[2] C. Casiraghi, F. Piazza, A. C. Ferrari, *et. al.*: *Bonding in hydrogenated diamond-like carbon by Raman spectroscopy.* Diamond & Related Materials, 2005, vol. 14, p. 1098–1102.

[3] J. Robertson: *Diamond-like amorphous carbon.* Materials Science and Engineering R, 2002, vol. 37, p. 129–281.

[4] R. Hauert: *An overview on the tribological behavior of diamond-like carbon in technical and medical applications.* Tribology International, 2004, vol. 37, p. 991–1003.

[5] A. Shirakura, *et. al*: *Diamond-like carbon films for PET bottles and medical applications.* Thin Solid Films, 2006, vol. 494, p. 84–91.

[6] M. Umeno, S. Adhikary, *et. al*: *Diamond-like carbon thin films by microwave surface-wave plasma CVD aimed for the application of photovoltaic solar cells.* Diamond & Related Materials, 2005, vol. 14, p. 1973–1979.

[7] Y. Jun, *et. al*: *Application of diamond-like carbon films to spacer tools for electron guns of cathode ray tube (CRT).* Thin Solid Films, 2000, vol. 377, p. 233–238.

[8] R. L. DeKock, H. B. Gray: *Chemical structure and bonding.* California: The Benjamin/Cummings Publishing Company, 1980. ISBN 0805323104.

[9] S. Aisenberg, R. Chabot: *Ion-Beam Deposition of Thin Films of Diamondlike Carbon.* Journal of Applied Physics, 1971, vol. 42, p. 2953–2958.

[10] S. Zeb, M. Sadiq, A. Qayyum, *et. al.*: *Deposition of diamond-like carbon film using dense plasma focus.* Materials Chemistry and Physics, 2007, vol. 103, p. 235–240.

[11] N.A. Morrison, C. William, B. Racine, *et. al.* : *Properties of a-C:H films deposited from a methane electron cyclotron wave resonant plasma.* Current Applied Physics, 2003, vol. 3, p. 433–437.

[12] Ko-Wei Weng, S. Han, Ya-Chi Chen, Da-Yung Wang *et. al.*: *Characteristics of diamond-like carbon film deposited by filter arc deposition.* Journal of Materials Processing Technology, 2008, vol. 203, p. 117–120.

[13] N. Paik: *Characterization of diamond-like carbon (DLC) films deposited by a magnetron-sputter-type negative ion source (MSNIS).* Applied Surface Science, 2004, vol. 226, p. 412–421.

[14] G. Ma, H. Zhang, H. Wu, *et. al.*: *Preparation of diamond-like carbon by PBII-enhanced microwave ECR chemical vapor deposition.* Surface and Coatings Technology, 2007, vol. 201, p. 6623–6626.

[15] *ESCALAB 250-Operating manual*: Thermo Fisher Scientific Inc.

[16] D. Halliday, R. Resnick, J. Walker: *Fyzika.* VUT Brno: nakladatelství VUTIUM, 2000. ISBN 8021418699.

[17] K. C. Ludema: *Friction.* In Modern Tribology Handbook, B. Bhushan, ed., Florida: CRC press LLC, 2001, p. 273–300. ISBN 0849384036.

[18] K. Kato, K. Adachi: *Wear Mechanisms.* In Modern Tribology Handbook, B. Bhushan, ed., Florida: CRC press LLC, 2001, p. 273–300. ISBN 0849384036.

[19] B. Beake, *et. al.*: *Micro Materials Nano Test User Manual.* Wrexham UK: Micro Materials Ltd., 2004.

[20] S.J. Bull, E. G. Berasetegui: *An overview of the potential of quantitative coating adhesion measurement by scratch testing.* Tribology International, 2006, vol. 39, p. 99–114.

[21] Ch. Kittel: *Úvod do fyziky pevných látek.* Praha: Academia, 1985.

[22] K. Nakamoto: *Infrared and Raman Spectra of Inorganic and Coordination Compounds: Theory and aplications of inorganic chemistry.* 5th edition. USA: A Wiley, 1997. ISBN 0471163945.

[23] L. Eckertová : *Fyzika tenkých vrstev.* Praha: SNTL, 1973.

[24] H. G. Tompkins, W. A. McGahan : *Spectroscopic Ellipsometry and Reflectometry: A User's Guide.* Canada: A Wiley, 1999. ISBN 0471181722.

[25] A. R. Forouhi, I. Bloomer: *Calculation of Optical Constants n and k, in the Interband Region.* In Handbook of Optical Constants of Solids II, E.D. Palik, ed., San Diego: Academic Press, 1991, p. 151–175.

[26] S. A. Alterovitz, N. Savvides, F. W. Smitg, J. A. Woollam: *Amorphous Hydrogenated Diamondlike Carbon Films and Arc-Evaporated Carbon Films.* In Handbook of Optical Constants of Solids II, E.D. Palik, ed., San Diego: Academic Press, 1991, p. 837–847.

[27] D. Franta, V. Buršíková, D. Nečas, L. Zajíčková : *Modeling of optical constants of diamond-like carbon*, Diamond & Related Materials, 2008, vol. 17, p. 705–08.

[28] E. Schmidt, J. Humlíček, F. Lukeš, J. Musilová: *Optické vlastnosti pevných látek.* Praha: SPN, 1986.

[29] R. K. Marcus: *Operation Principles and Design Considerations for Radiofrequency Powered Glow Discharge Devices.* Journal of analytical atomic spectrometry, 1993, vol. 8, p. 935–943.

[30] B. Shi, J. L. Sullivan, B. D. Beake: *An investigation into which factors control the nanotribological behaviour of thin sputtered carbon films.* Journal of Physics D: Applied Physics, 2008, vol. 41, no. 4.

[31] S. J. Bull: *TOPICAL REVIEW: Nanoindentation of coatings.* Journal of Physics D: Applied Physics, 2005, vol. 38, no. 24

[32] J. R. Tuck, A. M. Korsunsky, S. J. Bull, R. I. Davidson: *On the application of the work-of-indentation approach to depth-sensing indentation experiments in coated systems.* Surface and Coatings Technology, 2001, vol. 137, p. 217–224

[33] G.Beamson, D. Briggs: *High Resolution XPS of Organic Polymers.* London: A Wiley, 1992. ISBN 0471935921.

[34] *Peak Fitting in XPS.* [online]. [cit. 2009-05-17]. <http://www.casaxps.com/help_manual/manual_updates/peak_fitting_in_xps.pdf >.

[35] *ADVANTAGE.* [computer program]. Ver. 3.89. Licenced by Thermo Fisher Scientific.

[36] P. Mérel, *et. al.*: *Direct evaluation of the* sp^3 *content in diamond-like-carbon films by XPS.* Applied Surface Science, 1998, vol. 136, p. 105–110.

[37] T. Zaharia: *The study of ultra-low energy depozition of hydrogenated amorphous carbon thin films.* [diploma thesis]. Birmingham UK: Aston University, School of Engineering & Applied Science, Electronics Engineering, 2007.

[38] *MATLAB Curve Fitting Toolbox 2 - User's Guide.* [online]. Published in March 2009 [cit. 2009-05-17]. <http://www.mathworks.com/access/helpdesk/help/pdf_doc/curvefit/curvefit.pdf>.

[39] J. Schafer, J. Ristein, R. Graupner, *et. al.*: *Photoemission study of amorphous carbon modifications and comparison with calculated densities of states.* Physical Review B, 1996, vol. 53, p. 7762–7774.

[40] V. Matolín, I. Matolínová, K. Veltruská, K. Mašek: *Photoelectron spectroscopy and secondary ion mass spectrometry characterization of diamond-like carbon films.* Thin solid films, 2007, vol. 515, p. 5386-5390.

[41] A. C. Ferrari: *Determination of bonding in diamond-like carbon by Raman spectroscopy.* Diamond & Related Materials, 2002, vol. 11, p. 1053–1061.

[42] C. Casiraghi, F. Piazza, A.C. Ferrari, *et. al.*: *Bonding in hydrogenated diamond-like carbon by Raman spectroscopy.* Diamond & Related Materials, 2005, vol. 14, p. 1098–1102.

[43] *Abinit.org.* [online]. [cit. 2009-05-28]. <http://www.abinit.org/> .

[44] M. C. Payne, M. P. Teter, D. C. Allan, *et. al.*: *Iterative minimization techniques for ab initio total-energy calculations: molecular dynamics and conjugate gradients.* Reviews of Modern Physics, 1992, vol. 64, p. 1045–1097.

[45] M. Aouissi, I. Hamdi, N. Meskini, A. Qteish: *Phonon spectra of diamond, Si, Ge, α-Sn: Calculation with real space interatomic force constants.* Physical Review B, 2006, vol. 74, no. 5.

[46] F. Mauri, A. D. Corso: *Vibrational properties of tetrahedral amorphous carbon from first principles.* Applied Physics Letters, 1999, vol. 75, p. 644–646.

5. Appendix

Name	sp2	sp3	C-O	sp2	sp3	C-O	sp2	sp3	C-O	sp2	sp3	C-O	sp3/(sp3+sp2)
	M1[-]	M2[-]	M3[-]	h1[arb.un.]	h2[arb.un.]	h3[arb.un.]	s1[eV]	s2[eV]	s3[eV]	$E_0$1[eV]	$E_0$2[eV]	$E_0$3[eV]	[-]
A11	0.3	0.3	0.3	0.68	0.30	0.13	0.6	0.6	1.75	284.4	285.0	285.5	0.31
A12	0.3	0.3	0.3	0.61	0.54	0.06	0.5	0.6	1.75	284.4	285.0	287.0	0.51
A13	0.3	0.3	0.3	0.52	0.62	0.06	0.5	0.6	1.75	284.4	285.0	286.9	0.59
A14	0.3	0.3	0.3	0.63	0.51	0.06	0.52	0.6	1.75	284.4	285.0	286.8	0.48
A21	0.3	0.3	0.3	0.74	0.38	0.06	0.55	0.6	1.75	284.4	285.0	286.9	0.36
A22	0.3	0.3	0.3	0.48	0.63	0.06	0.49	0.6	1.75	284.4	285.0	287.0	0.62
A23	0.3	0.3	0.3	0.52	0.61	0.07	0.51	0.6	1.75	284.4	285.0	286.9	0.58
A24	0.3	0.3	0.3	0.71	0.42	0.06	0.54	0.6	1.75	284.4	285.0	286.5	0.40
A31	0.3	0.3	0.3	0.73	0.35	0.08	0.57	0.6	1.75	284.4	285.0	286.3	0.34
A32	0.3	0.3	0.3	0.72	0.40	0.07	0.54	0.6	1.75	284.4	285.0	286.5	0.38
A33	0.3	0.3	0.3	0.71	0.41	0.06	0.55	0.6	1.75	284.4	285.0	286.4	0.39
A34	0.3	0.3	0.3	0.61	0.54	0.07	0.51	0.6	1.74	284.4	285.0	286.6	0.51
A41	0.3	0.3	0.3	0.82	0.26	0.07	0.57	0.6	1.75	284.4	285.0	286.5	0.25
A42	0.3	0.3	0.3	0.32	0.80	0.08	0.45	0.6	1.75	284.4	285.0	286.5	0.77
A43	0.3	0.3	0.3	0.80	0.30	0.06	0.56	0.6	1.75	284.4	285.0	286.5	0.29
A44	0.3	0.3	0.3	0.66	0.50	0.06	0.52	0.6	1.51	284.4	285.0	286.9	0.47

Name	sp2	sp3	C-O	sp2	sp3	C-O	sp2	sp3	C-O	sp2	sp3	C-O	sp3/(sp3+sp2)
	M1[-]	M2[-]	M3[-]	h1[arb.un.]	h2[arb.un.]	h3[arb.un.]	s1[eV]	s2[eV]	s3[eV]	$E_0$1[eV]	$E_0$2[eV]	$E_0$3[eV]	[-]
B11	0.3	0.3	0.3	0.00	0.94	0.04	0.4	0.66	1.29	284.4	285.0	286.4	1.00
B12	0.3	0.3	0.3	0.42	0.76	0.04	0.47	0.6	0.99	284.4	285.0	286.8	0.70
B13	0.3	0.3	0.3	0.32	0.80	0.06	0.45	0.6	1.36	284.4	285.0	286.7	0.77
B14	0.3	0.3	0.3	0.65	0.51	0.06	0.52	0.6	1.27	284.4	285.0	286.8	0.48
B21	0.3	0.3	0.3	0.02	0.96	0.05	0.4	0.65	1.43	284.4	285.0	286.4	0.99
B22	0.3	0.3	0.3	0.13	0.89	0.06	0.4	0.63	1.72	284.4	285.0	286.3	0.92
B23	0.3	0.3	0.3	0.04	0.93	0.07	0.4	0.66	1.57	284.4	285.0	286.5	0.98
B24	0.3	0.3	0.3	0.18	0.87	0.08	0.4	0.61	1.72	284.4	285.0	286.3	0.88
B31	0.3	0.3	0.3	0.38	0.76	0.06	0.47	0.6	1.69	284.4	285.0	287.0	0.72
B32	0.3	0.3	0.3	0.62	0.54	0.06	0.51	0.6	1.68	284.4	285.0	287.0	0.51
B33	0.3	0.3	0.3	0.34	0.79	0.06	0.46	0.6	1.47	284.4	285.0	286.9	0.75
B34	0.3	0.3	0.3	0.14	0.90	0.06	0.4	0.62	1.63	284.4	285.0	286.4	0.91
B41	0.3	0.3	0.3	0.66	0.48	0.06	0.53	0.6	1.75	284.4	285.0	287.0	0.45
B42	0.3	0.3	0.3	0.61	0.55	0.06	0.5	0.6	1.67	284.4	285.0	287.0	0.52
B43	0.3	0.3	0.3	0.63	0.51	0.07	0.53	0.6	1.75	284.4	285.0	286.9	0.48
B44	0.3	0.3	0.3	0.25	0.83	0.08	0.42	0.62	1.75	284.4	285.0	286.4	0.83

Name	sp2	sp3	C-O	sp2	sp3	C-O	sp2	sp3	C-O	sp2	sp3	C-O	sp3/(sp3+sp2)
	M1[-]	M2[-]	M3[-]	h1[arb.un.]	h2[arb.un.]	h3[arb.un.]	s1[eV]	s2[eV]	s3[eV]	$E_0$1[eV]	$E_0$2[eV]	$E_0$3[eV]	[-]
C11	0.3	0.3	0.3	0.41	0.75	0.06	0.48	0.6	1.34	284.4	285.0	286.9	0.69
C12	0.3	0.3	0.3	0.56	0.60	0.06	0.5	0.6	1.65	284.4	285.0	287.0	0.57
C13	0.3	0.3	0.3	0.52	0.63	0.06	0.5	0.6	1.75	284.4	285.0	287.0	0.59
C14	0.3	0.3	0.3	0.02	0.93	0.08	0.4	0.64	1.53	284.4	285.0	286.4	0.98
C21	0.3	0.3	0.3	0.61	0.56	0.06	0.51	0.6	1.56	284.4	285.0	287.0	0.52
C22	0.3	0.3	0.3	0.52	0.64	0.07	0.49	0.6	1.63	284.4	285.0	287.0	0.60
C23	0.3	0.3	0.3	0.53	0.63	0.07	0.49	0.6	1.68	284.4	285.0	286.8	0.59
C24	0.3	0.3	0.3	0.58	0.59	0.07	0.5	0.6	1.68	284.4	285.0	286.9	0.55
C31	0.3	0.3	0.3	0.91	0.14	0.06	0.6	0.6	1.75	284.3	285.0	286.2	0.13
C32	0.3	0.3	0.3	0.56	0.61	0.06	0.5	0.6	1.56	284.4	285.0	287.0	0.56
C33	0.3	0.3	0.3	0.59	0.56	0.06	0.51	0.6	1.73	284.4	285.0	286.9	0.53
C34	0.3	0.3	0.3	0.04	0.92	0.09	0.4	0.66	1.59	284.4	285.0	286.4	0.98
C41	0.3	0.3	0.3	0.33	0.79	0.07	0.47	0.6	1.61	284.4	285.0	286.7	0.76
C42	0.3	0.3	0.3	0.33	0.81	0.06	0.46	0.6	1.51	284.4	285.0	286.6	0.76
C43	0.3	0.3	0.3	0.80	0.25	0.07	0.6	0.66	1.73	284.4	285.0	286.2	0.26
C44	0.3	0.3	0.3	0.59	0.58	0.06	0.5	0.6	1.54	284.4	285.0	286.9	0.54

Name	sp2	sp3	C-O	sp2	sp3	C-O	sp2	sp3	C-O	sp2	sp3	C-O	sp3/(sp3+sp2)
	M1[-]	M2[-]	M3[-]	h1[arb.un.]	h2[arb.un.]	h3[arb.un.]	s1[eV]	s2[eV]	s3[eV]	$E_0$1[eV]	$E_0$2[eV]	$E_0$3[eV]	[-]
D11	0.3	0.3	0.3	0.46	0.66	0.07	0.5	0.6	1.5	284.4	285.0	286.7	0.64
D12	0.3	0.3	0.3	0.41	0.73	0.06	0.48	0.6	1.75	284.4	285.0	287.0	0.69
D13	0.3	0.3	0.3	0.48	0.67	0.07	0.49	0.6	1.53	284.4	285.0	286.8	0.63
D14	0.3	0.3	0.3	0.62	0.51	0.07	0.51	0.6	1.7	284.4	285.0	286.6	0.49
D21	0.3	0.3	0.3	0.89	0.14	0.05	0.6	0.6	1.75	284.3	285.0	285.9	0.13
D22	0.3	0.3	0.3	0.52	0.65	0.06	0.49	0.6	1.66	284.4	285.0	286.9	0.61
D23	0.3	0.3	0.3	0.35	0.78	0.09	0.47	0.6	1.75	284.4	285.0	286.5	0.74
D24	0.3	0.3	0.3	0.63	0.48	0.08	0.54	0.63	1.75	284.4	285.0	286.4	0.46
D31	0.3	0.3	0.3	0.61	0.55	0.05	0.51	0.6	1.75	284.4	285.0	287.0	0.51
D32	0.3	0.3	0.3	0.40	0.71	0.07	0.53	0.65	1.75	284.4	285.0	286.7	0.68
D33	0.3	0.3	0.3	0.06	0.90	0.09	0.4	0.66	1.54	284.4	285.0	286.3	0.96
D34	0.3	0.3	0.3	0.91	0.13	0.06	0.6	0.6	1.71	284.3	285.0	286.0	0.13
D41	0.3	0.3	0.3	0.27	0.69	0.07	0.47	0.68	1.75	284.4	285.0	286.8	0.79
D42	-	-	-	-	-	-	-	-	-	-	-	-	-
D43	0.3	0.3	0.3	0.31	0.61	0.07	0.51	0.67	1.75	284.4	285.0	286.8	0.72
D44	0.3	0.3	0.3	0.30	0.68	0.07	0.45	0.6	1.75	284.4	285.0	286.6	0.75

Table 5.1: Decomposition of the carbon C 1s peak into three peak components sp^2, sp^3 and C-O. M is the mixing ratio and takes the value between 0 (pure Gaussian peak) and 1 (pure Lorentzian peak), h is the normalised height, the parameter s is 1/2 of FWHM of the peak and E_0 is the position of the peak. The last column represents the ratio of the sp^3 peak area to the sum of $(sp^3 + sp^2)$ areas denoting the degree of sp^3 hybridization.

Name	p-π	p-σ	O 2p	C $2p_2$	C $2p_1$	C $2s_3$	C $2s_2$	C $2s_1$	O 2s	p-π	p-σ	O 2p	C $2p_2$	C $2p_1$	C $2s_3$	C $2s_2$	C $2s_1$	O 2s
	h1	h2	h3	h4	h5	h6	h7	h8	h9	s1	s2	s3	s4	s5	s6	s7	s8	s9
	[arbitrary unit]									[eV]								
A11	-	-	-	-	-	-	-	-	-	-	-	-	-	-	-	-	-	-
A14	0.07	0.32	0.41	0.33	0.51	0.78	0.10	0.49	0.50	1.35	1.95	2.05	1.75	2.05	1.55	0.55	1.55	2.55
A41	0.09	0.31	0.45	0.36	0.55	0.77	0.21	0.51	0.53	1.25	1.95	2.05	1.75	2.05	1.55	0.65	1.55	2.55
A44	0.07	0.30	0.41	0.34	0.53	0.76	0.13	0.53	0.47	1.35	1.95	2.05	1.75	2.05	1.55	0.64	1.55	2.55
B11	0.09	0.33	0.41	0.37	0.52	0.75	0.13	0.45	0.50	1.25	1.95	2.05	1.75	2.05	1.55	0.64	1.55	2.55
B14	0.06	0.30	0.43	0.36	0.48	0.78	0.10	0.53	0.50	1.32	1.95	2.04	1.75	2.05	1.55	0.57	1.55	2.55
B41	0.07	0.32	0.41	0.29	0.52	0.74	0.10	0.41	0.47	1.25	1.95	2.05	1.75	2.05	1.55	0.57	1.55	2.55
B44	0.09	0.30	0.44	0.32	0.57	0.77	0.12	0.56	0.53	1.25	1.95	2.05	1.75	2.05	1.55	0.56	1.55	2.55
C11	0.06	0.31	0.44	0.30	0.59	0.75	0.16	0.60	0.47	1.35	1.95	2.05	1.75	2.05	1.55	0.65	1.55	2.55
C14	0.07	0.31	0.44	0.36	0.54	0.76	0.18	0.59	0.53	1.30	1.95	2.05	1.75	2.05	1.55	0.62	1.55	2.55
C41	0.07	0.30	0.42	0.33	0.54	0.76	0.17	0.51	0.49	1.35	1.95	2.05	1.75	2.05	1.55	0.61	1.55	2.55
C44	0.05	0.29	0.42	0.30	0.62	0.75	0.18	0.68	0.36	1.35	1.93	2.05	1.75	2.05	1.50	0.65	1.55	2.55
D11	0.12	0.34	0.47	0.34	0.61	0.77	0.16	0.54	0.62	1.25	1.95	2.05	1.85	2.05	1.55	0.65	1.55	2.55
D14	0.07	0.29	0.44	0.34	0.64	0.78	0.16	0.70	0.46	1.29	1.95	2.05	1.85	1.95	1.51	0.65	1.55	2.55
D41	0.07	0.26	0.38	0.33	0.55	0.78	0.13	0.57	0.35	1.33	1.95	2.05	1.75	2.05	1.55	0.65	1.55	2.55
D44	0.06	0.28	0.39	0.35	0.59	0.77	0.18	0.63	0.29	1.25	1.95	2.05	1.85	1.95	1.53	0.65	1.55	2.55

Name	p-π	p-σ	O 2p	C $2p_2$	C $2p_1$	C $2s_3$	C $2s_2$	C $2s_1$	O 2s	p-π	p-σ	O 2p	C $2p_2$	C $2p_1$	C $2s_3$	C $2s_2$	C $2s_1$	O 2s
	$E_0$1	$E_0$2	$E_0$3	$E_0$4	$E_0$5	$E_0$6	$E_0$7	$E_0$8	$E_0$9	Area 1	Area 2	Area 3	Area 4	Area 5	Area 6	Area 7	Area 8	Area 9
	[eV]									[arbitrary unit ·eV]								
A11	-	-	-	-	-	-	-	-	-	-	-	-	-	-	-	-	-	-
A14	3.1	5.6	9.0	11.9	14.1	16.6	18.4	19.7	25.1	0.20	1.32	1.73	1.21	2.19	2.51	0.11	1.57	2.66
A41	3.1	5.4	8.9	12.1	14.1	16.6	18.2	19.7	25.3	0.22	1.26	1.91	1.30	2.36	2.48	0.28	1.64	2.81
A44	3.1	5.6	8.9	11.9	14.1	16.6	18.4	19.7	25.2	0.19	1.24	1.77	1.25	2.28	2.47	0.17	1.71	2.52
B11	3.1	5.6	8.9	11.9	14.1	16.6	18.3	19.7	25.1	0.23	1.36	1.77	1.35	2.21	2.42	0.18	1.45	2.64
B14	3.1	5.6	8.9	11.9	14.1	16.6	18.3	19.7	25.1	0.16	1.21	1.82	1.30	2.05	2.51	0.12	1.72	2.67
B41	3.1	5.6	9.0	11.9	14.1	16.6	18.4	19.7	25.1	0.19	1.31	1.73	1.06	2.23	2.40	0.12	1.33	2.51
B44	3.1	5.6	8.9	11.9	14.1	16.6	18.3	19.7	25.1	0.23	1.23	1.90	1.18	2.44	2.48	0.14	1.80	2.80
C11	3.1	5.5	9.0	11.9	14.1	16.6	18.2	19.7	25.3	0.16	1.26	1.88	1.10	2.51	2.41	0.21	1.95	2.52
C14	3.1	5.6	8.9	11.9	14.1	16.6	18.3	19.7	25.2	0.18	1.26	1.86	1.33	2.32	2.46	0.23	1.90	2.81
C41	3.1	5.5	9.0	11.9	14.1	16.6	18.4	19.7	25.1	0.20	1.22	1.81	1.20	2.30	2.45	0.22	1.66	2.59
C44	2.9	5.5	9.1	11.9	14.1	16.7	18.2	19.7	25.3	0.15	1.16	1.80	1.08	2.64	2.34	0.24	2.21	1.91
D11	3.1	5.6	9.1	11.9	14.1	16.8	18.4	19.7	25.3	0.31	1.40	1.99	1.32	2.61	2.48	0.22	1.74	3.31
D14	3.1	5.6	9.1	11.9	14.1	16.7	18.2	19.7	25.3	0.19	1.19	1.89	1.31	2.61	2.45	0.22	2.26	2.42
D41	3.1	5.6	8.9	12.0	14.1	16.6	18.2	19.7	25.3	0.19	1.05	1.62	1.20	2.36	2.51	0.17	1.85	1.85
D44	2.9	5.6	9.0	11.9	14.1	16.7	18.2	19.7	25.1	0.16	1.14	1.66	1.34	2.39	2.46	0.25	2.04	1.55

Table 5.2: Decomposition of the DLC valence band into the nine peak components (p-π, p-σ, two C $2p$ peaks, three C $2s$, O $2p$ and O $2s$. The parameter h is the normalised height, s is 1/2 of FWHM of the peak and E_0 is the position of the peak.

Name	EA11	EA14	EA41	EA44	EB11	EB14	EB41	EB44	EC11	EC14	EC41	EC44	ED11	ED14	ED41	ED44
FB model																
A[-]	0.18	0.28	0.17	0.24	0.24	0.25	0.16	0.24	0.21	0.29	0.19	0.22	0.16	0.26	0.19	0.20
B [eV]	4.4	3.4	5.0	3.9	4.0	3.7	5.3	4.0	4.7	3.1	4.7	4.1	5.0	3.3	4.7	4.0
C [eV^2]	8.7	7.2	9.9	7.8	7.6	6.9	10.8	8.5	10.1	5.4	9.9	8.0	10.6	6.1	9.8	7.4
$n(\infty)$ [-]	1.85	1.90	1.80	1.89	1.86	1.88	1.76	1.86	1.89	1.92	1.81	1.91	1.80	1.77	1.81	1.75
E_g[eV]	0.72	0.65	1.08	0.69	0.88	0.71	0.87	0.63	0.75	1.00	0.79	0.85	0.80	0.87	0.96	0.87
h [nm]	520	425	364	424	363	335	338	439	300	362	347	414	480	374	392	366
χ	0.0025	0.0028	0.0045	0.0026	0.0026	0.0028	0.0040	0.0025	0.0038	0.0041	0.0031	0.0033	0.0025	0.0035	0.0032	0.0032
n(600nm)	2.11	2.21	2.01	2.19	2.12	2.19	2.00	2.18	2.19	2.16	2.08	2.18	2.04	2.02	2.04	2.00
k(600nm)	0.078	0.118	0.037	0.104	0.079	0.115	0.046	0.101	0.072	0.093	0.063	0.079	0.052	0.097	0.047	0.079
PJDOS model																
Q_π[eV$^{3/2}$]	1.9	2.5	-	2.4	0.9	2.8	0.8	2.8	0.9	0.6	0.9	1.0	0.7	0.5	0.5	1.6
$E_{g\pi}$[eV]	1.11	0.76	-	0.98	0.95	1.01	1.18	0.89	0.95	0.74	1.09	1.04	1.07	0.33	1.24	0.99
$E_{h\pi}$[eV]	4.90	6.21	-	5.72	3.61	5.68	3.62	6.49	3.64	2.97	3.49	3.76	3.38	2.89	3.03	4.98
Q_σ[eV$^{3/2}$]	185	190	-	190	185	190	177	189	195	185	183	192	179	168	178	171
$E_{g\sigma}$ [eV]	1.68	1.51	-	1.57	1.54	1.63	1.72	1.58	1.61	1.42	1.64	1.56	1.64	1.34	1.64	1.58
$E_{h\sigma}$[eV]	65	65	-	65	65	65	65	65	65	65	65	65	65	65	65	65
h [nm]	523	425	-	424	363	336	339	439	301	362	348	416	483	375	395	366
χ	0.0022	0.0021	-	0.0021	0.0025	0.0018	0.0034	0.0019	0.0022	0.0022	0.0028	0.0030	0.0029	0.0022	0.0055	0.0023
n(600nm)	2.10	2.21	-	2.19	2.12	2.19	1.99	2.18	2.18	2.15	2.07	2.18	2.03	2.02	2.03	2.00
k(600nm)	0.077	0.118	-	0.104	0.079	0.114	0.045	0.101	0.071	0.092	0.063	0.079	0.051	0.097	0.046	0.079

Table 5.3: Parameters of the FB and PJDOS models corresponding to the series E.
FB model: E_g is the optical energy band gap, $n(\infty)$ is the index of refraction at infinite frequency (should be 1),
PJDOS model: The parameters $E_{h\sigma}$, $E_{h\pi}$ are maximum energy limits of transitions, $E_{g\sigma}$, $E_{g\pi}$ are the minimum energy limits of transitions and Q_σ, Q_π are the parameters proportional to the valence electron densities of the material.
The thickness of the sample h, a quantity χ representing the quantity of the fit (0 is ideal and 0.001— the theoretical fit is indistinguishable by the eye from the experimental one), the index of refraction $n(600)$ and extinction coefficient $k(600)$ for λ=600 nm.